

**AD-A125 480**

**DRSAR-SF**

*1L*

**AD-A125 480**

**CHEMICAL SYSTEMS LABORATORY CONTRACTOR REPORT**

**ARCSL-CR-82060**

**MULTIPLE SCATTERING EFFECTS IN AEROSOLS:  
THEORETICAL INVESTIGATIONS**

**TECHNICAL  
LIBRARY**

**by**

**Adarsh Deepak**

**December 1982**

**Institute for Atmospheric Optics and Remote Sensing  
P.O. Box P, Hampton, Virginia 23666**

**Contract No. DAAK11-79-C-0100**



**US ARMY ARMAMENT RESEARCH AND DEVELOPMENT COMMAND  
Chemical Systems Laboratory  
Aberdeen Proving Ground, Maryland 21010**



**Approved for public release; distribution unlimited.**

#### **Disclaimer**

The views, opinions and/or findings contained in this report are those of the authors and should not be construed as an official Department of the Army position, policy, or decision unless so designated by other documentation.

#### **Disposition**

Destroy this report when it is no longer needed. Do not return it to the originator.

**UNCLASSIFIED**

SECURITY CLASSIFICATION OF THIS PAGE (When Data Entered)

<b>REPORT DOCUMENTATION PAGE</b>		<b>READ INSTRUCTIONS BEFORE COMPLETING FORM</b>
1. REPORT NUMBER ARCSL-CR-82060	2. GOVT ACCESSION NO.	3. RECIPIENT'S CATALOG NUMBER
4. TITLE (and Subtitle)  MULTIPLE SCATTERING EFFECTS IN AEROSOLS: THEORETICAL INVESTIGATIONS		5. TYPE OF REPORT & PERIOD COVERED Contractor Report September 1979 - July 1981
		6. PERFORMING ORG. REPORT NUMBER IIFAORS-208
7. AUTHOR(s)  Adarsh Deepak		8. CONTRACT OR GRANT NUMBER(s)  DAAK11-79-C-0100
9. PERFORMING ORGANIZATION NAME AND ADDRESS Institute for Atmospheric Optics and Remote Sensing P.O. Box P, Hampton, Virginia 23666		10. PROGRAM ELEMENT, PROJECT, TASK AREA & WORK UNIT NUMBERS 1L162622A552
11. CONTROLLING OFFICE NAME AND ADDRESS Commander, Chemical Systems Laboratory ATTN: DRDAR-CLJ-R Aberdeen Proving Ground, Maryland 21010		12. REPORT DATE December 1982
		13. NUMBER OF PAGES
14. MONITORING AGENCY NAME & ADDRESS (if different from Controlling Office) Commander, Chemical Systems Laboratory ATTN: DRDAR-CLB-PS Aberdeen Proving Ground, Maryland 21010		15. SECURITY CLASS. (of this report)  UNCLASSIFIED
		15a. DECLASSIFICATION/DOWNGRADING SCHEDULE NA
16. DISTRIBUTION STATEMENT (of this Report)  Approved for public release; distribution unlimited.		
17. DISTRIBUTION STATEMENT (of the abstract entered in Block 20, if different from Report)		
18. SUPPLEMENTARY NOTES  Contract Project Officer: Gerald C. Holst, Ph.D. (DRDAR-CLB-PS, 671-2543/2326).		
19. KEY WORDS (Continue on reverse side if necessary and identify by block number)  Multiple scattering Higher order scattering Aerosols Laser beams		
20. ABSTRACT (Continue on reverse side if necessary and identify by block number)  This report presents the results of a theoretical investigation on the effects of multiple scattering (MS) on the propagation of laser beams through scattering media. The theoretical formulations are given for three methods - two exact and one approximate - based on the solution of the radiative transfer equation in the small angle approximation. Computer codes were developed, optimized, and checked for consistency. The two methods are exact in the sense that the only approximation made is the small angle approximation. Using one (Continued on reverse side)		

**UNCLASSIFIED**

SECURITY CLASSIFICATION OF THIS PAGE(When Data Entered)

**20. ABSTRACT (Contd)**

of the exact methods, numerical results were obtained for contributions to MS due to various orders of scattering in the forward direction for various optical depths. The total MS contributions obtained by the two exact methods are shown to be in excellent agreement. The laser beam broadening due to MS by aerosols is also shown.

Using the approximate method, numerical results were also obtained for MS effects as functions of detector field of view, as well as the size of the detector's aperture; namely, for the cases when it is the same size as or smaller or larger than the laser beam diameter. The contrast between the on-axis intensity and the received power is shown for the last three cases.

## PREFACE

The work described in this report was authorized under Project 1L1622A552 Smoke and Obscurants Munitions, Smoke Technology. This work was started in September 1979 and completed in July 1981.

The use of trade names in this report does not constitute an official endorsement or approval of the use of such commercial hardware or software. This report may not be cited for purposes of advertisement.

Reproduction of this document in whole or in part is prohibited except with permission of the Commander, Chemical Systems Laboratory, ATTN: DRDAR-CLJ-R, Aberdeen Proving Ground, Maryland 21010. However, the Defense Technical Information Center and the National Technical Information Service are authorized to reproduce the document for United States Government purposes.

### Acknowledgments

It is a pleasure to acknowledge the valuable cooperation of and many fruitful discussions with Dr. Gerald C. Holst, Chemical Systems Laboratory Technical Monitor, during the course of this research. Special thanks are due Institute staff scientists Dr. Andrew Zardecki and Dr. V. O. Farrukh who diligently worked on and assisted in the successful completion of various portions of this work.

BLANK PAGE

## CONTENTS

	<u>Page</u>
1. INTRODUCTION. . . . .	7
2. EXACT METHODS FOR COMPUTING HIGHER ORDER AND TOTAL MULTIPLE SCATTERING OF LASER BEAMS . . . . .	9
2.1 INTRODUCTION . . . . .	9
2.2 SOLUTION FOR BEAM IRRADIANCE . . . . .	11
2.3 GAUSSIAN PHASE FUNCTION . . . . .	17
2.4 COMPUTATIONAL CONSIDERATIONS AND RESULTS . . . . .	19
2.5 DISCUSSION OF RESULTS AND CONCLUSIONS. . . . .	30
3. MULTIPLE SCATTERING CORRECTIONS AS FUNCTIONS OF DETECTOR FIELD OF VIEW . . . . .	39
3.1 INTRODUCTION . . . . .	39
3.2 THE FANTE-DOLIN THEORY . . . . .	40
3.3 CASE OF COLLIMATED GAUSSIAN BEAM . . . . .	43
3.4 CASE OF GENERAL GAUSSIAN BEAM. . . . .	45
3.5 NUMERICAL RESULTS. . . . .	46
4. CONCLUDING REMARKS. . . . .	78
5. REFERENCES . . . . .	80
DISTRIBUTION LIST . . . . .	85

## 1. INTRODUCTION

Whenever a beam of radiation passes through an aerosol medium, its energy always decreases during transit. The loss of energy is due to either scattering or absorption or both in the medium. The term extinction is defined as the sum of absorption and scattering. The transmittance  $T$  for a parallel, monochromatic beam of radiation of wavelength  $\lambda$  after passage through a homogeneous aerosol layer of length  $L$  and extinction coefficient  $\sigma_{ext}(\lambda)$ , in the single scattering (SS) approximation, is given by Bouguer-Beer law,  $T = e^{-\tau(\lambda)}$ , where the optical depth  $\tau(\lambda) = \sigma_{ext}(\lambda) L$ .

In SS, the scattered photon reaching the detector suffers only one scattering event; whereas, in multiple scattering (MS), it suffers more than one scattering event. Thus, the  $N^{th}$  order scattering refers to a case when a photon is scattered and rescattered  $N$  times before reaching the detector. The basis of the SS theory is that if one knows the scattering properties of an individual particle, then the scattering effect of  $N$  similar particles is simply  $N$  times that of a single particle.<sup>1</sup> Such a simple direct proportionality to  $N$  particles is what makes the SS theory so simple.

In the case of MS, this proportionality to  $N$  particles no longer holds, thereby making the theory very complicated. Therefore, except for a few researchers,<sup>2-14</sup> not much work has been done on experimental investigations on MS; even though relatively more work has been done on the theoretical aspects of MS.<sup>15-75</sup> Therefore, a coordinated research program was undertaken between the Institute for Atmospheric Optics and Remote Sensing (IAFORS) and Army Aberdeen Chemical System Laboratory (CSL) to implement systematic

research effort in the theoretical and experimental aspects of MS in aerosols in controlled laboratory environment. The theoretical research was performed at the Institute and the experimental work at CSL. Important features of such a theoretical and experimental approach to MS investigations were that the numerical results based on theoretical MS models could be compared with experimental results and vice versa. Laboratory experiments can serve to model real atmospheric conditions; and validation of MS theories are essential prerequisites for gaining confidence in their applications in real atmospheric conditions.

In this program, it was decided to start with the simple experiments on measurement of attenuation of visible and IR laser beams traversing through fog oil aerosols contained in a closed chamber, such as making measurement of: (1) optical depth for three or four wavelengths as a function of time, (2) size distribution of aerosols, (3) intensity of scattered radiance as a function of transverse distance from the direct beam axis.

On the theoretical aspects of the program, it was decided to develop exact<sup>22-24,47-48</sup> and approximate<sup>63-69</sup> methods based on solutions of the radiative transfer equation in the small angle approximation. Computer programs for two exact methods<sup>22-24,47-48</sup> were developed, optimized, and checked for consistency, and their results for scattered radiance as a function of optical depth for the various orders of scattering are shown in Section 2 of this report. In addition, the theory, computer codes, and computations for radiance as a function of the detector field-of-view using an approximate method<sup>63-69</sup> are discussed in Section 3. Conclusions and recommendations for future research efforts are given in Section 4.

2. EXACT METHODS FOR COMPUTING HIGHER ORDER  
AND TOTAL MULTIPLE SCATTERING OF  
LASER BEAMS

2.1 INTRODUCTION

Light propagation through optically thick particulate medium is basically a multiple scattering problem in which rays or photons traverse a medium of scatterers and undergo many scattering events before escaping. When a collimated laser beam is incident upon a thick scattering medium, it will suffer spatial and angular broadening as well as attenuation.<sup>16</sup> These effects, that inhibit optimum performance of both optical and communication systems, have recently become a focus of intensive experimental<sup>2-14</sup> and theoretical studies.<sup>15-75</sup> References 17-24 devoted to analytical investigation, parallel the Monte-Carlo treatment<sup>16,25,26</sup> of the problem.

The natural framework to study the multiple scattering problem is the transport theory. This theory, which does not directly include diffraction effects, deals with the transport of energy through a medium containing particles. Exact general solutions to the equation of transfer have not been obtained to date. However, there are some special cases where simple and useful approximate solutions are available. To mention but two limiting cases, for tenuous particle distribution, the first-order multiple scattering theory can be used, and for dense distribution the diffusion approximation is appropriate.<sup>27</sup> When particle size is much greater than a wavelength, as is the case typically for fogs, it is possible

to simplify the equation of transfer by employing the small angle approximation. This, in particular, involves the convolution integral in the gain term (containing the scattering phase function), which, obviously, lends itself to the application of the Fourier analysis. In an interesting investigation, Stotts<sup>28</sup> showed that the use of Fourier analysis requires the inclusion of all position and angular spatial frequency components in order to ensure the correct behavior for the scattered radiance in the small-angle approximation. His results preclude the low order truncation in the series expansion of the transformed phase function, as was attempted in Refs. 18 and 44. The high frequency limit, which is related to the first-order scattering, would not be adequate as the optical thickness becomes larger and larger. Therefore, it becomes important to estimate the contributions to the scattered radiance coming from scattering events of different orders, without the limitations imposed by the approximate Fourier techniques.

The purpose of this paper is to provide a systematic study of contributions of increasing order of scattering for both realistic and model aerosols. Our starting point will be the theory developed by Tam and Zardecki,<sup>22-24</sup> mainly to deal with multiple scattering of laser beams in fogs. This theory will be summarized in Section 2.2, which extends the original formulation for laser beams emanating from a point source to the more realistic case of laser beams of finite spatial width. Alternate schemes for solving the problem are described. In Section 2.3, we show how to construct the Gaussian phase functions that best approximate the exact Mie theory phase functions for both monodisperse and polydisperse aerosols. In Section 2.4 we discuss the computational aspects; and in Section 2.5 we

discuss the significance of the computed results in the context of laser beam propagation in dense aerosols.

## 2.2 SOLUTION FOR BEAM IRRADIANCE

Under the small-angle approximation, and with the  $z$ -axis chosen along the direction of the incident beam, the equation of transfer satisfied by the radiance (or specific intensity) distribution function,  $I(\underline{\phi}, \underline{r}, z)$ , reads as

$$\underline{\phi} \cdot \frac{\partial I}{\partial r} + \frac{\partial I}{\partial z} + \sigma_e I = \sigma_s \iint P(\underline{\phi} - \underline{\phi}') I(\underline{\phi}, \underline{r}, z') d^2\phi' \quad (1)$$

where  $\underline{\phi}$  is the transverse component of the unit propagation vector; the phase function,  $P$ , is considered to be a function of the difference of  $\underline{\phi}$  and  $\underline{\phi}'$ ; and  $\sigma_e$  and  $\sigma_s$  denote the extinction and scattering coefficients, respectively. In terms of the azimuthal angle  $\rho$ , the components of  $\underline{\phi}$  are  $(\theta \cos \rho, \theta \sin \rho)$ , where  $\theta$  is the scattering angle. In addition, we have adopted the convention in which the location of a given point in space is specified, in rectangular coordinate system, by  $(\underline{r}, z)$ , where  $\underline{r} = \hat{x}\hat{x} + \hat{y}\hat{y}$ .

Since most of the energy scattered by large particles in a unit volume is scattered in the forward direction, we assume that in the forward direction (or forward lobe) the angular distribution of scattered radiance can be represented by a Gaussian function. Thus the phase function  $P(\theta)$  may be written in terms of the projected angles  $\underline{\phi}$  as follows (see Fig. 1):

$$P(\underline{\phi}) = \frac{\alpha^2}{\pi} \exp(-\alpha^2 \underline{\phi}^2) \quad (2)$$

and that the incident laser beam can adequately be represented by a Gaussian functional form, both for the spatial distribution and the

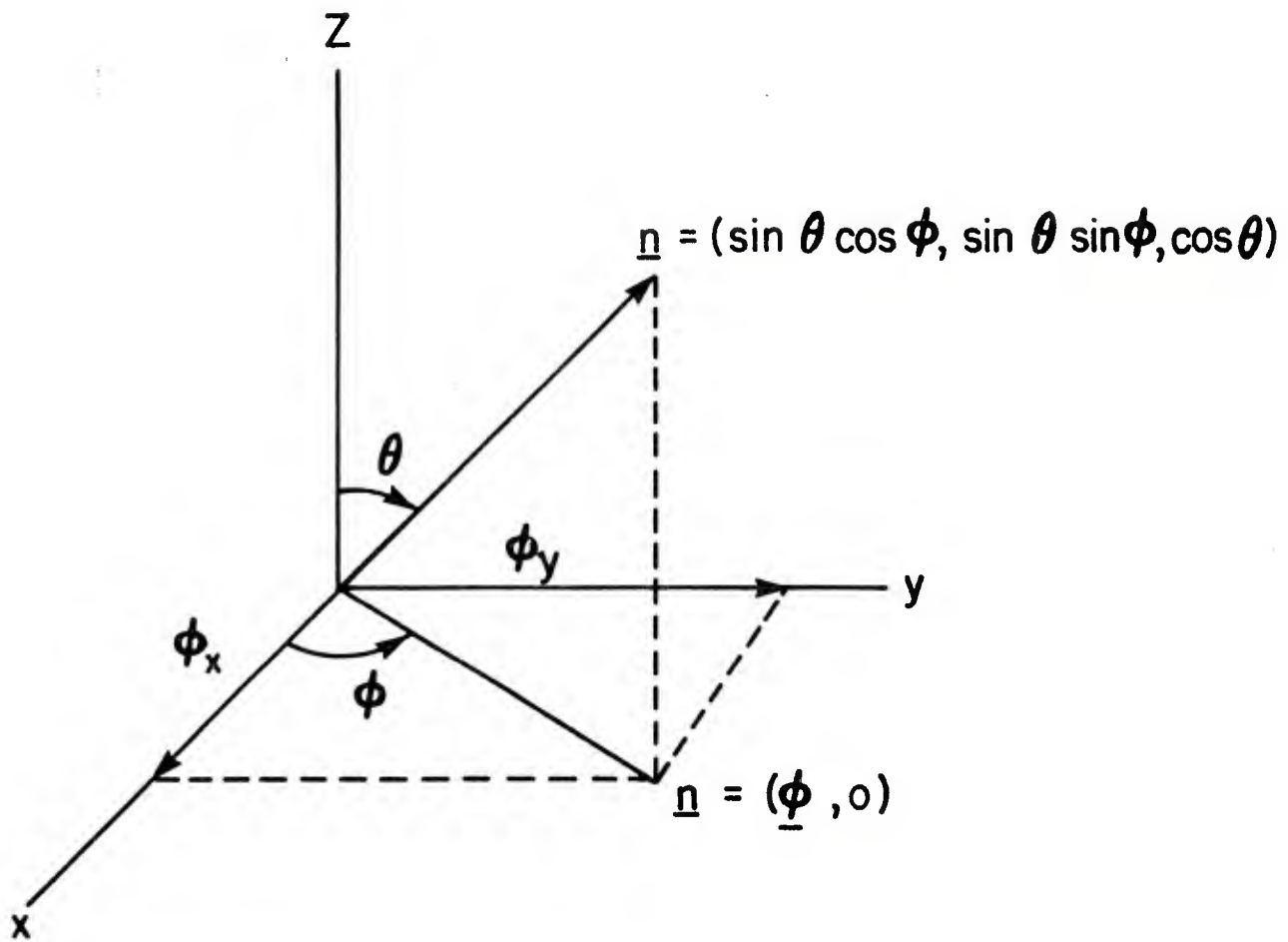


FIG. 1. The scattering geometrical relationships. In the small angle approximately the components of  $\underline{\phi}$  are  $(\phi_x, \phi_y) = (\theta \cos \rho, \theta \sin \rho)$ ,  $\theta$  being the scattering angle,  $\rho$  the azimuthal angle,  $\underline{n} = (\underline{\phi}, 0)$ , and the modulus of  $\underline{\phi}$  equals  $\theta$ , i.e.,  $|\underline{\phi}| = \theta$ .

angular divergence. Thus, the boundary condition at  $z = 0$  is expressed in the form

$$I_0(\underline{\phi}, \underline{r}) \equiv I(\underline{\phi}, \underline{r}, 0) = F\beta^2\gamma^2\pi^{-2} \exp(-\beta^2\underline{\phi}^2 - \gamma^2\underline{r}^2) \quad (3)$$

where  $F$  is the total power received at  $z = 0$ , the entrance plane of the cloud of particles.

Equation (1) may be solved by the use of Fourier transform techniques. With the incident beam specified by Eq. (3), we find by standard methods<sup>20,29</sup> the radiance of the scattered beam in the form of a Fourier integral over the variables  $(\xi, \eta)$ , which are the Fourier conjugates of variables  $(\underline{r}, \underline{\phi})$  in real space.

$$I(\underline{\phi}, \underline{r}, z) = \frac{1}{(2\pi)^4} \iiint \hat{I}(\xi, \eta, z) e^{-i(\xi \cdot \underline{\phi} + \eta \cdot \underline{r})} d^2\xi d^2\eta \quad (4)$$

where

$$\hat{I}(\xi, \eta, z) = F \exp(-\sigma_e z) \exp \left\{ -\frac{1}{4} \left[ \frac{(\xi + z\eta)^2}{\beta^2} + \frac{\eta^2}{\gamma^2} \right] \right\} \exp[\Omega(z)] \quad (5)$$

In Eq. (5), the function  $\Omega(z)$  is related to the Fourier transform of the phase function through the relation:

$$\Omega(z) = \sigma_s \int_0^z \hat{P}(\xi + z'\eta) dz' \quad (6)$$

which, in the case of the Gaussian functional form given by Eq. (2), becomes

$$\Omega(z) = \sigma_s \int_0^z \exp \left\{ -\frac{1}{4\alpha^2} |\xi + \eta z'|^2 \right\} dz' \quad (7)$$

As has been shown in Ref. 22, a form convenient for numerical computation is obtained as a power series generated by expanding the exponential containing  $\Omega(z)$  in a Taylor series and carrying out the integration over  $\xi$  and  $\eta$  before  $z'$ .

Because of the peaked nature of the phase function, the angular distribution of the incident beam is retained through several scattering events.<sup>13</sup> Therefore, for a detector whose field of view is considerably larger than  $\alpha^{-1}$ , which represents the angular spread of the phase function, the irradiance defined as

$$N(\underline{r}, z) = \iint I(\phi, \underline{r}, z) d^2\phi \quad (8)$$

will effectively be equal to the received power. In the following, discussions we shall be mainly concerned with the evaluation of the beam irradiance, thereby reducing the number of independent parameters to only two, namely,  $\underline{r}$  and  $z$ .

On combining Eqs. (4) and (8), one readily obtains the irradiance in the form of the following two-dimensional Fourier integral

$$N(\underline{r}, z) = \frac{1}{(2\pi)^2} \iint \hat{I}(\underline{\eta}, z) e^{-i\underline{\eta} \cdot \underline{r}} d^2\eta \quad (9)$$

where

$$\hat{I}(\underline{\eta}, z) \equiv \hat{I}(\xi = 0, \underline{\eta}, z) \quad (10)$$

$$= F e^{-\Omega_0 z} \exp \left\{ -\frac{1}{4} \left( \frac{z^2}{\beta^2} + \frac{1}{\gamma^2} \right) \underline{\eta}^2 \right\} \exp[\Omega_0(z)] \quad (11)$$

with

$$\Omega_0(z) = \sigma_s \int_0^z \exp \left\{ -\frac{\eta^2 z'^2}{4\alpha^2} \right\} dz' \equiv \frac{\alpha \sigma_s \sqrt{\pi}}{\eta} \operatorname{erf} \left( \frac{\eta z}{2\alpha} \right) \quad (12)$$

Eq. (9) can be simplified by the following two approaches: one, gives the separate contributions to total irradiance due to both single and higher order scattering; whence the second, gives the total multiple scattering (MS) contribution. It should be noted that in either case one also gets the unscattered contribution to total irradiance.

### (i) Various Orders of Scattering by Series Expansion

On expanding the exponential term containing  $\Omega_0(z)$  in Eq. (11) and performing the integration over  $\eta$ , we obtain

$$N(\underline{r}, z) = \sum_{m=0}^{\infty} N_m(\underline{r}, z) = (F/\pi z^2) \exp(-\sigma_e z) \sum_{m=0}^{\infty} \frac{(\sigma_s z)^m}{m!} N_m^0(\underline{r}, z) \quad (13)$$

where for the zeroth order ( $m = 0$ ) scattering,

$$N_0^0(\underline{r}, z) = \frac{\beta^2 \gamma^2 z^2}{\beta^2 + \gamma^2 z^2} \exp \left\{ -\frac{\beta^2 \gamma^2 r^2}{\beta^2 + \gamma^2 z^2} \right\} \equiv \frac{2z^2}{W^2(z)} \exp \left\{ -\frac{2r^2}{W^2(z)} \right\} \quad (14)$$

with  $W(z)/\sqrt{2}$  as the  $e^{-2}$ -point Gaussian width at axial distance  $z$ ;

for the  $m$ th order scattering

$$N_m^0(\underline{r}, z) = \int_0^1 \dots \int_0^1 dz_1 \dots dz_m \Lambda_m^{-1}(z) \exp \left[ -\frac{(\underline{r}/z)^2}{\Lambda_m(z)} \right] \quad (15)$$

with

$$\Lambda_m(z) = \alpha^{-2} \sum_{j=1}^m (1-z_j)^2 + \beta^{-2} + \gamma^{-2} z^{-2} \quad (0 \leq z_j \leq 1) \quad (16)$$

and for the single scattering ( $m = 1$ ):

$$N_1^0(\underline{r}, z) = \int_0^z dz_1 \Lambda_1^{-1}(z) \exp[-(\underline{r}/z)^2/\Lambda_1(z)] \quad (17a)$$

with

7

$$\Lambda_1(z) = \alpha^{-2}(1-z)^2 + \beta^{-2} + \gamma^{-2}z^{-2} \quad (0 \leq z, \leq 1) \quad (17b)$$

It should be noted that the width  $w_o$  at beam waist is related to  $\gamma$ ,  $\beta$  and  $W(z)$  by the relations

$$\gamma = \sqrt{2/w_o}, \quad \beta = kw_o/\sqrt{2} \quad (18a)$$

$$w^2(z) = w_o^2 + (2z/kw_o)^2 \quad (18b)$$

The problem has thus been reduced to a numerical computation of integrals given by Eq. (15), which describes, according to the Wentzel method,<sup>23,30,71</sup> the m-fold scattering contributions to the observed irradiance.

#### Single Order Scattering Contribution

The single scattering expression obtained from Eqs. (13, 15, and 16) by setting  $m = 1$  is difficult to evaluate numerically because it has a narrow spike at  $z_j = 1$  in Eq. (16). This problem can be solved by a variable transformation from  $z_j$  to  $\delta$ , namely

$$2z^2 \frac{(1 - z_j)^2}{\alpha^2} \frac{w_o^2}{w^2(z)} = \tan^2 \delta \quad (19)$$

which for single scattering ( $j = m = 1$ ) leads to:

$$N_1(\underline{r}, z) = N_o'(\underline{r}, z) \left[ \frac{\tilde{\omega} \tau e^{-\tau}}{AB} \int_0^{\delta_o} \exp \left\{ \frac{2r^2}{w_o^2} A^2 \sin^2 \delta \right\} d\delta \right] \quad (20)$$

where  $\tilde{\omega}$  is single scattering albedo;

$$\tau = \sigma_e Z;$$

$$\delta_o = \tan^{-1} AB;$$

$$A = w_o/W(z);$$

$$B = \sqrt{2} z/\alpha w_o;$$

$$\text{and } N_o'(\underline{r}, z) = \frac{F}{\pi z^2} N_o(\underline{r}, z)$$

This new expression in Eq. (20) is much easier to evaluate than the one in Eq. (17a.). These results are discussed later.

### (ii) Total Multiple Scattering Contribution

If we are interested in obtaining just the total MS contribution, without the need to know the individual contributions due to the different orders of scatterings, then we could use an alternate formulation<sup>47,48</sup> obtained by simplifying Eq. (9) by an appeal to circular symmetry of the propagating beam. By integrating the two dimensional integral of Eq. (9) over the azimuthal angle, we obtain the following expression:<sup>25, 26</sup>

$$N(r, z) = \frac{1}{2\pi} \int_0^\infty \hat{I}(\eta, z) J_0(\eta r) \eta d\eta \quad (21)$$

where  $\hat{I}(\eta, z)$  is defined by Eqs. (10) and (11), which can be written in terms of  $w_o$  as

$$\hat{I}(\eta, z) = F e^{-\tau} \exp \left\{ - \left[ \frac{\eta}{2} \right]^2 \left[ \frac{2z^2}{k^2 w_o^2} + \frac{w_o^2}{2} \right] \right\} \quad (22)$$

This formulation is computationally easier to evaluate than the series formulation of Eq. (13), provided the spatial point of interest lies within a volume bounded by a surface coaxial with the symmetry axis of the propagating Gaussian beam and at radial distance equal to the width of the unscattered Gaussian beam at that location.

### 2.3 GAUSSIAN PHASE FUNCTION

The radiative transfer multiple scattering formulation adopted here assumes that the scattering phase function is Gaussian. In general, such an assumption

does not strictly hold true for scattering profiles obtained by applying the Mie theory results for spherical particles.

Nevertheless, an assumption of Gaussian phase function could be justified in certain domains of aerosol particle size distributions. When the Mie scattering phase function is highly peaked in the forward direction, then the intensity contributions, resulting from scattering a few degrees from the forward, are negligible. Under these conditions an equivalent Gaussian phase function could be fitted to the forward peak of the Mie scattering phase function.

The procedure to obtain the Gaussian equivalent phase function is described as follows.

#### (i) Exact Mie Phase Function Formulation

It is assumed here that the individual scatterers are isotropic, homogeneous spheres, which enables one to apply the results of the Mie theory to evaluate the exact form of the volume scattering phase function  $P(\theta, x, \tilde{m}) [\text{sr}^{-1}]$ , as well as  $\sigma_s(x, \tilde{m}) [\text{m}^{-1}]$  and  $\sigma_e(x, \tilde{m})$  the volume scattering and extinction coefficients, respectively, where  $\theta$  is the scattering angle (Fig. 1),  $x = 2\pi r/\lambda$  is the size parameter,  $r [\mu\text{m}]$  is the particle radius,  $\lambda [\mu\text{m}]$  is the radiation wavelength, and  $\tilde{m} = m' - im''$  is the aerosol complex refractive index. The exact scattering phase function is defined as

$$P(\theta, x, \tilde{m}) = \frac{1}{2\pi\sigma_s} f(\theta, x, \tilde{m}) N_a \quad (\text{for monodisperse aerosols}) \quad (23a)$$

$$= \frac{1}{2\pi\sigma_s} \int_{r_1}^{r_2} f(\theta, x, \tilde{m}) n(a) da \quad (\text{for polydisperse aerosols}) \quad (23b)$$

$$\text{where } \sigma_s = \pi r^2 Q_s(x, \tilde{m}) N_a \quad (\text{monodisperse}) \quad (24a)$$

$$= \int_{r_1}^{r_2} \pi r^2 Q_s(x, \tilde{m}) n(a) da \quad (\text{polydisperse}) \quad (24b)$$

$$\text{and } f(\theta, x, \tilde{m}) = \left[ i_1(\theta, x, \tilde{m}) + i_2(\theta, x, \tilde{m}) \right] / 2k \quad (24c)$$

is the differential scattering cross-section  $\left[ \text{m}^2 \text{sr}^{-1} \right]$ ;  $i_1$  and  $i_2$  are Mie intensity functions;<sup>1</sup>  $Q_s$  is the efficiency factor;<sup>1</sup>  $n(r)$  is the aerosol size distribution  $\left[ \text{cm}^{-3} \mu\text{m}^{-1} \right]$ ; and  $N_r$  is the monodisperse aerosol number density  $\left[ \text{cm}^{-3} \right]$ ; and  $r_1$  and  $r_2$  are limits of integration. The convention introduced in Eq. (23b) ensures that the integral of  $P(\theta, x, m)$  over the total range of the argument will be equal to unity.

### (ii) Gaussian Fit to Mie Phase Functions

It is required to obtain a Gaussian phase function of the form

$$P(\theta, \alpha) = A e^{-\theta^2 \alpha^2} \quad (25)$$

where  $A$  is the peak value of the phase function which corresponds to the forward scattering peak obtained by the Mie formulation; and  $\alpha$  is the inverse angular width (in  $\text{rad}^{-1}$ ) of the equivalent scattering function.  $\alpha^2$  is obtained by plotting the normalized Mie phase function  $P(\theta)/P(0)$  versus  $\theta^2 \text{ deg}^2$  on a log-linear scale and obtaining the slope of the straight line that best fits in the least squares sense the forward lobe of the Mie phase function. The computations are discussed in the next section.

Such an approach will reproduce the optical effects of the forward peak of the scattering functions.

## 2.4 COMPUTATIONAL CONSIDERATIONS AND RESULTS

### (i) Mie Phase Functions

The Mie phase functions  $P(\theta, x, m)$  were computed by the exact Mie scattering codes<sup>76</sup> for monodisperse spherical aerosols of various radii (in the range  $2.0 \mu\text{m}$  to  $41.0 \mu\text{m}$ ) and for polydisperse aerosols, represented by analytic models,<sup>77</sup> such as, the popular Junge power law,

$$n(a) = p_1 a^{-p_2} \quad (a_1 \leq a \leq a_2) \quad (26)$$

and Deirmendjian<sup>76</sup> cloud model C1; here  $p_1$  and  $p_2$  are adjustable constants obtained from observational data. These normalized Mie phase functions are plotted as functions of  $\theta^2$  as shown in Figs. 2-5 by curves or straight lines connecting the circles. Figs. 2 and 3 are for the case of monodisperse aerosols; and Figs. 4 and 5 are for polydisperse aerosols. In the case of particles large compared to  $\lambda$ , the Mie phase function becomes highly oscillatory, hence the dog-legged shape of the plot in Fig. 3.

### (iii) Gaussian Fits to the Forward Lobe

The equivalent Gaussian phase function is then obtained by best fitting the functional form  $P(\theta, \alpha)$  in Eq. (25) to the forward lobe of the normalized Mie phase functions. The best fits, obtained by the use of a least squares code, are shown by the dashed line in Figs. 2-5. The slope of dashed line yields  $\alpha(\text{deg}^{-1})$ ; and the normalization constant, the value for A.

Gaussian phase functions, as given by Eq. (25), were best fitted to the exact Mie phase functions for monodisperse aerosols with radii in the range from 2.01  $\mu\text{m}$  to 40.2  $\mu\text{m}$  and refractive indices  $m' = 1.33$  and 1.55. Essential parameters of these cases are summarized in Table 1. The Gaussian fit obviously suppresses the oscillations originating from the diffraction effect. These oscillations are effectively smoothed out in the case of polydisperse aerosols, as can be seen from Figs. 4 and 5. The Gaussian approximation merely leads to a faster convergence for large scattering angles. It may be reminiscent of other approaches to the multiple scattering, e.g., the statistical theory of Whitney,<sup>45</sup> by which the fine details of the angular scattering problem are lost, thus circumventing the need for the generation of the phase function with a Mie code.

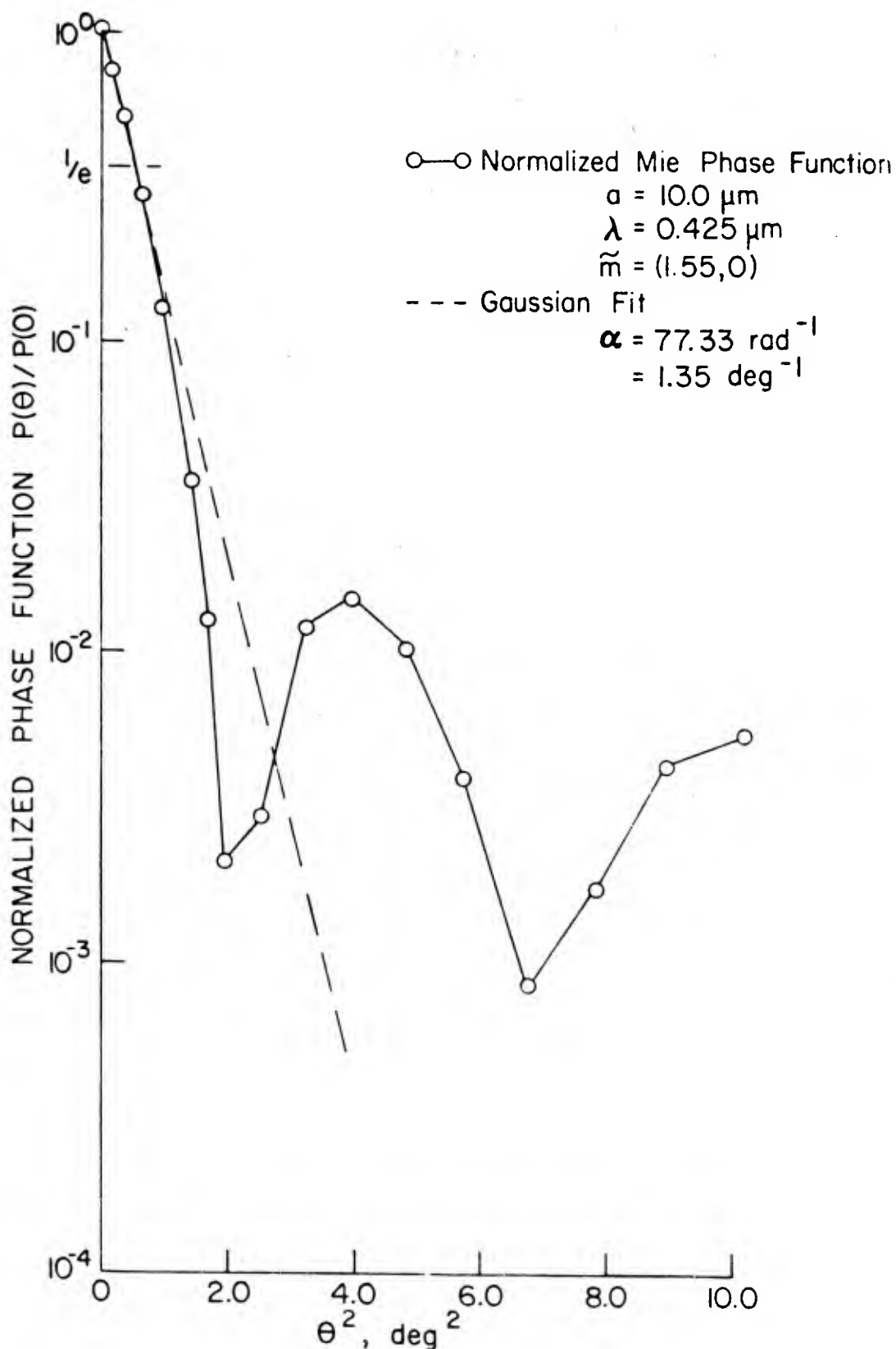


FIG. 2. Gaussian fit to the forward lobe of the normalized Mie phase function for  $\lambda = 0.425 \text{ mm}$  and monodisperse spherical particles of  $a = 10.0 \mu\text{m}$  and  $\tilde{m} = (1.55 - 0i)$ .

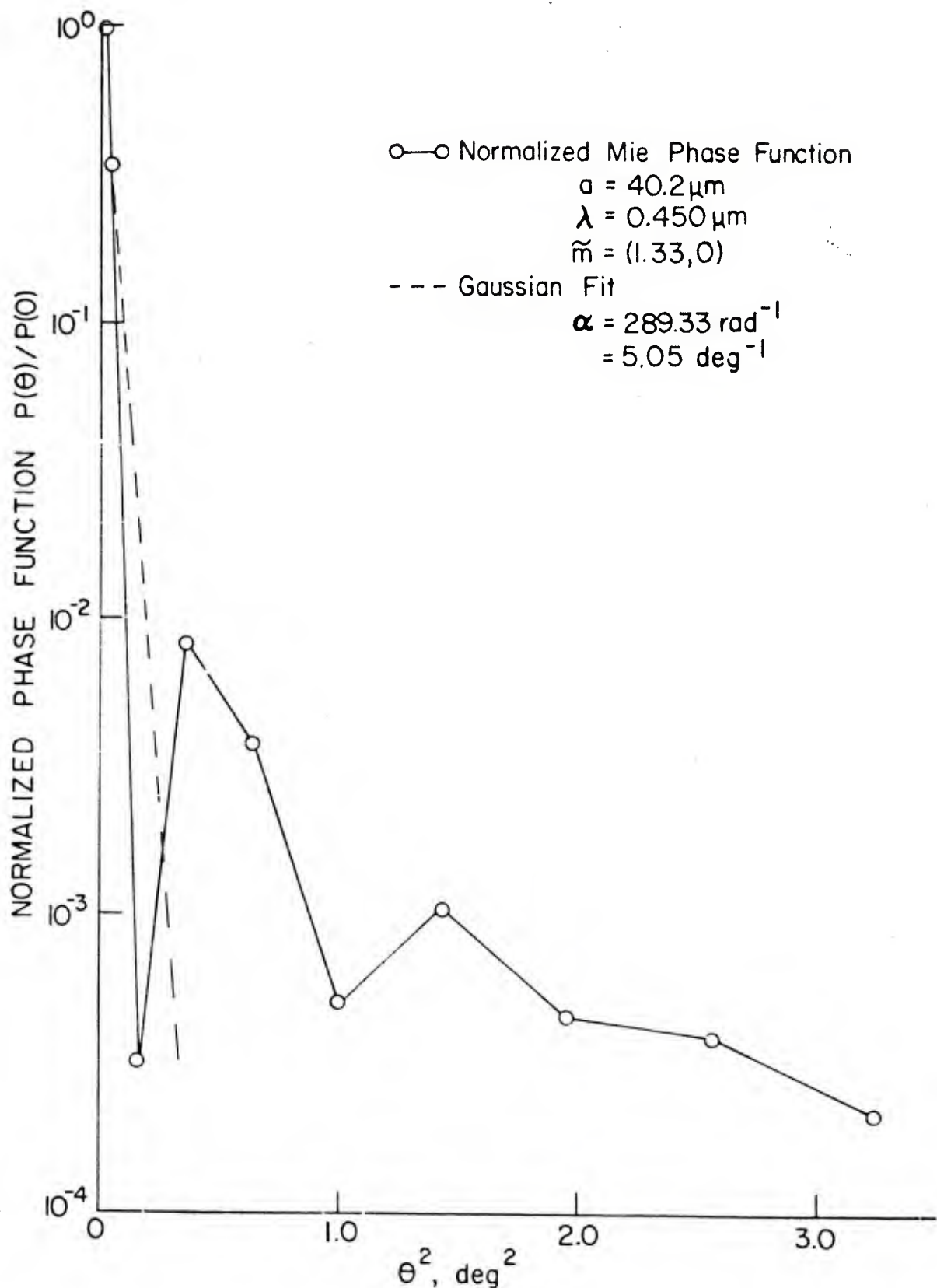


FIG. 3. Gaussian fit to the forward lobe of the normalized Mie phase function for  $\lambda = 0.45 \mu\text{m}$  and monodisperse spherical particles of  $a = 40.2 \mu\text{m}$  and  $m = (1.33 - 0i)$ .

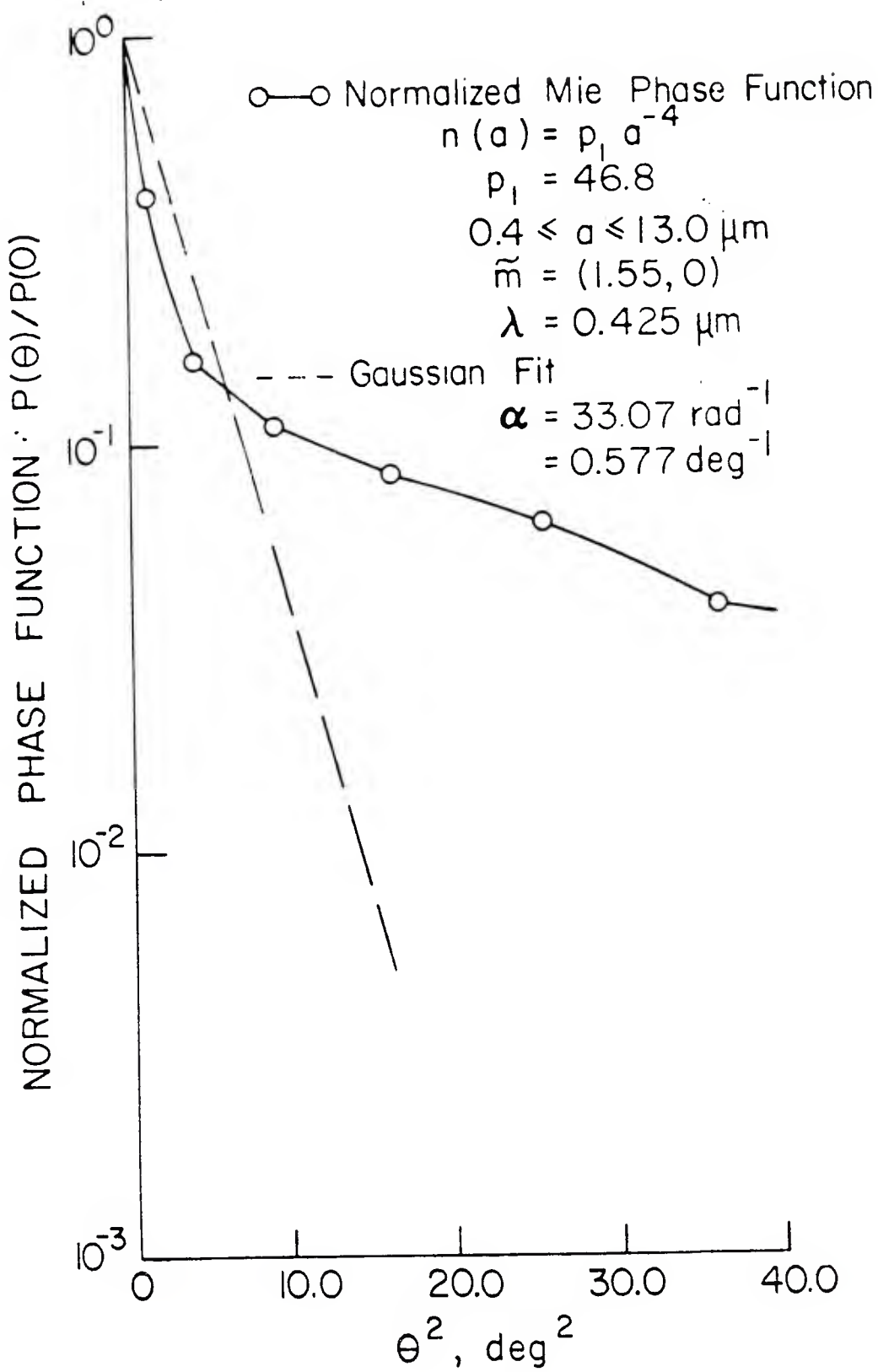


FIG. 4. Gaussian fit to the forward lobe of the normalized Mie phase function for  $\lambda = 0.425 \mu\text{m}$  and polydisperse aerosols of size distribution  $n(a) = p_1 a^{-4}$ , with  $p_1 = 46.8$ ,  $0.4 \leq a \leq 13.0 \mu\text{m}$ , and  $\tilde{m} = (1.55 - 0i)$ .

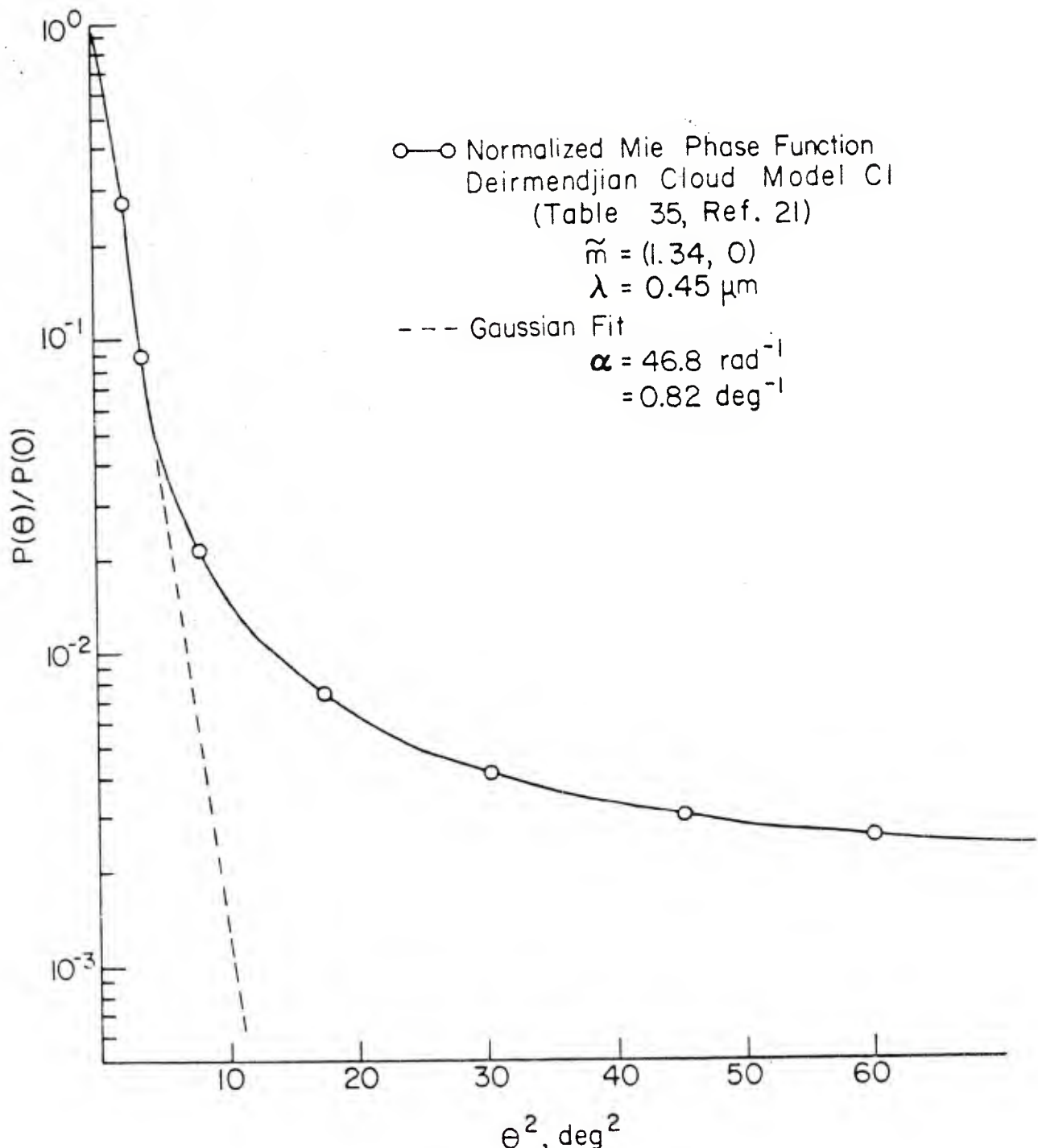


FIG. 5. Gaussian fit to the forward lobe of the normalized Mie phase function values obtained from (Table 35, Ref. 21) for  $\lambda = 0.45 \mu\text{m}$ , Deirmendjian Cloud Model C1, and  $\tilde{m} = (1.34 = 0i)$ .

TABLE 1. Inverse Angular Width  $\alpha$  of Equivalent Gaussian Fit to the Forward Lobe of the Mie Phase Functions for Different Monodisperse Aerosols

$r$ ( $\mu\text{m}$ )	$\lambda$ ( $\mu\text{m}$ )	$x$	$m'$	$\alpha$ $\text{deg}^{-1}$	$\alpha$ $\text{rad}^{-1}$
2.01	0.450	28.06	1.33	0.29	16.82
5.00	0.425	73.92	1.55	0.71	40.51
7.75	0.425	114.58	1.55	1.00	57.30
10.00	0.425	147.84	1.55	1.35	77.33
15.50	0.425	229.15	1.55	2.15	123.37
20.00	0.425	295.68	1.55	2.60	148.71
26.80	0.450	374.20	1.33	3.58	205.15
31.00	0.425	458.30	1.55	4.12	236.24
38.00	0.425	561.30	1.33	5.05	289.33
40.20	0.450	561.30	1.33	5.05	289.33

(iii) Variation of  $\alpha$  as Function of  $m'$  and  $x$

The values of the inverse angular widths for monodisperse nonabsorbing particles from Table 1, when plotted as shown in Fig. 6, fall, as expected, on a straight line. The slope of the lines are functions of the index of refraction of the scattering particles. It could be concluded as a rule that as the index of refraction increases for nonabsorbing particles, the forward scattering peak broadens and the angular width per degree drops as a result. Under certain conditions it is difficult to estimate accurately the index of refraction of such particles or it may be an unknown quantity under certain circumstances. On examining equations (13) through (16) we can deduce the following relationship

$$\frac{\partial N(a, z)}{\partial \alpha} = -\frac{\alpha}{z} \frac{\partial N(a, z)}{\partial z} \quad (26)$$

which reveals that the far field scattered radiation is insensitive to small changes in  $\alpha$ , the inverse angular scattering width.

The two lines in Fig. 10 obey the following fitted expression:

$$\alpha = 3.25 \frac{(m')^{-1/2}}{\lambda} r \quad (27)$$

where  $\alpha$  is the inverse angular width per radian,  $\lambda$  (wavelength) and  $r$  (particle radius in  $\mu\text{m}$ ; and  $m'$  the real part of complex aerosol refractive index). If the refractive index changes by a small amount, then

$$\Delta \alpha = \frac{3.25}{\lambda} r \left[ \frac{1}{m'_1} - \frac{1}{m'_2} \right] \approx -\alpha \frac{\Delta m'}{2m'} \quad (28)$$

which means that the percentage change of the inverse angular width  $\alpha$  is half that of the corresponding change in the index of refraction.

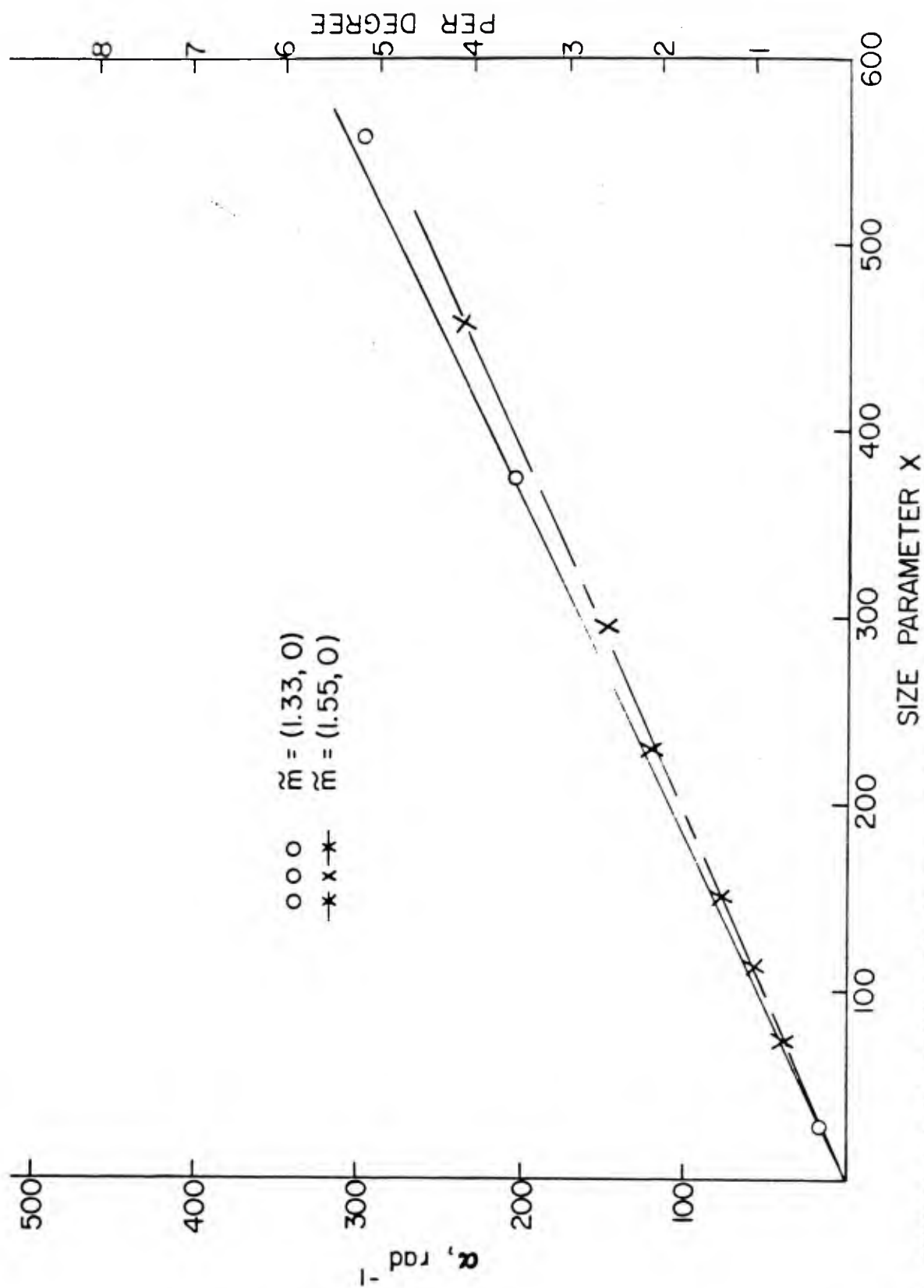


FIG. 6. Inverse angular width  $\alpha$  of the forward lobe of the scattering phase function for monodisperse, nonabsorbing aerosols plotted as a function of aerosol size parameter  $x$  for  $m = 1.33$  and  $1.55$ .

(iv) Computational Problems in Evaluation Eq. (21).

To check out computation scheme for solving Eq. (21), we decided first to compute  $N_0(r,z)$  by setting  $\sigma_s = 0$ , or  $\tau = 0$ , in Eq. (22) and performing the integrations over  $\eta$  for various values of  $r$ . Results for  $N_0$  thus obtained from Eq. (21) using a 1000-point trapezoidal integration scheme agreed very well with those from Eq. (14), for  $r \leq W(z)$ , i.e., the discrepancies were less than 0.5%. However, negative or erroneous results were obtained for  $r > W(z)$ , due to the need to include a very large number (i.e. over 20) of cycles in the evaluation of  $J_0(\eta r)$ , which involves values of  $J_0$  comparable to the errors in the numerical representation of  $J_0$  obtained from the Handbook of Mathematical Functions, p. 369 (Abramowitz and Stegun<sup>78</sup>). The error in the use of this representation is less than or equal to  $1.6 \times 10^{-8}$ , which implies that whenever the absolute values of  $J_0$  become comparable to or smaller than this error, then the integration of Eq. (21) yields erroneous results.

In addition, to avoid underflows in the numerical evaluation, negative arguments in the exponential were not allowed to exceed 675. As a result of the highly complicated numerical integration problems arising due to the oscillatory nature of the zero order Bessel function in the integrand in Eq. (21), the following computational method was developed to compute the total irradiance  $N(r,z)$ . In this scheme, first we determined the locations of the zeros of the Bessel functions, and the intervals between the zeros were then subdivided by a predetermined integral value to accommodate the variations in the Bessel function cycles within a fixed range of integration. This method is very useful due to the fact that Eq. (21) becomes highly oscillatory and a fixed interval computational scheme gives erroneous results. Computation of off-axis irradiance with this method becomes more expensive as the radial

distance  $r$  is increased. The results for  $N(r,z)$  are given in Table 2.

(v) Computation Problems in Evaluating Eq. (15) for Various Scattering Orders.

(a) First Order Scattering Contribution  $N_1$

Equations (13)-(15) were found to have a spike in values of  $N_m(r,z)$  at the integration limit  $z_1 = 1$ , arising due to the expression

$$C = \frac{1}{1 + ((1 - z_1)^2 + \frac{\alpha^2}{\beta^2}) \frac{z_w^2}{\alpha_2^2}} \quad (29)$$

As explained in Section II(i), this problem was solved by making a variable transformation from  $z_1$  to  $\delta$ , as shown in Eq. (19), to arrive at transformed Eq. (20) for  $N_1(r,z)$ . The integral in Eq. (20) was easily evaluated by using a simple 100-point trapezoidal integration scheme. The results for  $N_1$  are shown in Table 2.

(b) Second and Higher Order Scattering Computations

For higher order scattering computations the Conroy method<sup>58,79</sup> was adopted. In the Conroy method, in contrast to the Monte Carlo method, the sample points are distributed systematically over the integration region and are optimally predetermined to achieve convergence. A characteristic feature of the Conroy method is that the number of sample points will need to be increased to achieve a specific degree of accuracy as we go to integrals of higher and higher multiplicity. In this method, eight different sample point sets are available for multidimensional integrations for  $m = 2$  to 12, in a tabular form in Ref. 58 and 79.

The 1154-point sets given in Ref. 58, were used to compute 2 to 7 dimensional integrations (for  $m = 2$  to 7); the 3708-point set was used to

compute 8 dimensional integration (for  $m = 8$ ); and the 3722-point sets used to compute from 9 to 12 dimensional integrations (for  $m = 9$  to 12). The selection of these point sets was made by repeatedly performing the integrations with the different sets and selecting the lowest point set that achieved convergence.

## 2.5 DISCUSSION OF RESULTS AND CONCLUSIONS

Table 2 presents a summary of the results obtained from Eqs. (20), (13), (15) and (21) for SS, higher order scattering, and total irradiance contributions for an aerosol cloud represented by Gaussian phase function with  $\alpha = 46.8 \text{ rad}^{-1}$ , shown in Fig. 5, at transverse distances  $r = 0.0$  and  $2.0 \text{ cm}$  and layer depths  $z = 10^{-4}, 10^{-3}, \dots, 10^2$  and  $10^3 \text{ km}$ .

In Table 3, we show a typical set of results obtained from Eqs. 14 and 15 for the irradiance contributions due to the different orders of scattering for a 10 m deep cloud of aerosols represented by a Gaussian phase function with  $\tau = 289.33 \text{ rad}^{-1}$ , shown in Fig. 3, and for optical depths  $\tau = 0.1, 0.3, 1.0, 3.0, 5.0$  and  $7.0$ . Also, shown are results for the total scattered and the direct attenuated irradiances. Figures 7 and 8 depict the unscattered ( $N_0$ ), MS and total scattered irradiance as a function of the relative transverse distance,  $r/W_0$  at  $z = 10 \text{ m}$  for an aerosol cloud, represented by a Gaussian phase function with  $\alpha = 289.33 \text{ rad}^{-1}$  in Fig. 3, and having optical depths  $\tau = 0.1$  and  $2.0$ , respectively. Figure 9 depicts the same quantities for aerosol cloud with  $\alpha = 33.07 \text{ rad}^{-1}$  and  $\tau = 0.2$  and  $4.2$ . Figure 10 shows the variations of unscattered, multiple scattering orders ( $m = 1, 2, \dots, 15$ ), total MS, and total irradiance received by an open detector placed coaxially along the direction of beam propagation for various optical depths up to  $\tau = 10.0$  due to an aerosol cloud having  $\alpha = 289.33 \text{ rad}^{-1}$  and  $z = 10 \text{ m}$ .

TABLE 2

Scattered Irradiance at Various  $z$  and  $r$  for Gaussian Laser Beam of Width  $W_0 = 1.0$  cm Propagating Through Water Cloud C1, Represented by a Gaussian Phase Function with  $\alpha = 46.8$  rad $^{-1}$  shown in Fig. 5 and Having an Optical Depth  $\tau = 1.0$

$z$	$r$ cms	Scattered Irradiance Using Series Method (Eq. 13)			Total Scattered Irradiance Using Eq. (21)
		SS Irradiance		Total	
		Orders 2 and above	Using Eq. (20)	(1) + (2)	
$z$	$r$ cms	(1)	(2)	(1) + (2)	
1000 km	0.0	0.849 (-10)	*	0.109 (-12)	0.850 (-10)
	2.0	0.849 (-10)	0.109 (-12)	0.850 (-10)	0.849 (-10)
100 km	0.0	0.849 (-8)	0.109 (-10)	0.850 (-8)	0.849 (-8)
	2.0	0.849 (-8)	0.109 (-10)	0.850 (-8)	0.848 (-8)
10 km	0.0	0.847 (-6)	0.109 (-8)	0.848 (-6)	0.847 (-6)
	2.0	0.831 (-6)	0.109 (-8)	0.832 (-6)	0.830 (-6)
1 km	0.0	0.696 (-4)	0.110 (-6)	0.697 (-4)	0.696 (-4)
	2.0	0.277 (-4)	0.110 (-6)	0.278 (-4)	0.278 (-4)
100 m	0.0	0.120 (-2)	0.109 (-4)	0.121 (-2)	0.121 (-2)
	2.0	0.250 (-3)	0.101 (-4)	0.260 (-3)	0.259 (-3)
10 m	0.0	0.119 (-1)	0.779 (-3)	0.127 (-1)	0.127 (-1)
	2.0	0.226 (-2)	0.526 (-3)	0.279 (-2)	0.279 (-2)
1 m	0.0	0.969 (-1)	-	-	0.129 (0)
	2.0	0.573 (-2)	-	-	0.120 (-1)
0.1 m	0.0	0.227 (0)	-	-	0.385 (0)
	2.0	0.976 (-4)	-	-	0.203 (-3)

\* Arguments in parenthesis denote powers of 10.

TABLE 3. Different Orders of Scattering For Various Values of  $\tau$  For a 10 m Layer of Aerosols with Phase Function Represented by a Gaussian with  $\alpha = 289.33$  as Shown in Figure 3.

$\tau$	Irradiance ( $\text{W}/\text{cm}^2 \mu\text{m}$ ) for $m$ th Order of Scattering				Total Scattered Irradiance $\Sigma N_m$ ( $\text{W}/\text{cm}^2 \cdot \mu\text{m}$ )	Direct Attenuated Irradiance ( $\text{W}/\text{cm}^2 \cdot \mu\text{m}$ )
	1st	2nd	3rd	4th		
0.1	$4.5 \times 10^{-4}$	$3.16 \times 10^{-5}$	$1.79 \times 10^{-6}$			$4.85 \times 10^{-4}$
0.3	$3.88 \times 10^{-2}$	$2.27 \times 10^{-3}$	$1.21 \times 10^{-4}$	$5.89 \times 10^{-6}$	$4.12 \times 10^{-2}$	$4.74 \times 10^{-1}$
1.0	$6.70 \times 10^{-2}$	$1.29 \times 10^{-2}$	$2.27 \times 10^{-3}$	$3.66 \times 10^{-4}$	$8.25 \times 10^{-2}$	$2.39 \times 10^{-1}$
3.0	$2.83 \times 10^{-2}$	$1.63 \times 10^{-2}$	$8.62 \times 10^{-3}$	$4.17 \times 10^{-3}$	$1.82 \times 10^{-3}$	$5.91 \times 10^{-2}$
5.0	$6.45 \times 10^{-3}$	$6.29 \times 10^{-3}$	$5.58 \times 10^{-3}$	$4.54 \times 10^{-3}$	$3.31 \times 10^{-3}$	$3.08 \times 10^{-2}$
7.0	$1.31 \times 10^{-3}$	$1.76 \times 10^{-3}$	$2.17 \times 10^{-3}$	$2.46 \times 10^{-3}$	$2.50 \times 10^{-3}$	$1.77 \times 10^{-2}$
						$6.68 \times 10^{-4}$

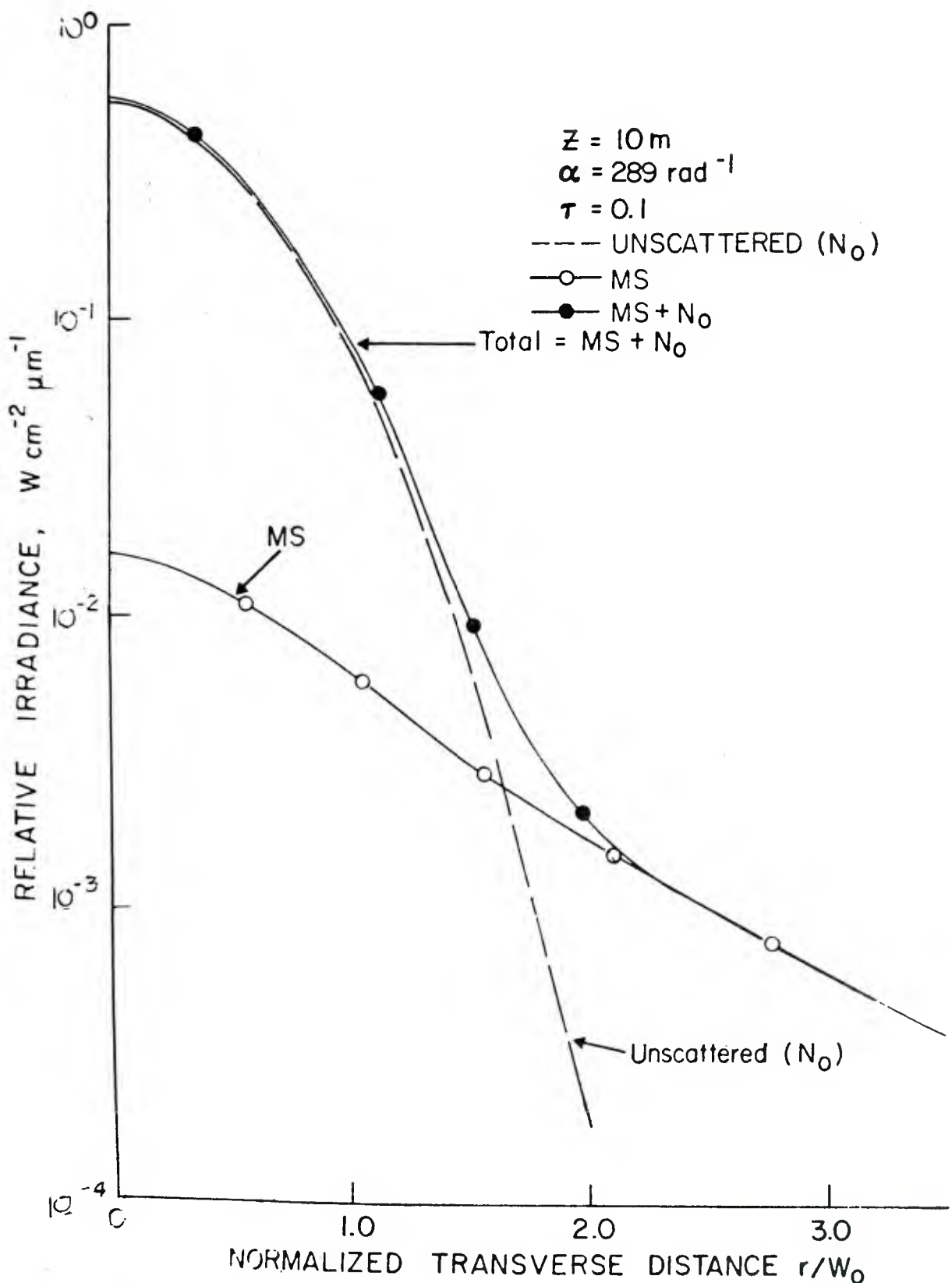


FIG. 4. Relative irradiance as a function of the normalized transverse distance ( $r/W_0$ ) for  $z = 10 \text{ m}$ ,  $\alpha = 289.33 \text{ rad}^{-1}$  and  $\tau = 0.1$ .

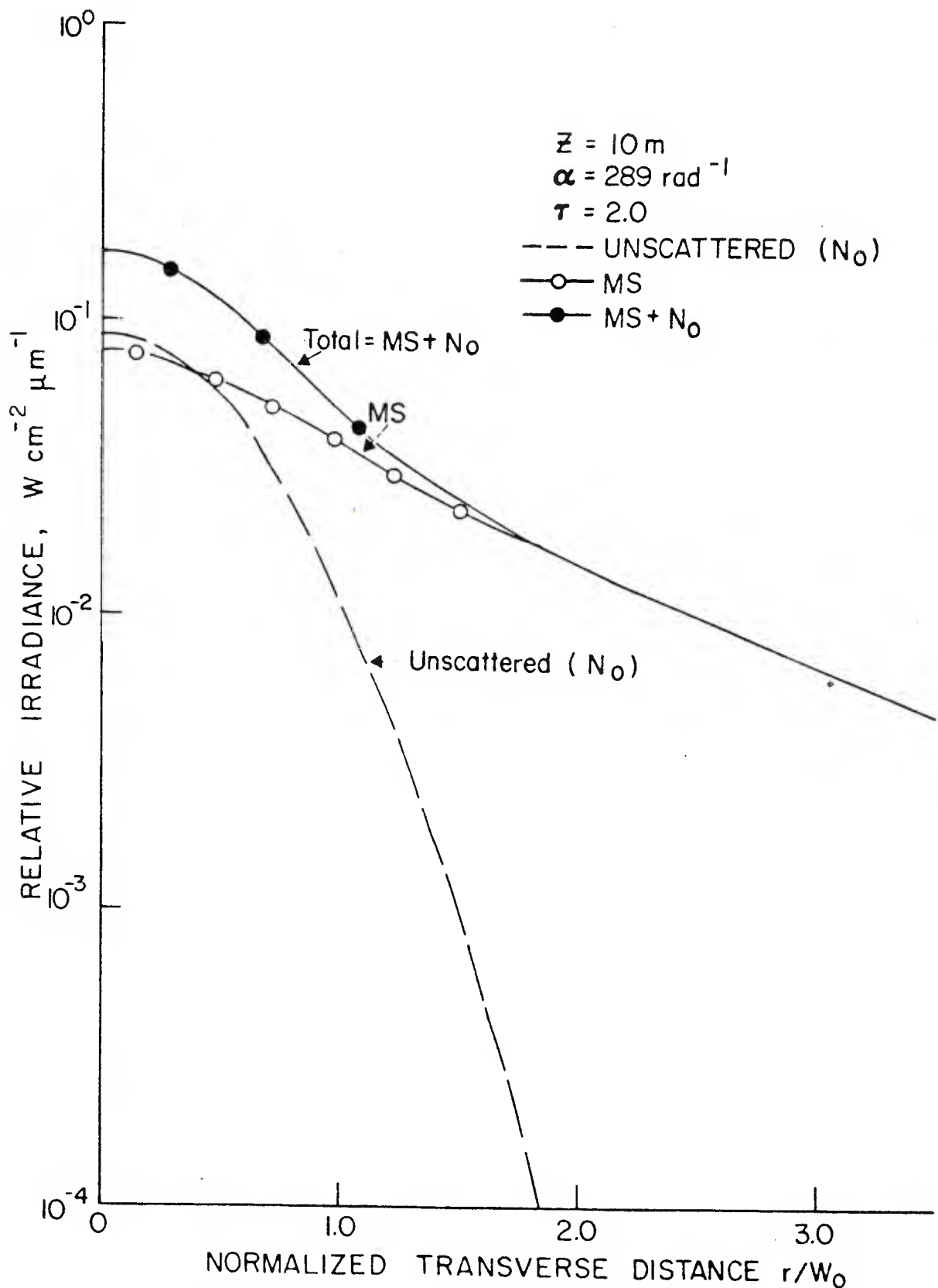


FIG. 8. Relative irradiance as a function of the normalized transverse distance ( $r/W_0$ ) for  $z = 10 \text{ m}$ ,  $\alpha = 289.33 \text{ rad}^{-1}$  and  $\tau = 2.0$ .

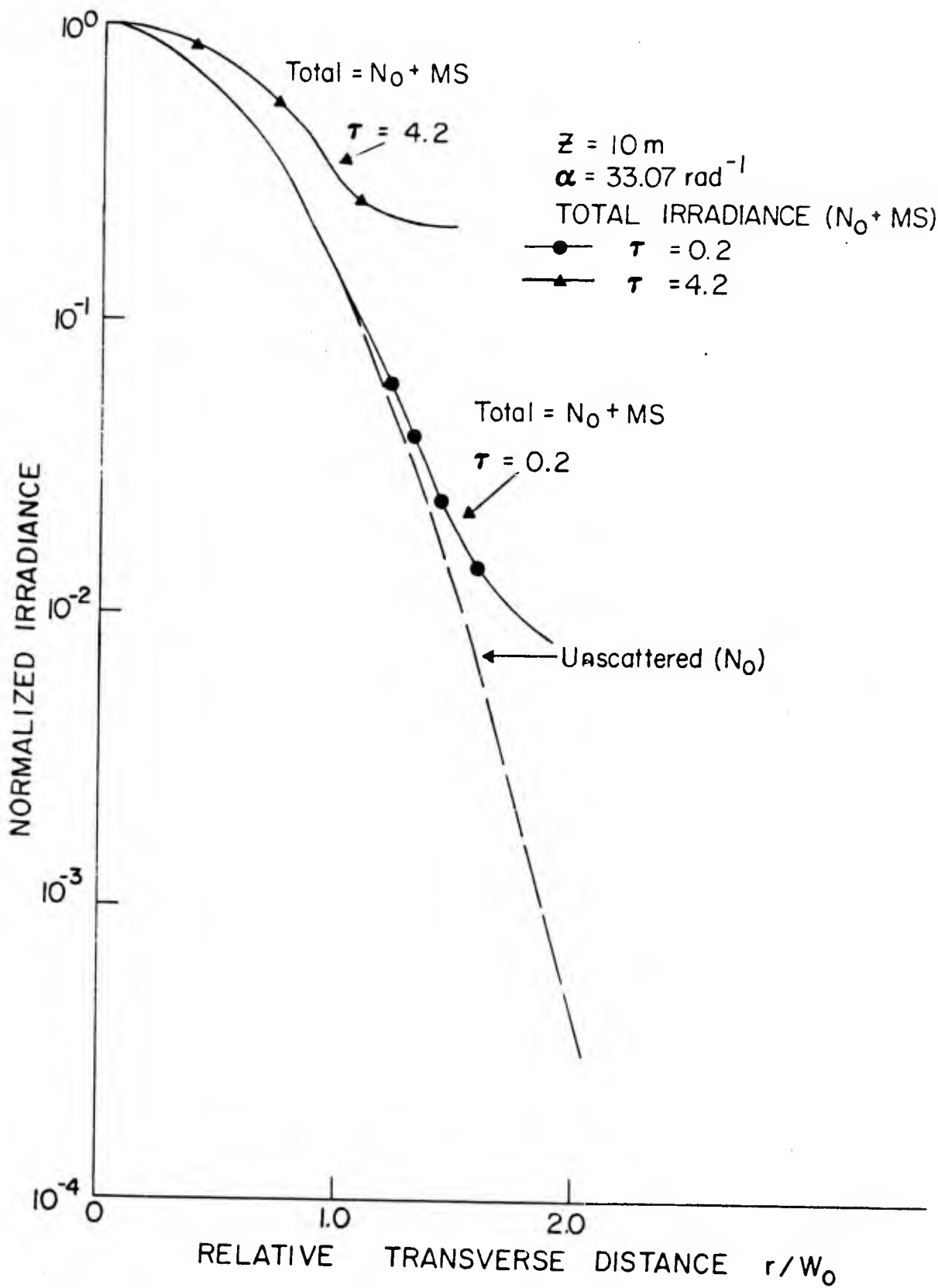


FIG. 9. Normalized irradiance as a function of the normalized transverse distance ( $r/W_0$ ) for  $z = 10 \text{ m}$ ,  $\alpha = 33.07 \text{ rad}^{-1}$  for  $\tau = 0.2$  and  $4.2$ .

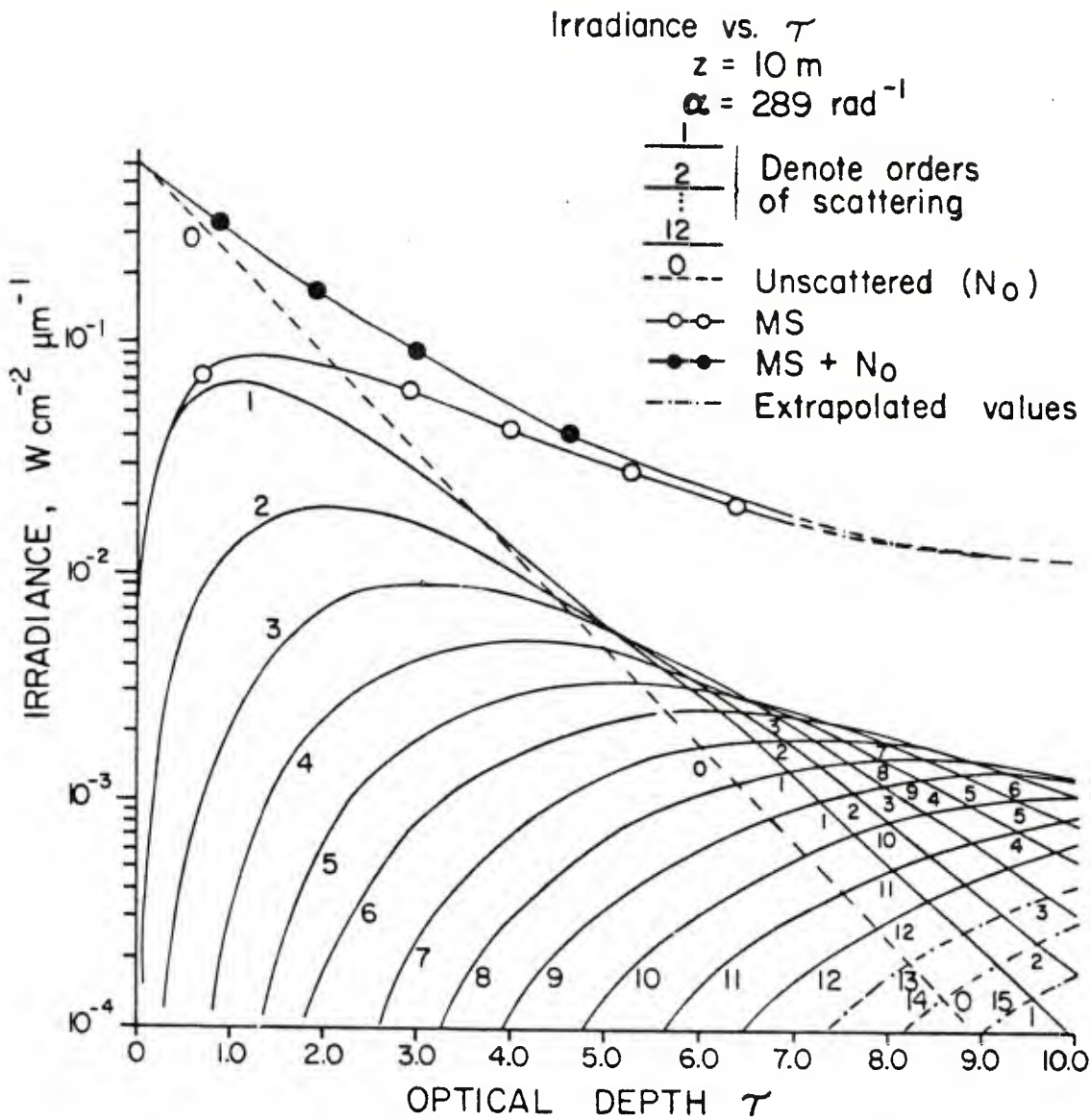


FIG. 10. The relative irradiance as a function of the optical depth  $\tau$ , showing the unscattered contribution (denoted by 0), contribution due to various orders of scattering (denoted by 1, 2, 3 ...), total scattered contribution (blank circles) and total scattered plus unscattered contributions (solid circles).

In this section we show the importance of higher order scatterings as related to the transmission of Gaussian laser beams through dense scattering media. The Conroy scheme used to obtain results from Eq. 14 differs from the Monte Carlo approach in that the points of integration are predetermined to achieve best convergence so that convergence is achieved at a faster rate than the Monte Carlo method, resulting in a lesser computational time. The formulations described earlier are based on the Gaussian representation of the scattering phase function in the forward direction, in which the essential factor is the width of the forward scattering lobe for monodisperse or polydisperse scatterers. Using the Conroy numerical scheme we have been able to obtain good theoretical results for optical depths  $\tau \leq 7.0$ . At  $\tau = 7.0$ , the contribution from the sixth order scattering peaks while at the same time scattering orders of up to 12 contribute appreciably to the total scattering (Fig. 10). Computations by the series method for the off-axis locations (e.g.,  $r = 2.0$  cm) of the open detector require the same number of integration points to achieve the same accuracy as required for the on-axis ( $r/W_o = 0$ ) case; whereas, by the Bessel function integration method, the number of integration points need to be increased for the off-axis locations, as explained earlier.

On the other hand, the alternative formulation of Eq. (2i), involving Bessel functions, cannot estimate the contributions of the different orders of scatterings although it is a powerful tool because it can compute the total scattering irrespective of the value of the optical depth as long as we are within a volume bounded by the surface described in Section 2.2 (ii).

From Fig. 10, we notice that for  $\tau \leq 0.1$ , only SS contributes to the total irradiance; for  $0.1 \leq \tau \leq 0.3$ , the second order contributions also needs to be included; and for  $\tau > 0.3$ , higher orders of scattering need to be taken into account. For example, for  $\tau \approx 2.0$ , the maximum contribution to irradiance is made by the first order scattering and that contributions from up to 5 orders of scattering are significant. Similarly, for  $\tau \approx 7.0$ , the maximum contribution is made by the 6th order scattering, and that contributions from up to 13 orders of scattering are significant. The contributions from the various orders of scattering seem to be enveloped by a curve which has a mode at about  $\tau \approx 1.0$ , and falls monotonically for  $\tau > 1.0$ . Similarly, the total scattered irradiance is given by a curve similar of similar shape, which has a mode at about  $\tau \approx 1.0$  and falls monotonically for  $\tau > 1.0$  but at a lesser rate than the previous envelope. The total irradiance received by the detector is given by the curve, obtained by adding the unscattered and scattered irradiances. The detector receives forward scattered radiation in addition to the direct radiation, thereby causing deviations from the Beer-Bouger's law (i.e., transmittance  $T = \exp(-\tau)$ ), which is represented by the dash line marked 0. This shows succinctly that the optical depth obtained from the transmissometer/radiometer measurements would not be the true value but an apparent optical depth. Therefore, in order to obtain the true optical depths, a forward scattering correction must be made to the transmissometer/radiometer measurements. A detailed discussion of the MS corrections as functions of the detector field of view and optical depths is given in Section 3 next.

### 3. MULTIPLE SCATTERING CORRECTIONS AS FUNCTIONS OF DETECTOR FIELD OF VIEW

#### 3.1 INTRODUCTION

In making optical extinction measurements by laser beams traversing aerosols, an error is always made because some forward scattered radiation invariably enters the detector's finite field of view. To determine the correction due to multiple scattering requires the solution of the radiation transfer equation. A fruitful approach to the problem has been a Monte Carlo technique, because it can handle strange geometries as well as inhomogeneities.<sup>16,25,59</sup> Recently, considerable attention has been paid to analytical solutions to the equation of transfer in a form appropriate for the laser beam propagation problem.<sup>22,24,47,48,60,61</sup> Although exact solutions have not been obtained to date, there are some special cases where simple and useful approximate solutions to the equation of transfer are available. For tenuous distribution of scatterers, the first-order multiple scattering theory can be used, and for dense distribution the diffusion approximation is appropriate. If the particle size is large compared with incident wavelength, the energy scattered by the particle is largely confined within a small angle in the forward direction and, therefore, by employing the small-angle approximation it is possible to simplify the equation of transfer. In Ref. 61, a systematic study of contributions of increasing order of scattering for both realistic and model aerosols has been conducted.

As indicated by Ishimaru,<sup>27,62</sup> the first-order multiple scattering approximation is applicable when the density of scatterers is so low that the diffuse (incoherent) intensity is considerably smaller than the reduced (coherent) intensity. This will certainly be the case if optical distance traversed by the beam is much smaller than unity. However, the same weak fluctuation case is also encountered in the situations where the receiver has a narrow receiving angle. In this case, the amount of scattered intensity entering into the receiver is small compared with the direct coherent intensity, and therefore the received field is predominantly coherent. The effect of the detector's finite field of view on the received power has been a subject of comprehensive investigations related to forward scattering corrections for optical extinction measurements.<sup>8,82-84</sup>

The purpose of this effort was to study the effect of a finite field of view on the intensity and the received power of a laser beam undergoing multiple scattering. Our analytic approach is based on the theory of Dolin<sup>63,64</sup> and Fante,<sup>20,65,66,69</sup> summarized in Section 3.2. In Sections 3.3 and 3.4, we apply this theory to Gaussian beams. Numerical results relevant to the beam propagation in a water cloud and model aerosol particles are presented in Section 3.5.

### 3.2 THE FANTE-DOLIN THEORY

Our considerations will be based on the equation of radiative transfer for the radiance (specific intensity) distribution function,  $I(\vec{\phi}, \vec{r}, z)$ . In the small angle approximation,  $I(\vec{\phi}, \vec{r}, z)$  satisfies

$$\vec{\phi} \cdot \frac{\partial I}{\partial \vec{r}} + \frac{\partial I}{\partial z} + \sigma I = \sigma_s \int P(\vec{\phi} - \vec{\phi}') I(\vec{\phi}', \vec{r}, z) d\vec{\phi}' \quad (1a)$$

where  $\sigma$  and  $\sigma_s$  are volume extinction and scattering coefficients ( $m^{-1}$ ) for the aerosol medium;  $\vec{r}$  is the component of the position vector transverse to the  $z$  axis; and  $\vec{\phi}$  is the transverse component of the unit propagation vector as shown in Fig. 1 in Section 2.2.

In the work of Dolin<sup>64</sup> and Fante,<sup>20,65,66,69</sup> which applies to sharply peaked phase functions,  $I(\vec{\phi}', \vec{r}, z)$  in the integrand on the right hand side of Eq. is expanded in Taylor series about  $\vec{\phi}' = \vec{\phi}$ . More precisely,  $I(\vec{\phi}, \vec{r}, z)$  is split into

$$I(\vec{\phi}, \vec{r}, z) = I^{(o)}(\vec{\phi}, \vec{r}, z) + I^{(s)}(\vec{\phi}, \vec{r}, z) \quad (30)$$

where superscripts  $o$  and  $s$  refer to unscattered and scattered radiance, respectively. Then, one expands

$$\begin{aligned} I^{(s)}(\vec{\phi}, \vec{r}, z) &= I^{(s)}(\vec{\phi}, \vec{r}, z) \\ &+ \sum_k (\phi' - \phi)_k \frac{\partial}{\partial \phi_k} I^{(s)}(\vec{\phi}, \vec{r}, z) \\ &+ \frac{1}{2} \sum_k \sum_l (\phi' - \phi)_k (\phi' - \phi)_l \frac{\partial^2}{\partial \phi_k \partial \phi_l} I^{(s)}(\vec{\phi}, \vec{r}, z) + \dots \end{aligned} \quad (31)$$

where  $k$  and  $l$  refer to the Cartesian components of the  $\vec{\phi}$  vector. Recall that  $\vec{\phi} = \phi_x \hat{x} + \phi_y \hat{y}$ .

Equation (1) now yields

$$\vec{\phi} \cdot \frac{\partial I^{(o)}}{\partial \vec{r}} + \frac{\partial I^{(o)}}{\partial z} + \sigma I^{(o)} = 0 \quad (32)$$

while  $I^{(s)}$  is determined from the nonhomogeneous equation

$$\vec{\phi} \cdot \frac{\partial I^{(s)}}{\partial \vec{r}} - \frac{\sigma\omega}{4} \langle \vec{\phi}^2 \rangle \nabla_{\vec{\phi}}^2 I^{(s)} + \frac{\partial I^{(s)}}{\partial z} + \sigma(1-\omega) I^{(s)} = \sigma\omega \int P(\vec{\phi} - \vec{\phi}') I^{(o)}(\vec{\phi}', \vec{r}, z) d^2\phi' \quad (33)$$

where  $\omega = \sigma_s/\sigma$  is the single scattering albedo; and  $\langle \vec{\phi}^2 \rangle$  is defined as

$$\langle \vec{\phi}^2 \rangle = \int P(\vec{\phi}) \vec{\phi}^2 d^2\phi \quad (34)$$

In deriving Eq.(33) we have neglected the terms of higher order than second in Eq. (31). The solutions to Eqs.(32) and (33) can be obtained by the method of characteristics in the Fourier space of the variables  $\vec{\phi}$  and  $\vec{r}$ . With the Fourier transforms defined generically as

$$\hat{I}(\vec{\xi}, \vec{\eta}, z) = \iint_{-\infty}^{\infty} d^2\phi d^2r I(\vec{\phi}, \vec{r}, z) e^{i(\vec{\xi} \cdot \vec{\phi} + \vec{\eta} \cdot \vec{r})} \quad (34)$$

$$\hat{P}(\vec{\xi}) = \int_{-\infty}^{\infty} d^2\phi P(\vec{\phi}) e^{i\vec{\xi} \cdot \vec{\phi}} \quad (35)$$

we obtain the following solutions

$$\hat{I}^{(o)}(\vec{\xi}, \vec{\eta}, z) = \hat{I}(\vec{\xi} + \vec{\eta}z, \vec{\eta}, z=0) e^{-\sigma z} \quad (36)$$

and

$$\begin{aligned} \hat{I}^{(s)}(\vec{\xi}, \vec{\eta}, z) &= \hat{I}(\vec{\xi} + \vec{\eta}z, \vec{\eta}, z=0) \int P[\vec{\xi} + \vec{\eta}(z-z')] e^{-\sigma z'} \\ &\cdot \exp \left\{ - \int_{z'}^z [\frac{\sigma\omega}{4} \langle \vec{\phi}^2 \rangle |\vec{\xi} + \vec{\eta}(z-z')|^2 + \sigma(1-\omega)] dz'' \right\} dz' \end{aligned} \quad (37)$$

for the unscattered and scattered contributions, respectively.

### 3.3 CASE OF COLLIMATED GAUSSIAN BEAM

We assume now that in the single scattering theory the scattering phase function  $P(\vec{\phi})$  is given by a Gaussian function, i.e.,

$$P(\vec{\phi}) = \frac{\alpha^2}{\pi} \exp(-\alpha^2 \vec{\phi}^2) \quad (2)$$

and that the incident collimated beam, directed along the  $z$  axis, has a Gaussian spatial form, i.e.,

$$I(\vec{\phi}, \vec{r}, z=0) = F_o \pi^{-1} \gamma^2 \delta^{(2)}(\vec{\phi}) \exp(-\gamma^2 \vec{r}^2) \quad (38)$$

where  $\delta^{(2)}$  is the Dirac delta function.

In the situation modeled by Eqs.(2) and (38), we obtain, after performing the inverse Fourier transforms of Eqs. (36) and (37), the explicit formulas for  $I^{(o)}(\vec{\phi}, \vec{r}, z)$  and  $I^{(s)}(\vec{\phi}, \vec{r}, z)$ . They read

$$I^{(o)}(\vec{\phi}, \vec{r}, z) = F_o \pi^{-1} e^{-\sigma z} e^{-\gamma^2 \vec{r}^2} \delta^{(2)}(\vec{\phi}) \quad (39)$$

and

$$\begin{aligned} I^{(s)}(\vec{\phi}, \vec{r}, z) &= \frac{F_o \sigma \omega e^{-\sigma z}}{(2\pi)^2} \int dz' [4 A(z') C(z') - B^2(z')]^{-1} \\ &\cdot \exp \left\{ -\frac{A(z') \vec{r}^2 - B(z') \vec{\phi} \cdot \vec{r} + C(z') \vec{\phi}^2}{4A(z')C(z') - B^2(z')} \right\} e^{\omega \sigma z'} \end{aligned} \quad (40)$$

where the functions  $A$ ,  $B$ , and  $C$  are defined as

$$\begin{aligned} A(z') &= \frac{1 + \sigma \omega z'}{4\alpha^2} \\ B(z') &= \frac{2z' + \sigma \omega z'^2}{4\alpha^2} \\ C(z') &= \frac{1}{4\gamma^2} + \frac{z'^2 + \sigma \omega z'^3/3}{4\alpha^2} \end{aligned} \quad (41)$$

In polar coordinates  $(\theta, b)$ , the vector  $\vec{\phi}$  can be expressed by

$$\begin{aligned}\phi_x &= \theta \cos b \\ \phi_y &= \theta \sin b\end{aligned}\quad (42)$$

For a detector having the field of view (FOV) half-angle,  $\theta_D$ , the received intensity is obtained from Eq. (40) after integration over the angle  $b$  in the range  $(0, 2\pi)$  and over  $\theta$  in the range  $(0, \theta_D)$ . The received intensity  $F^{(s)}(\theta_D, \vec{r}, \sigma z)$  corresponding to the scattered beam thus becomes

$$F^{(s)}(\theta_D, \vec{r}, \sigma z) = \int_0^{\theta_D} I^{(s)}(\theta, \vec{r}, \sigma z) \theta d\theta \quad (43)$$

where

$$\begin{aligned}I^{(s)}(\theta, \vec{r}, \sigma z) &= \frac{F_0 \omega e^{-\sigma z}}{2\pi} \int_0^{\sigma z} [4A(\frac{x}{\sigma})C(\frac{x}{\sigma}) - B^2(\frac{x}{\sigma})]^{-1} \\ &\cdot I_0 \left[ \frac{\theta r B(x/\sigma)}{4A(x/\sigma)C(x/\sigma) - B^2(x/\sigma)} \right] \\ &\cdot \exp \left[ -\frac{A(x/\sigma)r^2 + C(x/\sigma)\theta^2}{4A(x/\sigma)C(x/\sigma) - B^2(x/\sigma)} \right] e^{\omega x} dx\end{aligned}\quad (44)$$

Here  $I_0$  is the modified Bessel function of zeroth order, and  $x$  is a dimensionless integration variable.

The contribution coming from the unscattered part of the beam is

$$F^{(o)}(\theta_D, \vec{r}, \sigma z) = F_0 \pi^{-1} e^{-\sigma z} e^{-\gamma r^2} \quad (45)$$

It is thus seen that the numerical results can be extracted from this theory in a rather simple manner by performing merely a double integration.

### 3.4 CASE OF GENERAL GAUSSIAN BEAM

More generally, one can account both for the spatial and angular divergence of the laser beam assuming a Gaussian law of the form

$$I(\vec{\phi}, \vec{r}, z = 0) = F_0 \beta^2 \gamma^2 \pi^{-2} \exp(-\beta^2 \phi^2 - \gamma^2 r^2) \quad (46)$$

for the incident beam. Here, the parameter  $\beta$  describes the angular divergence.

By following exactly the same line of reasoning as in Section III, we obtain the following contributions  $F^{(s)}(\theta_D, \vec{r}, \sigma z)$  corresponding to the scattered beam, viz.,

$$F(s)(\theta_D, \vec{r}, \sigma z) = \theta_D^2 \int_0^1 I^{(s)}(\theta' \theta_D, \vec{r}, \sigma z) \theta' d\theta' \quad (47)$$

where

$$\begin{aligned} I^{(s)}(\theta, \vec{r}, \sigma z) &= F_0 \omega \sigma z e^{-\sigma z / 2\pi} \\ &\times \int_0^1 \left[ \frac{4A\{(x/\sigma) z\sigma\} C\{(x/\sigma) z\sigma\} - B^2\{(x/\sigma) z\sigma\}}{4A\{(x/\sigma) z\sigma\} C\{(x/\sigma) z\sigma\} - B^2\{(x/\sigma) z\sigma\}} \right]^{-1} \\ &\times I_0 \left[ \frac{\theta(\vec{r}) - B\{(x/\sigma) z\sigma\}/\gamma}{4A\{(x/\sigma) z\sigma\} C\{(x/\sigma) z\sigma\} - B^2\{(x/\sigma) z\sigma\}} \right] \\ &\times \exp \left[ - \frac{(\vec{r})^2 A\{(x/\sigma) z\sigma\}/\gamma^2 + C\{(x/\sigma) z\sigma\}\theta^2}{4A\{(x/\sigma) z\sigma\} C\{(x/\sigma) z\sigma\} - B^2\{(x/\sigma) z\sigma\}} \right] \\ &\times \exp(\omega x\sigma z) \cdot dx' \end{aligned} \quad (48)$$

and  $I_0$  is the modified Bessel function of zeroth order.

For the unscattered beam, we obtain

$$\begin{aligned}
 F^{(0)}(\theta_D, \gamma_r, \sigma z) &= 2F_0 \beta^2 \exp(-\sigma z) \theta_D^2 / \pi \\
 &+ \int_0^1 \theta' d\theta' I_0 \{2(\gamma/\sigma) \theta_D \theta' (\gamma_r) \sigma z\} \\
 &+ \exp \left\{ -(\gamma_r)^2 - \left[ (\gamma/\sigma)^2 (\sigma z)^2 + \beta^2 \right] \theta_D^2 \theta'^2 \right\} \quad (49)
 \end{aligned}$$

The integrals in Eqs. (48) and (49) have limits 0 and 1. This choice of limits anticipates the use of Gaussian quadrature in numerical computation.

### 3.5 NUMERICAL RESULTS

The numerical values for the on-axis intensities are given in Tables 4-7 and the corresponding plots are given in Figs. 11-14, in which we show the unscattered (reduced) intensity marked by squares, scattered (diffuse) intensity marked by circles, and total intensity, by triangles, on the beam axis for optical depth  $\tau = 1, 4, 7$ , and  $10$ , respectively. A divergent beam with the parameters  $\beta = 2\pi/(\gamma\lambda)$  and  $\gamma = 1.0 \text{ cm}^{-1}$  is assumed to be propagating in the Deirmendjian water cloud (Ref. 27) model Cl. For  $\lambda = 0.45 \mu\text{m}$ , the extinction coefficient is obtained from the Mie theory computations when a modified gamma distribution is taken for water cloud particle size distribution. One also obtained  $\alpha = 46.80 \text{ rad}^{-1}$  for the Gaussian fit to the phase function as shown in Fig. 5. For a coaxial detector, with a diameter  $R_D = 1.0 \text{ cm}$ , the same as the laser beam diameter, the intensity  $F$  becomes a function of  $\theta_D$  and  $z$ . We normalize the intensities by dividing out the factor  $F^{(0)}(\theta_D = \infty, z = 0)$ . For the sake

TABLE 4. Received Power and On-Axis Intensity as Functions of the Detector FOV for Deirmendjian's Water Cloud C1 Model, with  $\alpha = 46.80 \text{ rad}^{-1}$ ,  $\sigma = 1.66 \times 10^{-3} \text{ cm}^{-1}$ ,  $\omega = 1.0$ ,  $\lambda = 0.45 \mu\text{m}$ , Laser Beam Radius = 1.0cm, Detector Radius  $R_D = 1.0 \text{ cm}$ , and  $\tau = 1.0$ .

fov (rad)	optical depth= 1.00	pr-unscat.	pr-scatt.	pr-total	i-un	i-sc	i-tot
.00100	8.64644e-01	6.93418e-04	8.65337e-01	8.99923e-01	5.89179e-04	1.00051e+00	
.00200	8.64644e-01	2.74078e-03	8.67385e-01	9.99923e-01	2.32054e-03	1.00224e+00	
.00300	8.64644e-01	6.04651e-03	8.70690e-01	9.99923e-01	5.09003e-03	1.00501e+00	
.00400	8.64644e-01	1.04611e-02	8.75105e-01	9.99923e-01	8.73842e-03	1.00866e+00	
.00500	8.64644e-01	1.57946e-02	8.80439e-01	9.99923e-01	1.30698e-02	1.01299e+00	
.00600	8.64644e-01	2.18324e-02	8.86476e-01	9.99923e-01	1.78728e-02	1.01780e+00	
.00700	8.64644e-01	2.83520e-02	8.92996e-01	9.99923e-01	2.29407e-02	1.02286e+00	
.00800	8.64644e-01	3.51383e-02	8.99782e-01	9.99923e-01	2.80887e-02	1.02801e+00	
.00900	8.64644e-01	4.19965e-02	9.06640e-01	9.99923e-01	3.31646e-02	1.03309e+00	
.01000	8.64644e-01	4.87604e-02	9.13404e-01	9.99923e-01	3.80547e-02	1.03798e+00	
.01100	8.64644e-01	5.52973e-02	9.19941e-01	9.99923e-01	4.26834e-02	1.04261e+00	
.01200	8.64644e-01	6.15091e-02	9.26153e-01	9.99923e-01	4.70089e-02	1.04693e+00	
.01300	8.64644e-01	6.73301e-02	9.31974e-01	9.99923e-01	5.10167e-02	1.05094e+00	
.01400	8.64644e-01	7.27232e-02	9.37367e-01	9.99923e-01	5.47116e-02	1.05463e+00	
.01500	8.64644e-01	7.76742e-02	9.42318e-01	9.99923e-01	5.81105e-02	1.05803e+00	
.01600	8.64644e-01	8.21871e-02	9.46831e-01	9.99923e-01	6.12364e-02	1.06116e+00	
.01700	8.64644e-01	8.62785e-02	9.50922e-01	9.99923e-01	6.41138e-02	1.06404e+00	
.01800	8.64644e-01	8.99735e-02	9.54617e-01	9.99923e-01	6.67656e-02	1.06669e+00	
.01900	8.64644e-01	9.33018e-02	9.57946e-01	9.99923e-01	6.92119e-02	1.06913e+00	
.02000	8.64644e-01	9.62953e-02	9.60939e-01	9.99923e-01	7.14691e-02	1.07139e+00	
.02100	8.64644e-01	9.89859e-02	9.63630e-01	9.99923e-01	7.35504e-02	1.07347e+00	
.02200	8.64644e-01	1.01404e-01	9.66048e-01	9.99923e-01	7.54664e-02	1.07539e+00	
.02300	8.64644e-01	1.03578e-01	9.68222e-01	9.99923e-01	7.72256e-02	1.07715e+00	
.02400	8.64644e-01	1.05533e-01	9.70177e-01	9.99923e-01	7.88354e-02	1.07876e+00	
.02500	8.64644e-01	1.07291e-01	9.71935e-01	9.99923e-01	8.03025e-02	1.08023e+00	

#### Symbol Legend:

- fov denotes detector field of view
- pr-unscat. denotes unscattered received power
- pr-scatt. denotes scattered received power
- pr-total denotes total received power
- i-un denotes unscattered on-axis intensity
- i-sc denotes scattered on-axis intensity
- i-tot denotes total on-axis intensity
- e-01 denotes

TABLE 5. Same as Table 4, Except  $\tau = 4.0$ 

optical depth= 4.00	fov (rad)	pr-unscat.	pr-scat.	pr-total	i-un	i-sc	i-tot
.00100	8.64332e-01	7.61831e-04	8.65093e-01	9.98770e-01	6.63804e-04	9.39434e-01	
.00200	8.64332e-01	3.01907e-03	8.67351e-01	9.98770e-01	2.62024e-03	1.00139e+00	
.00300	8.64332e-01	6.68906e-03	8.71021e-01	9.98770e-01	5.76760e-03	1.00454e+00	
.00400	8.64332e-01	1.16408e-02	8.75972e-01	9.98770e-01	1.00872e+00		
.00500	8.64332e-01	1.77041e-02	8.82036e-02	9.98770e-01	1.49544e-02	1.01372e+00	
.00600	8.64332e-01	2.46810e-02	8.89013e-01	9.98770e-01	2.05615e-02	1.01933e+00	
.00700	8.64332e-01	3.23580e-02	8.96689e-01	9.98770e-01	2.65300e-02	1.02530e+00	
.00800	8.64332e-01	4.05176e-02	9.04849e-01	9.98770e-01	3.26302e-02	1.03140e+00	
.00900	8.64332e-01	4.89493e-02	9.13281e-01	9.98770e-01	3.86552e-02	1.03743e+00	
.01000	8.64332e-01	5.74575e-02	9.21789e-01	9.98770e-01	4.44314e-02	1.04320e+00	
.01100	8.64332e-01	6.58680e-02	9.30199e-01	9.98770e-01	4.98243e-02	1.04859e+00	
.01200	8.64332e-01	7.40317e-02	9.38363e-01	9.98770e-01	5.47410e-02	1.05351e+00	
.01300	8.64332e-01	8.18268e-02	9.46158e-01	9.98770e-01	5.91280e-02	1.05790e+00	
.01400	8.64332e-01	8.91583e-02	9.53490e-01	9.98770e-01	6.29668e-02	1.06174e+00	
.01500	8.64332e-01	9.59576e-02	9.60289e-01	9.98770e-01	6.62675e-02	1.06504e+00	
.01600	8.64332e-01	1.02180e-01	9.66512e-01	9.98770e-01	6.90616e-02	1.06783e+00	
.01700	8.64332e-01	1.07804e-01	9.72135e-01	9.98770e-01	7.13949e-02	1.07017e+00	
.01800	8.64332e-01	1.12824e-01	9.77115e-01	9.98770e-01	7.33215e-02	1.07209e+00	
.01900	8.64332e-01	1.17254e-01	9.81586e-01	9.98770e-01	7.48977e-02	1.07367e+00	
.02000	8.64332e-01	1.21120e-01	9.85452e-01	9.98770e-01	7.61787e-02	1.07495e+00	
.02100	8.64332e-01	1.24458e-01	9.88790e-01	9.98770e-01	7.72156e-02	1.07599e+00	
.02200	8.64332e-01	1.27311e-01	9.91642e-01	9.98770e-01	7.80536e-02	1.07682e+00	
.02300	8.64332e-01	1.29726e-01	9.94058e-01	9.98770e-01	7.887315e-02	1.07750e+00	
.02400	8.64332e-01	1.31754e-01	9.96085e-01	9.98770e-01	7.92816e-02	1.07805e+00	
.02500	8.64332e-01	1.33443e-01	9.97775e-01	9.98770e-01	7.97301e-02	1.07850e+00	

TABLE 6. Same as Table 4, Except  $\tau = 7.0$ 

fov (rad)	optical depth = 7.00	pr-unscat.	pr-scatt.	pr-total	i-un	i-sc	i-tot
.00100	8.63644e-01	9.51905e-04	8.64596e-01	9.96244e-01	7.52899e-04	9.96997e-01	
.00200	8.63644e-01	3.76558e-03	8.67410e-01	9.96244e-01	2.95184e-03	9.99196e-01	
.00300	8.63644e-01	8.31783e-03	8.71962e-01	9.96244e-01	6.42609e-03	1.00267e+00	
.00400	8.63644e-01	1.44128e-02	8.78057e-01	9.96244e-01	1.09178e-02	1.00716e+00	
.00500	8.63644e-01	2.17955e-02	8.85440e-01	9.96244e-01	1.61165e-02	1.01236e+00	
.00600	8.63644e-01	3.01693e-02	8.93814e-01	9.96244e-01	2.16979e-02	1.01794e+00	
.00700	8.63644e-01	3.92164e-02	9.02861e-01	9.96244e-01	2.73594e-02	1.02360e+00	
.00800	8.63644e-01	4.86183e-02	9.12263e-01	9.96244e-01	3.28487e-02	1.02909e+00	
.00900	8.63644e-01	5.80765e-02	9.21721e-01	9.96244e-01	3.79798e-02	1.03422e+00	
.01000	8.63644e-01	6.73291e-02	9.30973e-01	9.96244e-01	4.26379e-02	1.03888e+00	
.01100	8.63644e-01	7.61637e-02	9.39808e-01	9.96244e-01	4.67735e-02	1.04302e+00	
.01200	8.63644e-01	8.44245e-02	9.48069e-01	9.96244e-01	5.03904e-02	1.04663e+00	
.01300	8.63644e-01	9.20138e-02	9.55658e-01	9.96244e-01	5.35293e-02	1.04977e+00	
.01400	8.63644e-01	9.88882e-02	9.62533e-01	9.96244e-01	5.62521e-02	1.05250e+00	
.01500	8.63644e-01	1.05051e-01	9.68695e-01	9.96244e-01	5.86284e-02	1.05487e+00	
.01600	8.63644e-01	1.10539e-01	9.74184e-01	9.96244e-01	6.07256e-02	1.05697e+00	
.01700	8.63644e-01	1.15416e-01	9.79061e-01	9.96244e-01	6.26027e-02	1.05885e+00	
.01800	8.63644e-01	1.19757e-01	9.83401e-01	9.96244e-01	6.43079e-02	1.06055e+00	
.01900	8.63644e-01	1.23639e-01	9.87284e-01	9.96244e-01	6.58782e-02	1.06212e+00	
.02000	8.63644e-01	1.27137e-01	9.90782e-01	9.96244e-01	6.73405e-02	1.06358e+00	
.02100	8.63644e-01	1.30317e-01	9.93961e-01	9.96244e-01	6.87137e-02	1.06496e+00	
.02200	8.63644e-01	1.33232e-01	9.96876e-01	9.96244e-01	7.00106e-02	1.06625e+00	
.02300	8.63644e-01	1.35927e-01	9.99571e-01	9.96244e-01	7.12395e-02	1.06748e+00	
.02400	8.63644e-01	1.38434e-01	1.00208e+00	9.96244e-01	7.24062e-02	1.06865e+00	
.02500	8.63644e-01	1.40778e-01	1.00442e+00	9.96244e-01	7.35141e-02	1.06976e+00	

TABLE 7. Same as Table 4, Except  $\tau = 10.0$

fov (rad)	optical depth= 10.00	pr-unscat.	pr-scat.	pr-total	i-un	i-sc	i-tot
.00100	8.62582e-01	1.32122e-03	8.63903e-01	9.92365e-01	8.27520e-04	9.93192e-01	
.00200	8.62582e-01	5.22432e-03	8.67807e-01	9.92365e-01	3.25100e-03	9.95616e-01	
.00300	8.62582e-01	1.15339e-02	8.74116e-01	9.92365e-01	7.10270e-03	9.99467e-01	
.00400	8.62582e-01	1.99779e-02	8.82560e-01	9.92365e-01	1.21325e-02	1.00450e+00	
.00500	8.62582e-01	3.02143e-02	8.92797e-01	9.92365e-01	1.80451e-02	1.01041e+00	
.00600	8.62582e-01	4.18646e-02	9.04447e-01	9.92365e-01	2.45404e-02	1.01691e+00	
.00700	8.62582e-01	5.45468e-02	9.17129e-01	9.92365e-01	3.13486e-02	1.02371e+00	
.00800	8.62582e-01	6.79063e-02	9.30488e-01	9.92365e-01	3.82550e-02	1.03062e+00	
.00900	8.62582e-01	8.16396e-02	9.44222e-01	9.92365e-01	4.51119e-02	1.03748e+00	
.01000	8.62582e-01	9.55087e-02	9.58091e-01	9.92365e-01	5.18371e-02	1.04420e+00	
.01100	8.62582e-01	1.09346e-01	9.71929e-01	9.92365e-01	5.84033e-02	1.05077e+00	
.01200	8.62582e-01	1.23052e-01	9.85634e-01	9.92365e-01	6.48225e-02	1.05719e+00	
.01300	8.62582e-01	1.36580e-01	9.99162e-01	9.92365e-01	7.11291e-02	1.06349e+00	
.01400	8.62582e-01	1.49928e-01	1.01251e+00	9.92365e-01	7.73653e-02	1.06973e+00	
.01500	8.62582e-01	1.63119e-01	1.02570e+00	9.92365e-01	8.35704e-02	1.07594e+00	
.01600	8.62582e-01	1.76186e-01	1.03877e+00	9.92365e-01	8.97747e-02	1.08214e+00	
.01700	8.62582e-01	1.89164e-01	1.05175e+00	9.92365e-01	9.59972e-02	1.08836e+00	
.01800	8.62582e-01	2.02081e-01	1.06466e+00	9.92365e-01	1.02246e-01	1.09461e+00	
.01900	8.62582e-01	2.14953e-01	1.07754e+00	9.92365e-01	1.08519e-01	1.10088e+00	
.02000	8.62582e-01	2.27784e-01	1.09037e+00	9.92365e-01	1.14807e-01	1.10717e+00	
.02100	8.62582e-01	2.40566e-01	1.10315e+00	9.92365e-01	1.21099e-01	1.11346e+00	
.02200	8.62582e-01	2.53284e-01	1.11587e+00	9.92365e-01	1.27378e-01	1.11974e+00	
.02300	8.62582e-01	2.65913e-01	1.12849e+00	9.92365e-01	1.33626e-01	1.12599e+00	
.02400	8.62582e-01	2.78427e-01	1.14101e+00	9.92365e-01	1.39826e-01	1.13219e+00	
.02500	8.62582e-01	2.90796e-01	1.15338e+00	9.92365e-01	1.45961e-01	1.13833e+00	

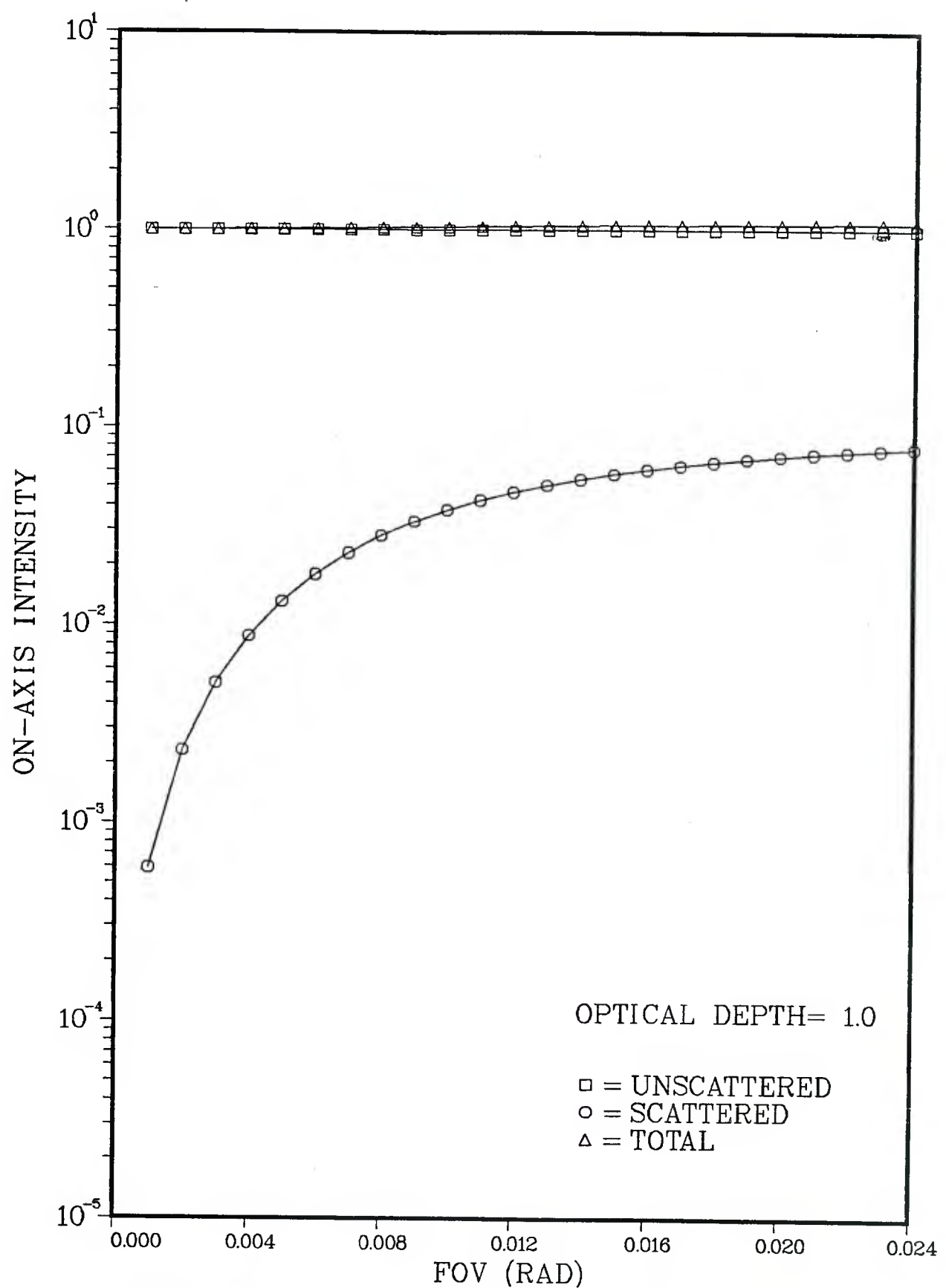


Fig. 11: Normalized intensity on the beam axis as function of detector FOV corresponding to Table 4 for  $\alpha = 46.80 \text{ rad}^{-1}$ ,  $R_D = 1.0 \text{ cm}$ , and  $\tau = 1.0$ .

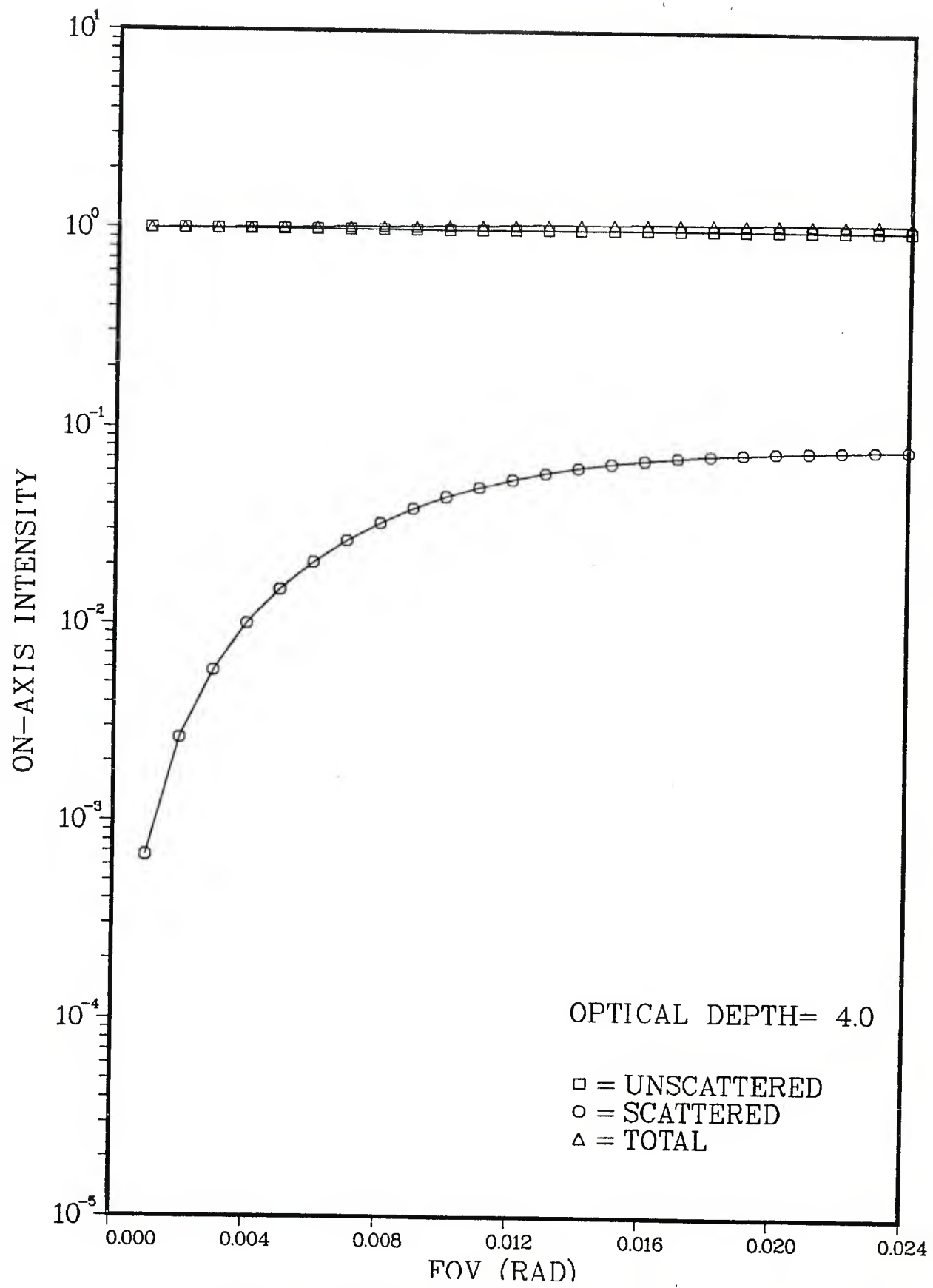


Fig. 12: Normalized intensity on the beam axis as function of detector FOV corresponding to Table 5 for  $\alpha = 46.80 \text{ rad}^{-1}$ ,  $R_D = 1.0 \text{ cm}$ , and  $\tau = 4.0$ .

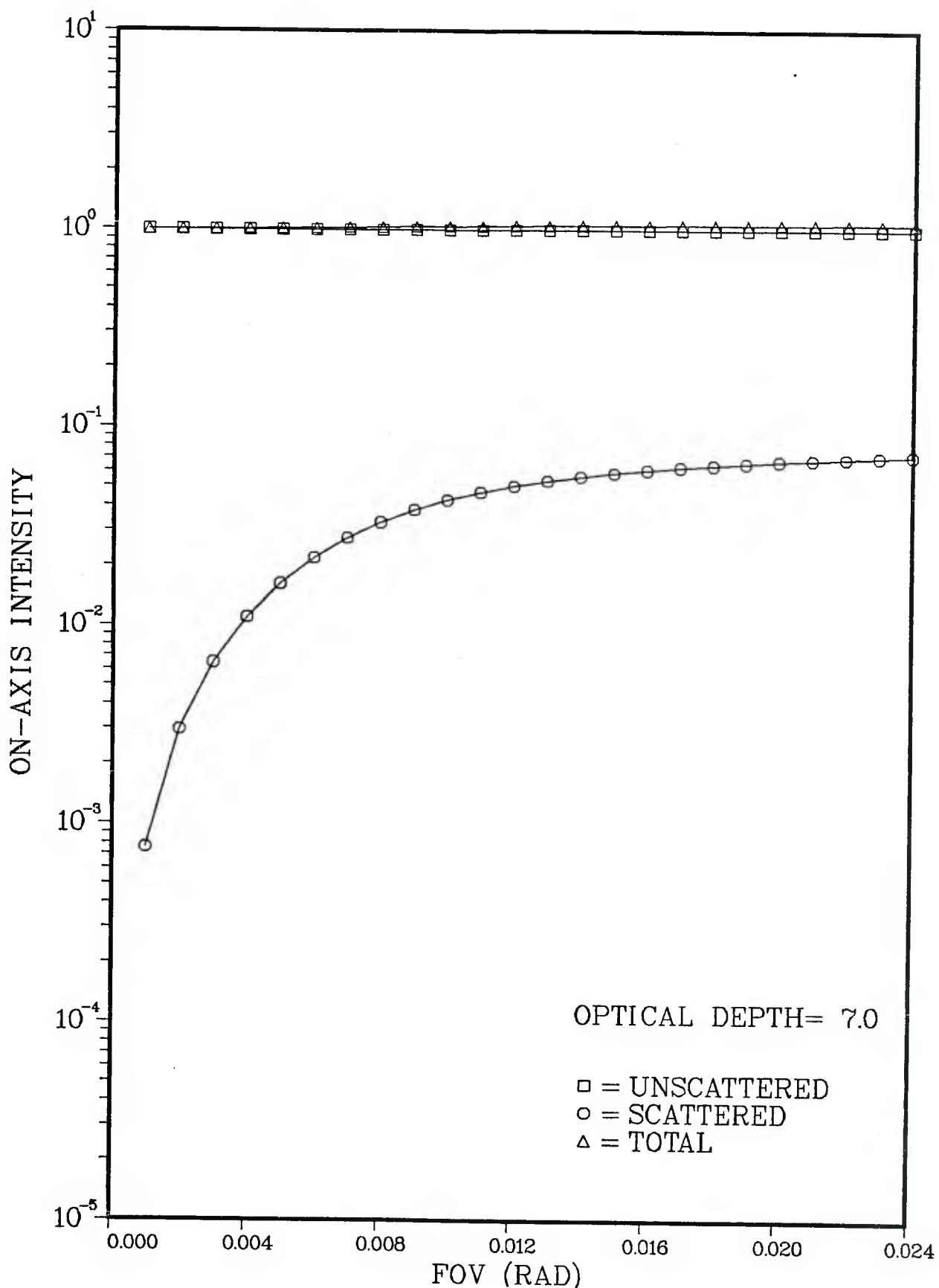


Fig. 13: Normalized intensity on the beam axis as function of detector FOV corresponding to Table 6 for  $\alpha = 46.80 \text{ rad}^{-1}$ ,  $R_D = 1.0 \text{ cm}$ , and  $\tau = 7.0$ .

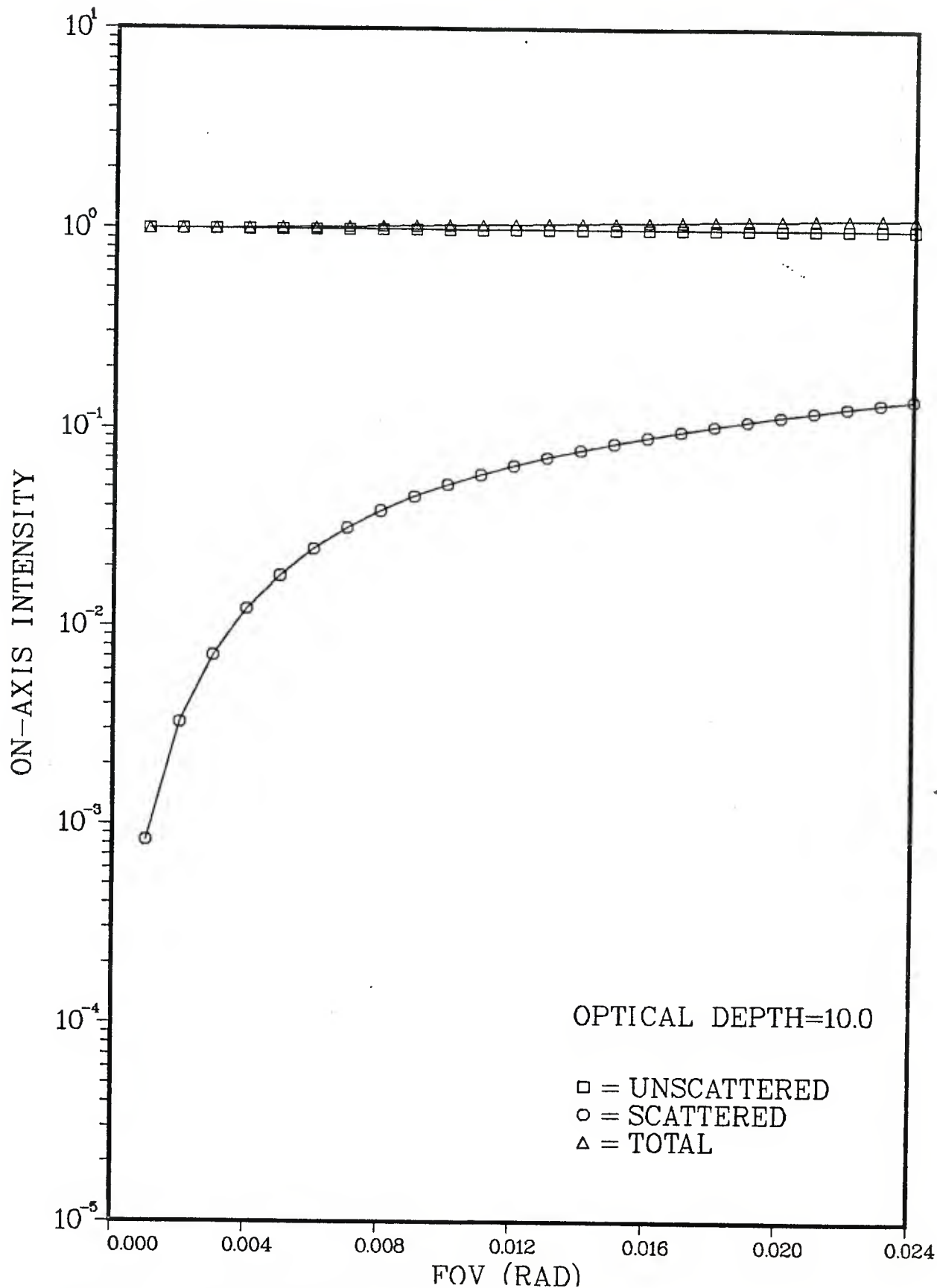


Fig. 14: Normalized intensity on the beam axis as function of detector FOV corresponding to Table 7 for  $\alpha = 46.80 \text{ rad}^{-1}$ ,  $R_D = 1.0 \text{ cm}$ , and  $\tau = 10.0$ .

of clarity in graphical presentation, we also scale the normalized intensities by the multiplicative factor  $\exp(\tau)$ .

In order to investigate the significance of the optical thickness, we calculated the power received by a coaxial detector of radius  $R_D = 1 \text{ cm}$ . If  $F(\theta_D, \vec{r}, \tau)$  denotes generically the beam intensity, then the received power is defined as

$$P(R_D) = 2\pi \int_0^{R_D} F(\theta_D, \vec{r}, \tau) r dr \quad (50)$$

The received power is also scaled by the multiplicative factor  $\exp(\tau)$ , and the power received at  $z = 0$  is divided out. The numerical values for received power for a coaxial detector of diameter  $R_D = 1 \text{ cm}$  are given in Tables 4-7, and the situation is depicted in Figs. 15-18 corresponding to the same parameters as in Figs. 11-14, respectively. As the FOV increases, both the intensity and the received power saturate rapidly, independently of the optical depth. This corresponds to the situation of an open detector. The contribution of the scattered power becomes dominant in the saturation region for optical depth of the order of 10.

Gaussian phase functions as given by Eq. (2) were best fitted to the exact Mie phase functions for monodisperse aerosols with radii in the range from 2.01 to  $40.2 \mu\text{m}$ . In Tables 8-11 and Figs. 19-22, we show the intensity vs. detector's FOV, and in Tables 8-11 and Figs. 23-26, the received power vs. FOV. Both these sets of results were computed for the model particles characterized by the parameters  $\alpha = 289.33 \text{ rad}^{-1}$ , and  $\sigma = 5.0 \times 10^{-2} \text{ cm}^{-1}$

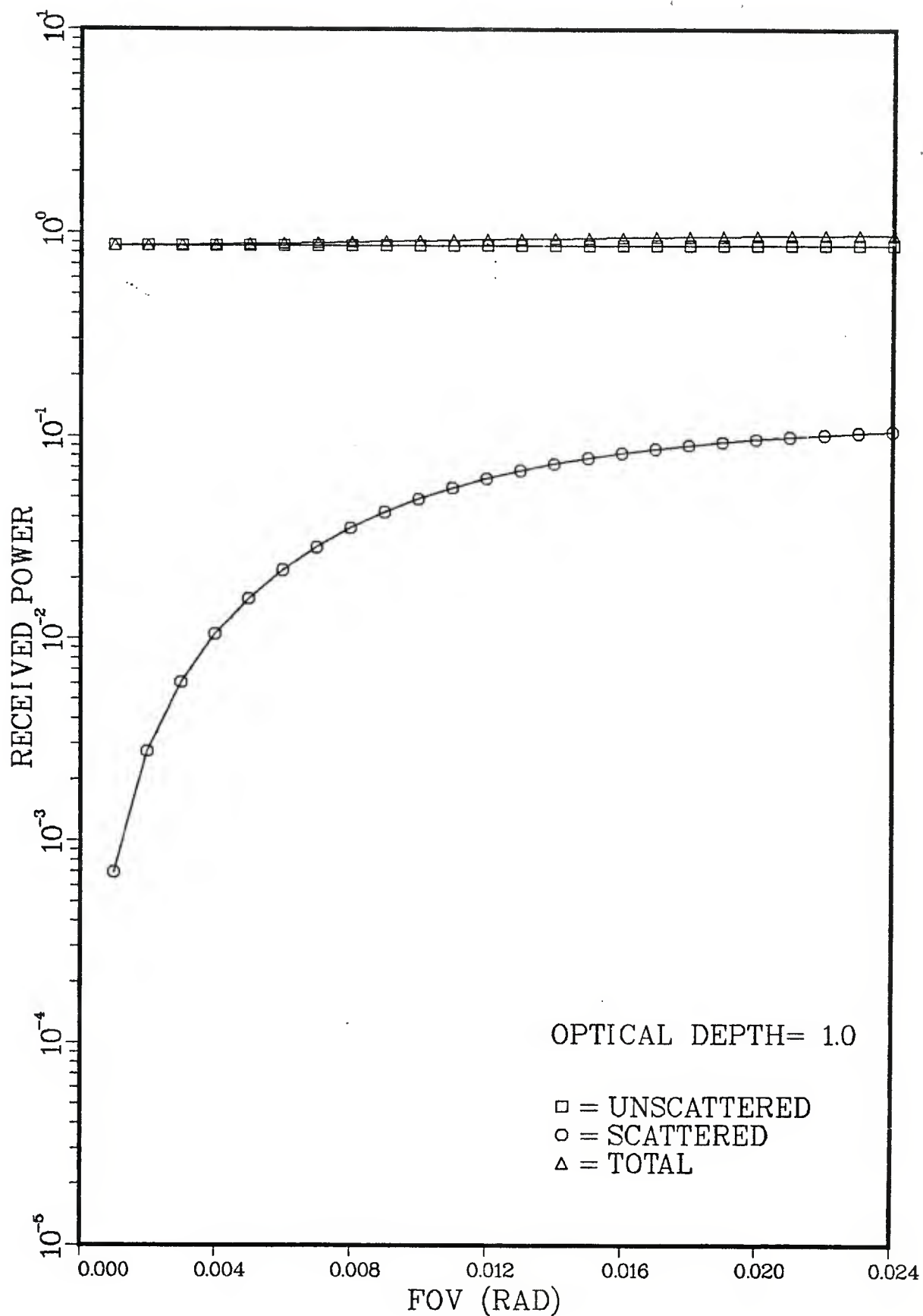


Fig. 1.5: Received power (arbitrary units) on the beam axis as function of detector FOV corresponding to Table 4 for  $\alpha = 46.80 \text{ rad}^{-1}$ ,  $R_D = 1.0 \text{ cm}$ , and  $\tau = 1.0$ .

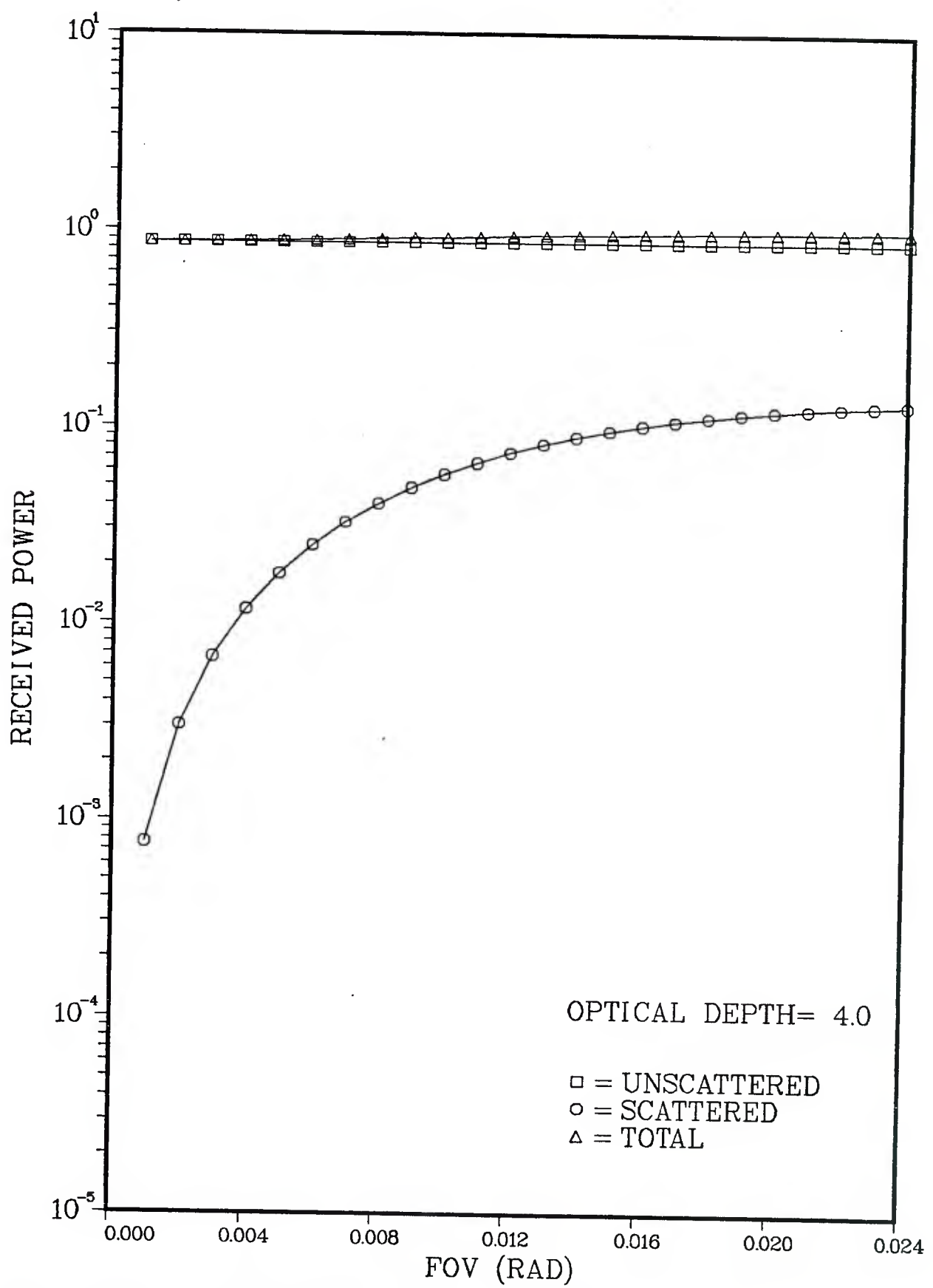


Fig. 16: Received power (arbitrary units) on the beam axis as function of detector FOV corresponding to Table 5 for  $\alpha = 46.80 \text{ rad}^{-1}$ ,  $R_D = 1.0 \text{ cm}$ , and  $\tau = 4.0$ .

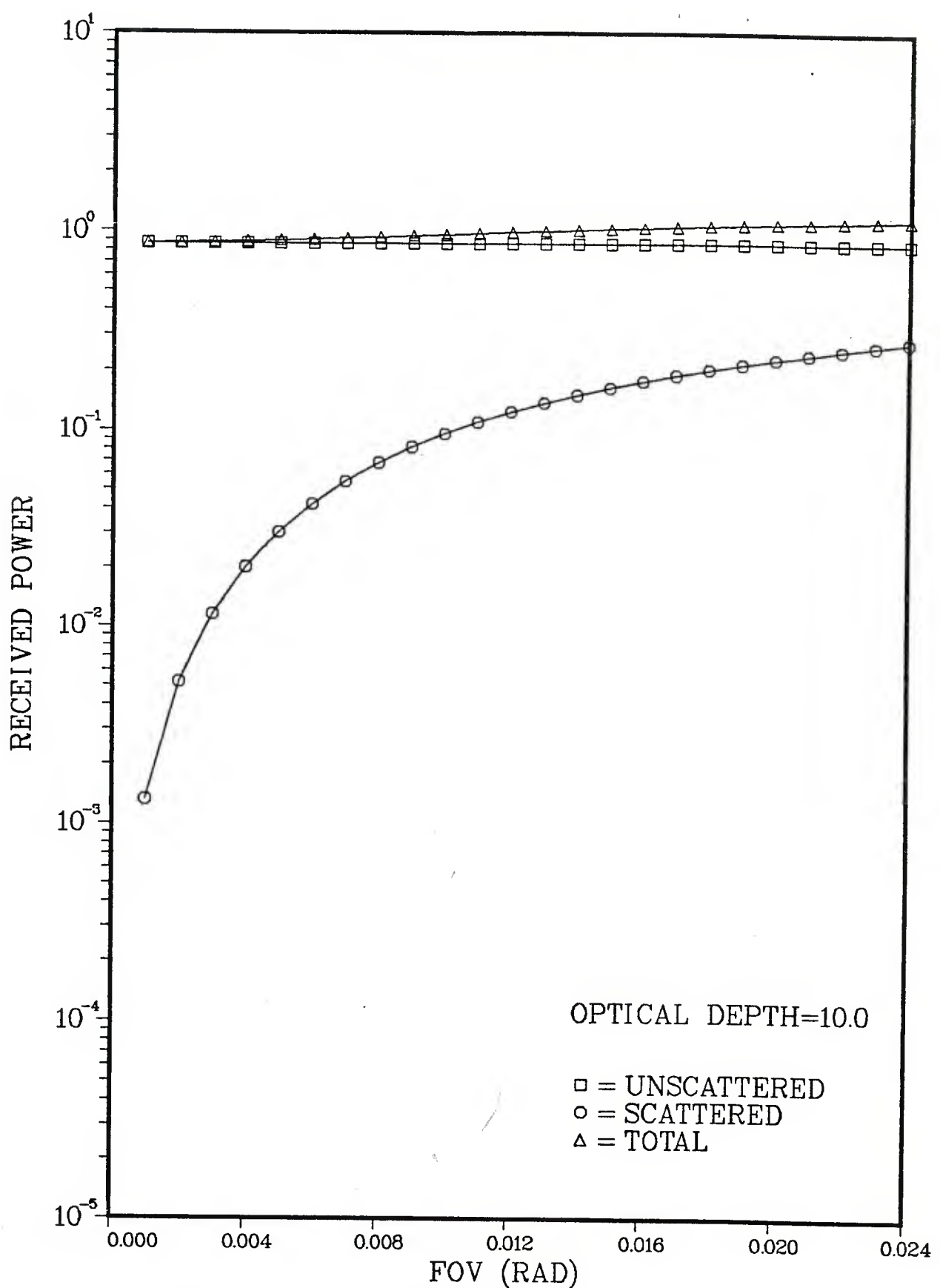


Fig. 18: Received power (arbitrary units) on the beam axis as function of detector FOV corresponding to Table 7 for  $\alpha = 46.80 \text{ rad}^{-1}$ ,  $R_D = 1.0 \text{ cm}$ , and  $\tau = 10.0$ .

TABLE 8. Received Power and On-Axis Intensity as Functions of the Detector FOV for Large Size Monodispersions with  $\alpha = 289.33 \text{ rad}^{-1}$ ,  $\sigma = 4 \times 10^{-3} \text{ cm}^{-1}$ ,  $\omega = 1.0$ ,  $\lambda = 0.45 \mu\text{m}$ ,  
Laser Beam Radius = 1.0 cm, Detector Radius  $R_D = 1.0 \text{ cm}$ , and  $\tau = 1.0$ .

optical depth= 1.00	fov (rad)	pr-unscat.	pr-scatt.	pr-total	i-un	i-sc	i-tot
.00050	8.64662e-01	1.98527e-02	8.84515e-01	9.99992e-01	2.22331e-02	1.02222e+00	
.00100	8.64662e-01	7.75393e-02	9.42202e-01	9.99992e-01	8.64919e-02	1.08648e+00	
.00150	8.64662e-01	1.67739e-01	1.03240e+00	9.99992e-01	1.85899e-01	1.18589e+00	
.00200	8.64662e-01	2.82497e-01	1.14716e+00	9.99992e-01	3.10359e-01	1.31035e+00	
.00250	8.64662e-01	4.12391e-01	1.27705e+00	9.99992e-01	4.4825e-01	1.44825e+00	
.00300	8.64662e-01	5.47807e-01	1.41241e+00	9.99992e-01	5.88225e-01	1.58822e+00	
.00350	8.64662e-01	6.80090e-01	1.54475e+00	9.99992e-01	7.20656e-01	1.72065e+00	
.00400	8.64662e-01	8.02379e-01	1.66704e+00	9.99992e-01	8.38621e-01	1.83861e+00	
.00450	8.64662e-01	9.10047e-01	1.77471e+00	9.99992e-01	9.38204e-01	1.93820e+00	
.00500	8.64662e-01	1.00073e+00	1.86540e+00	9.99992e-01	1.01825e+00	2.01824e+00	
.00550	8.64662e-01	1.07406e+00	1.93872e+00	9.99992e-01	1.07977e+00	2.07976e+00	
.00600	8.64662e-01	1.13114e+00	1.99580e+00	9.99992e-01	1.12512e+00	2.12511e+00	
.00650	8.64662e-01	1.17405e+00	2.03871e+00	9.99992e-01	1.15733e+00	2.15733e+00	
.00700	8.64662e-01	1.20527e+00	2.06994e+00	9.99992e-01	1.17946e+00	2.17946e+00	
.00750	8.64662e-01	1.22736e+00	2.09202e+00	9.99992e-01	1.19424e+00	2.19424e+00	
.00800	8.64662e-01	1.24259e+00	2.10725e+00	9.99992e-01	1.20390e+00	2.20389e+00	
.00850	8.64662e-01	1.25288e+00	2.11754e+00	9.99992e-01	1.21011e+00	2.21010e+00	
.00900	8.64662e-01	1.25973e+00	2.12439e+00	9.99992e-01	1.21406e+00	2.21406e+00	
.00950	8.64662e-01	1.26424e+00	2.12890e+00	9.99992e-01	1.21658e+00	2.21657e+00	
.01000	8.64662e-01	1.26720e+00	2.13187e+00	9.99992e-01	1.21817e+00	2.21816e+00	
.01050	8.64662e-01	1.26914e+00	2.13381e+00	9.99992e-01	1.21919e+00	2.21918e+00	
.01100	8.64662e-01	1.27042e+00	2.13508e+00	9.99992e-01	1.21983e+00	2.21983e+00	
.01150	8.64662e-01	1.27126e+00	2.13592e+00	9.99992e-01	1.22024e+00	2.22024e+00	
.01200	8.64662e-01	1.27181e+00	2.13647e+00	9.99992e-01	1.22051e+00	2.22050e+00	
.01250	8.64662e-01	1.27217e+00	2.13683e+00	9.99992e-01	1.22067e+00	2.22066e+00	

TABLE 9. Same as Table 8, Except  $\tau = 4.0$

optical depth = 4.00

fov (rad)	pr-unscat.	pr-scatt.	pr-total	i-un	i-sc	i-tot
.00050	8.64629e-01	1.19802e-01	9.84432e-01	9.99869e-01	9.07773e-02	1.09065e+00
.00100	8.64629e-01	4.67565e-01	1.33219e+00	9.99869e-01	3.52279e-01	1.35215e+00
.00150	8.64629e-01	1.01020e+00	1.87483e+00	9.99869e-01	7.54168e-01	1.75404e+00
.00200	8.64629e-01	1.69834e+00	2.56297e+00	9.99869e-01	1.25246e+00	2.25232e+00
.00250	8.64629e-01	2.47366e+00	3.33829e+00	9.99869e-01	1.79750e+00	2.79737e+00
.00300	8.64629e-01	3.27701e+00	4.14163e+00	9.99869e-01	2.34212e+00	3.34199e+00
.00350	8.64629e-01	4.05559e+00	4.92022e+00	9.99869e-01	2.84801e+00	3.84788e+00
.00400	8.64629e-01	4.76828e+00	5.63291e+00	9.99869e-01	3.28938e+00	4.28925e+00
.00450	8.64629e-01	5.38826e+00	6.25289e+00	9.99869e-01	3.65359e+00	4.65346e+00
.00500	8.64629e-01	5.90300e+00	6.76763e+00	9.99869e-01	3.93932e+00	4.93919e+00
.00550	8.64629e-01	6.31228e+00	7.17691e+00	9.99869e-01	4.15341e+00	5.15328e+00
.00600	8.64629e-01	6.62488e+00	7.48951e+00	9.99869e-01	4.30728e+00	5.30715e+00
.00650	8.64629e-01	6.85491e+00	7.71954e+00	9.99869e-01	4.41385e+00	5.41372e+00
.00700	8.64629e-01	7.01855e+00	7.88318e+00	9.99869e-01	4.48535e+00	5.48522e+00
.00750	8.64629e-01	7.13155e+00	7.99618e+00	9.99869e-01	4.53210e+00	5.53197e+00
.00800	8.64629e-01	7.20766e+00	8.07229e+00	9.99869e-01	4.56208e+00	5.56194e+00
.00850	8.64629e-01	7.25794e+00	8.12257e+00	9.99869e-01	4.58106e+00	5.58093e+00
.00900	8.64629e-01	7.29072e+00	8.15535e+00	9.99869e-01	4.59300e+00	5.59287e+00
.00950	8.64629e-01	7.31196e+00	8.17659e+00	9.99869e-01	4.60050e+00	5.60037e+00
.01000	8.64629e-01	7.32568e+00	8.19031e+00	9.99869e-01	4.60522e+00	5.60509e+00
.01050	8.64629e-01	7.33456e+00	8.19919e+00	9.99869e-01	4.60819e+00	5.60806e+00
.01100	8.64629e-01	7.34031e+00	8.20494e+00	9.99869e-01	4.61006e+00	5.60993e+00
.01150	8.64629e-01	7.34404e+00	8.20867e+00	9.99869e-01	4.61123e+00	5.61110e+00
.01200	8.64629e-01	7.34646e+00	8.21109e+00	9.99869e-01	4.61195e+00	5.61182e+00
.01250	8.64629e-01	7.34803e+00	8.21266e+00	9.99869e-01	4.61237e+00	5.61224e+00

TABLE 10. Same as Table 8, Except  $\tau = 4.0$ 

fov (rad)	pr-unscat.	pr-scatt.	pr-total	i-un	i-sc	i-tot
0.00050	8.64556e-01	3.68071e-01	1.23263e+00	9.99598e-01	2.20229e-01	1.21983e+00
.00100	8.64556e-01	1.44243e+00	2.30698e+00	9.99598e-01	8.60204e-01	1.85980e+00
.00150	8.64556e-01	3.13761e+00	4.00216e+00	9.99598e-01	1.86122e+00	2.86081e+00
.00200	8.64556e-01	5.32401e+00	6.18857e+00	9.99598e-01	3.13600e+00	4.13560e+00
.00250	8.64556e-01	7.84467e+00	8.70923e+00	9.99598e-01	4.58199e+00	5.58156e+00
.00300	8.64556e-01	1.05341e+01	1.13987e+01	9.99598e-01	6.09547e+00	7.09507e+00
.00350	8.64556e-01	1.32364e+01	1.41009e+01	9.99598e-01	7.58384e+00	8.58343e+00
.00400	8.64556e-01	1.58192e+01	1.66838e+01	9.99598e-01	8.97409e+00	9.97369e+00
.00450	8.64556e-01	1.81831e+01	1.90477e+01	9.99598e-01	1.02167e+01	1.12163e+01
.00500	8.64556e-01	2.02647e+01	2.11292e+01	9.99598e-01	1.12854e+01	1.22850e+01
.00550	8.64556e-01	2.20345e+01	2.28991e+01	9.99598e-01	1.21736e+01	1.31732e+01
.00600	8.64556e-01	2.34920e+01	2.43566e+01	9.99598e-01	1.28898e+01	1.38894e+01
.00650	8.64556e-01	2.46578e+01	2.55224e+01	9.99598e-01	1.34517e+01	1.44513e+01
.00700	8.64556e-01	2.55659e+01	2.64304e+01	9.99598e-01	1.38821e+01	1.48817e+01
.00750	8.64556e-01	2.62564e+01	2.71209e+01	9.99598e-01	1.42048e+01	1.52044e+01
.00800	8.64556e-01	2.67703e+01	2.76349e+01	9.99598e-01	1.44420e+01	1.54416e+01
.00850	8.64556e-01	2.71458e+01	2.80103e+01	9.99598e-01	1.46136e+01	1.56132e+01
.00900	8.64556e-01	2.74157e+01	2.82803e+01	9.99598e-01	1.47360e+01	1.57356e+01
.00950	8.64556e-01	2.76073e+01	2.84719e+01	9.99598e-01	1.48222e+01	1.58218e+01
.01000	8.64556e-01	2.77419e+01	2.86064e+01	9.99598e-01	1.48824e+01	1.58820e+01
.01050	8.64556e-01	2.78357e+01	2.87003e+01	9.99598e-01	1.49241e+01	1.59237e+01
.01100	8.64556e-01	2.79009e+01	2.87655e+01	9.99598e-01	1.49530e+01	1.59526e+01
.01150	8.64556e-01	2.79460e+01	2.88106e+01	9.99598e-01	1.49728e+01	1.59724e+01
.01200	8.64556e-01	2.79772e+01	2.88418e+01	9.99598e-01	1.49865e+01	1.59861e+01
.01250	8.64556e-01	2.79989e+01	2.88634e+01	9.99598e-01	1.49959e+01	1.59955e+01

TABLE 11. Same as Table 8, Except  $\tau = 4.0$

optical depth= 10.00

fov (rad)	pr-unscat.	pr-scatt.	pr-total	i-un	i-sc	i-tot
.00050	8.64443e-01	1.55944e+00	2.42389e+00	9.99180e-01	8.20988e-01	1.82017e+00
.00100	8.64443e-01	6.14684e+00	7.01129e+00	9.99180e-01	3.23206e+00	4.23124e+00
.00150	8.64443e-01	1.34987e+01	1.43632e+01	9.99180e-01	7.08365e+00	8.08283e+00
.00200	8.64443e-01	2.32057e+01	2.40702e+01	9.99180e-01	1.21458e+01	1.31450e+01
.00250	8.64443e-01	3.47523e+01	3.56168e+01	9.99180e-01	1.81335e+01	1.91326e+01
.00300	8.64443e-01	4.75645e+01	4.84289e+01	9.99180e-01	2.47352e+01	2.57343e+01
.00350	8.64443e-01	6.10582e+01	6.19226e+01	9.99180e-01	3.16413e+01	3.26405e+01
.00400	8.64443e-01	7.46836e+01	7.55480e+01	9.99180e-01	3.85677e+01	3.95669e+01
.00450	8.64443e-01	8.79598e+01	8.88243e+01	9.99180e-01	4.52729e+01	4.62720e+01
.00500	8.64443e-01	1.00498e+02	1.01363e+02	9.99180e-01	5.15675e+01	5.25667e+01
.00550	8.64443e-01	1.12014e+02	1.12879e+02	9.99180e-01	5.73177e+01	5.83169e+01
.00600	8.64443e-01	1.22325e+02	1.23190e+02	9.99180e-01	6.34415e+01	6.44423e+01
.00650	8.64443e-01	1.31345e+02	1.32209e+02	9.99180e-01	6.69070e+01	6.79062e+01
.00700	8.64443e-01	1.39065e+02	1.39930e+02	9.99180e-01	7.07156e+01	7.17147e+01
.00750	8.64443e-01	1.45542e+02	1.46406e+02	9.99180e-01	7.39009e+01	7.49001e+01
.00800	8.64443e-01	1.50873e+02	1.51737e+02	9.99180e-01	7.65162e+01	7.75154e+01
.00850	8.64443e-01	1.55184e+02	1.56049e+02	9.99180e-01	7.86262e+01	7.96254e+01
.00900	8.64443e-01	1.58614e+02	1.59479e+02	9.99180e-01	8.03011e+01	8.13003e+01
.00950	8.64443e-01	1.61302e+02	1.62166e+02	9.99180e-01	8.16106e+01	8.26098e+01
.01000	8.64443e-01	1.633379e+02	1.64243e+02	9.99180e-01	8.26203e+01	8.36195e+01
.01050	8.64443e-01	1.64964e+02	1.65828e+02	9.99180e-01	8.33894e+01	8.43886e+01
.01100	8.64443e-01	1.66161e+02	1.67025e+02	9.99180e-01	8.39689e+01	8.49681e+01
.01150	8.64443e-01	1.67056e+02	1.67921e+02	9.99180e-01	8.44016e+01	8.54007e+01
.01200	8.64443e-01	1.67721e+02	1.68586e+02	9.99180e-01	8.47223e+01	8.57215e+01
.01250	8.64443e-01	1.68213e+02	1.69077e+02	9.99180e-01	8.49589e+01	8.59581e+01

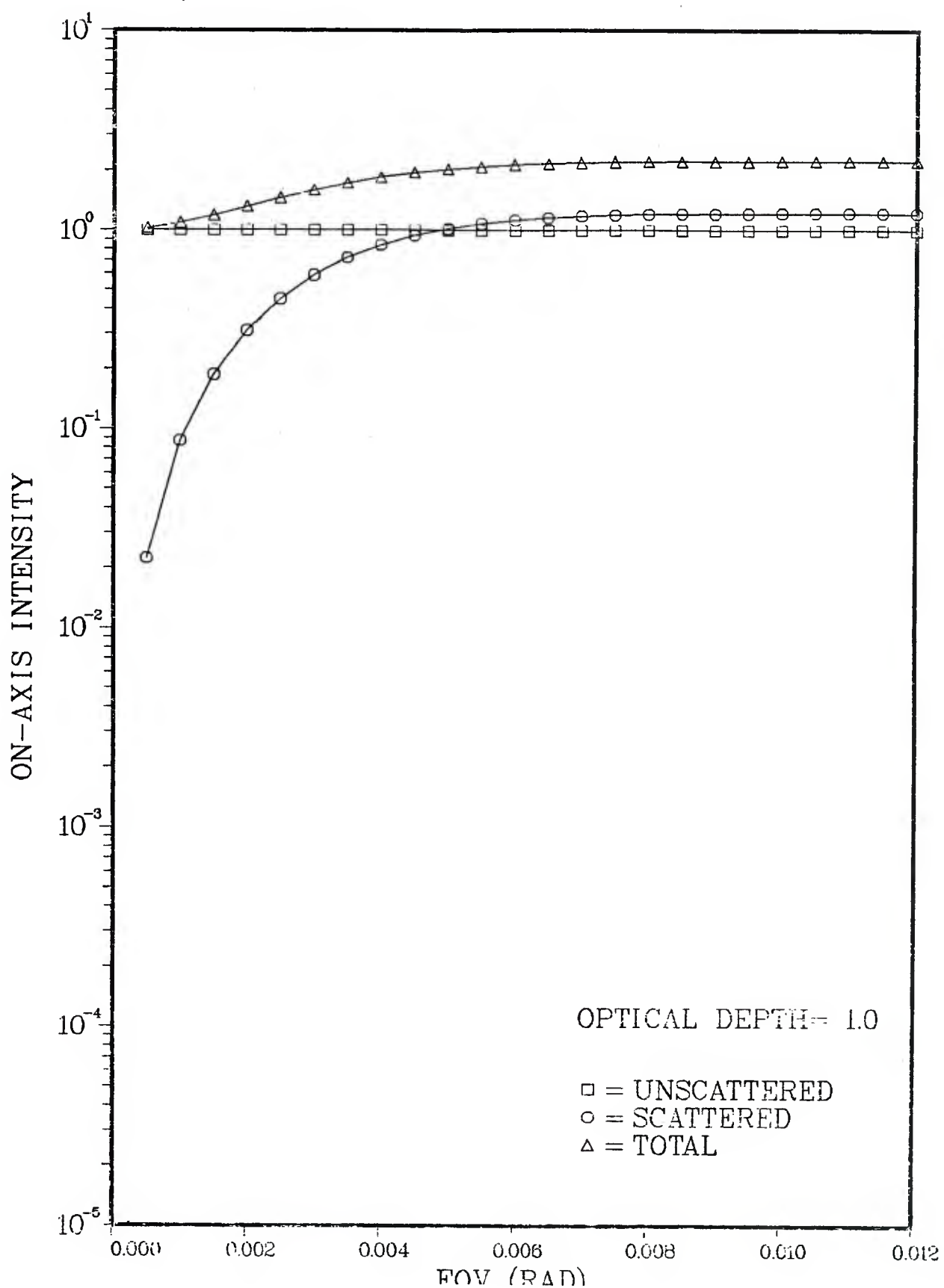


Fig. 19: Normalized intensity on the beam axis as function of detector FOV corresponding to Table 8 for  $\alpha = 289.33 \text{ rad}^{-1}$ ,  $R_D = 1.0 \text{ cm}$ , and  $\tau = 1.0$ .

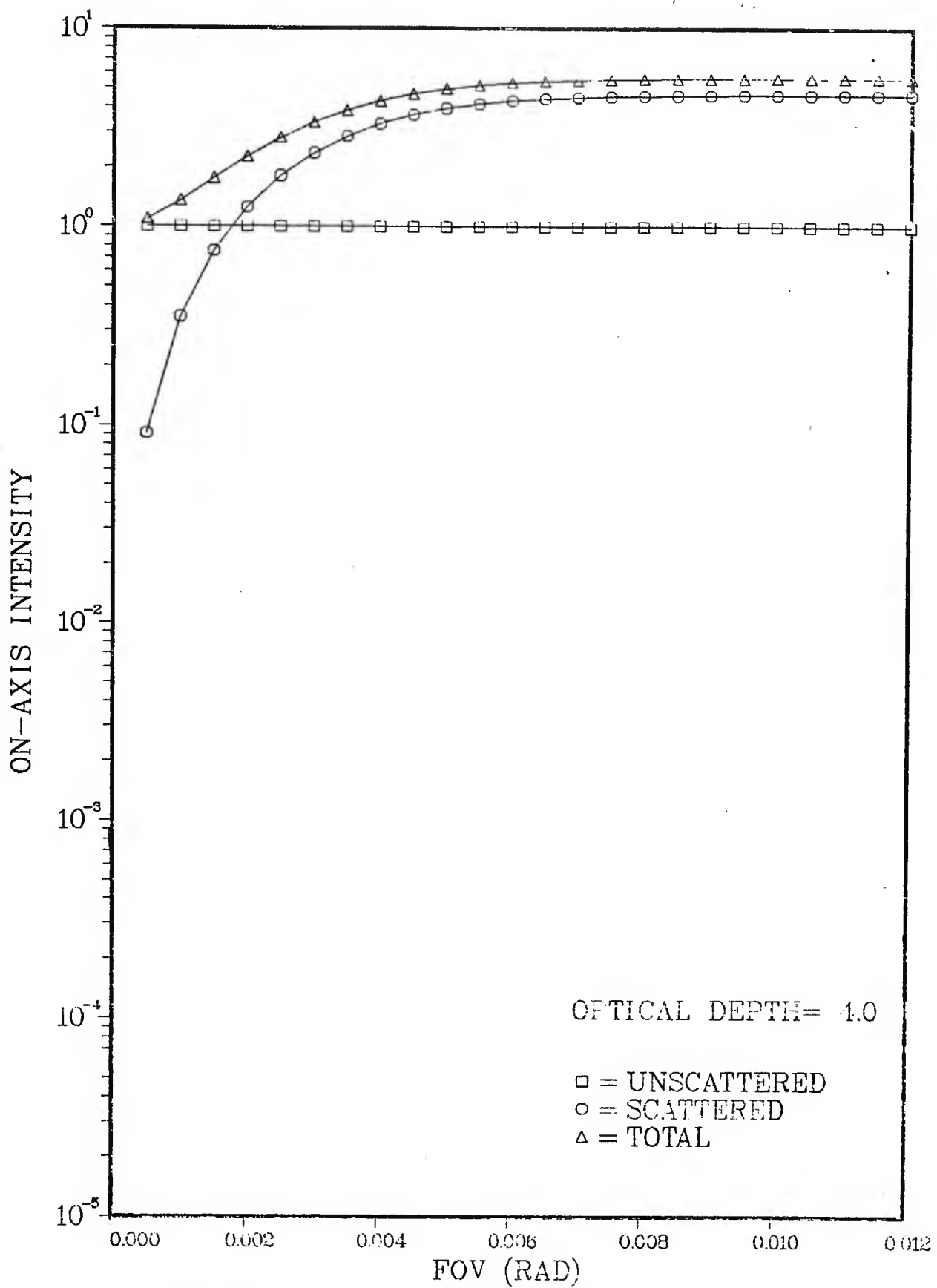


Fig. 20: Normalized intensity on the beam axis as function of detector FOV corresponding to Table 9 for  $\alpha = 289.33 \text{ rad}^{-1}$ ,  $R_D = 1.0 \text{ cm}$ , and  $\tau = 4.0$ .

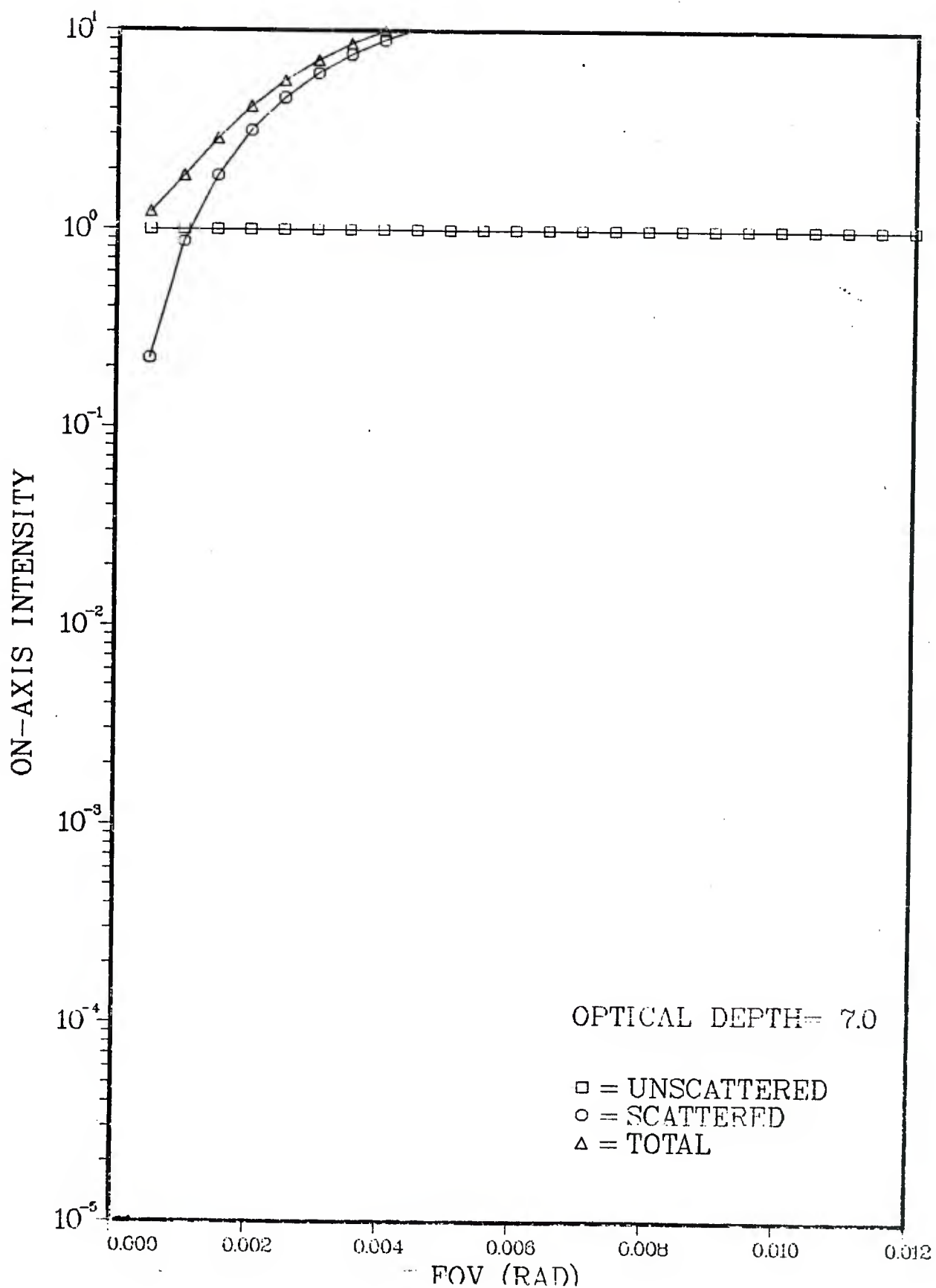


Fig. 21: Normalized intensity on the beam axis as function of detector FOV corresponding to Table 10 for  $\alpha = 289.33 \text{ rad}^{-1}$ ,  $R_D = 1.0 \text{ cm}$ , and  $\tau = 7.0$ .

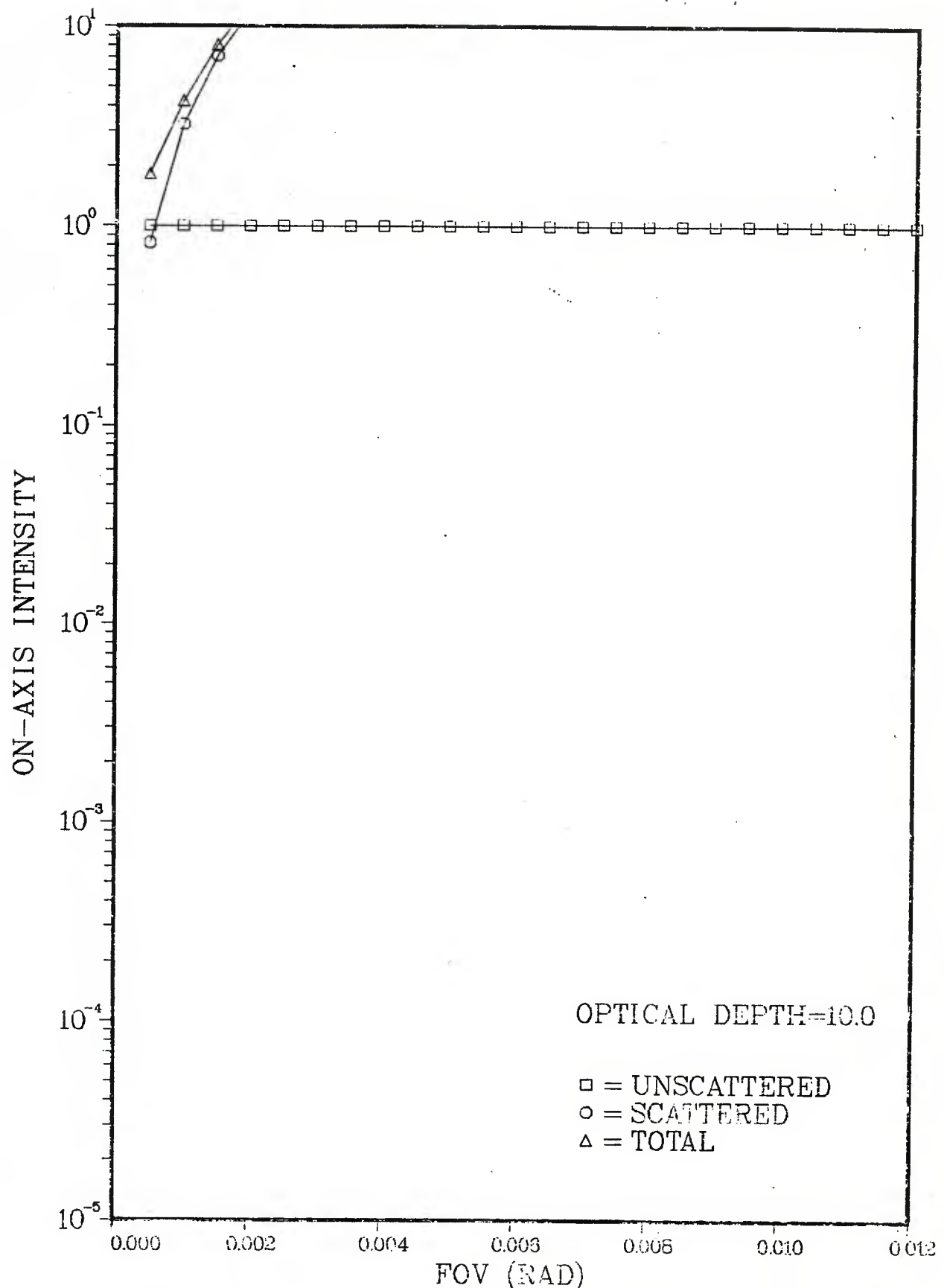


Fig. 22: Normalized intensity on the beam axis as function of detector FOV corresponding to Table 11 for  $\alpha = 289.33 \text{ rad}^{-1}$ ,  $R_D = 1.0 \text{ cm}$ , and  $\tau = 10.0$ .

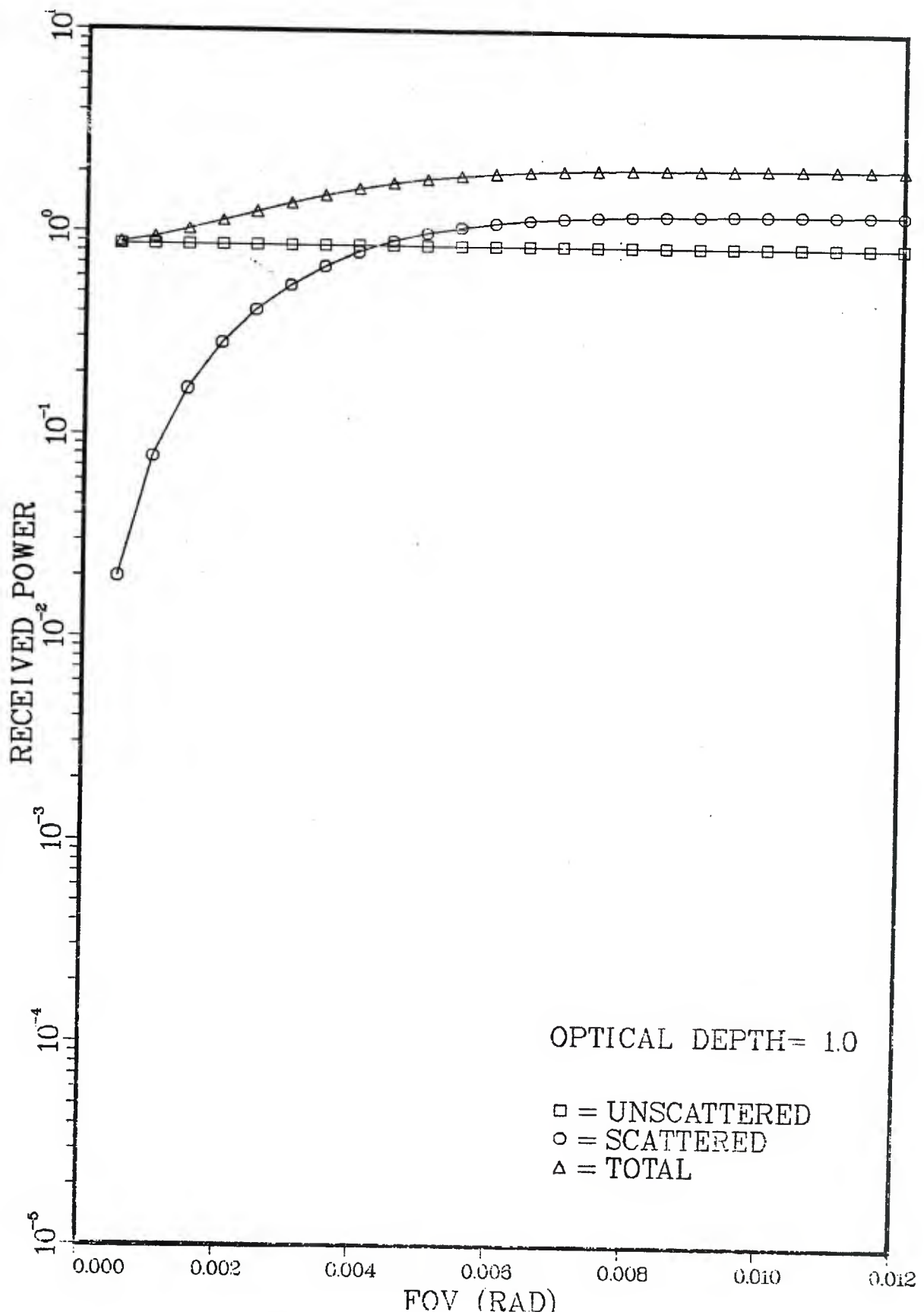


Fig. 23: Received power (arbitrary units) on the beam axis as function of detector FOV corresponding to Table 8 for  $\alpha = 289.33 \text{ rad}^{-1}$ ,  $R_D = 1.0 \text{ cm}$ , and  $\tau = 1.0$ . Received power is multiplied by  $\exp(\tau)$ .

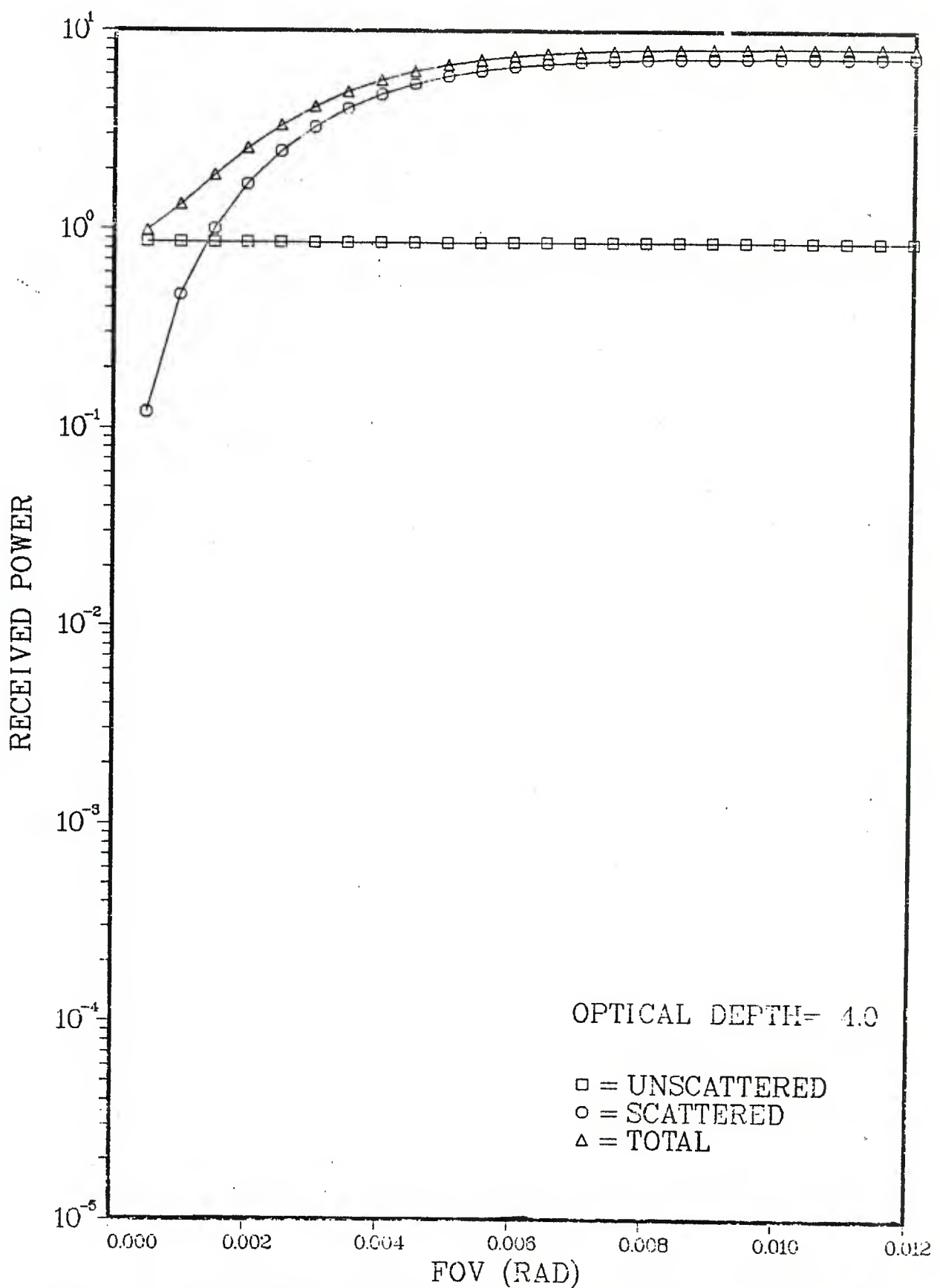


Fig. 24: Received power (arbitrary units) on the beam axis as function of detector FOV corresponding to Table 9 for  $\alpha = 289.33 \text{ rad}^{-1}$ ,  $R_D = 1.0 \text{ cm}$ , and  $\tau = 4.0$ . Received power is multiplied by  $\exp(\tau)$ .

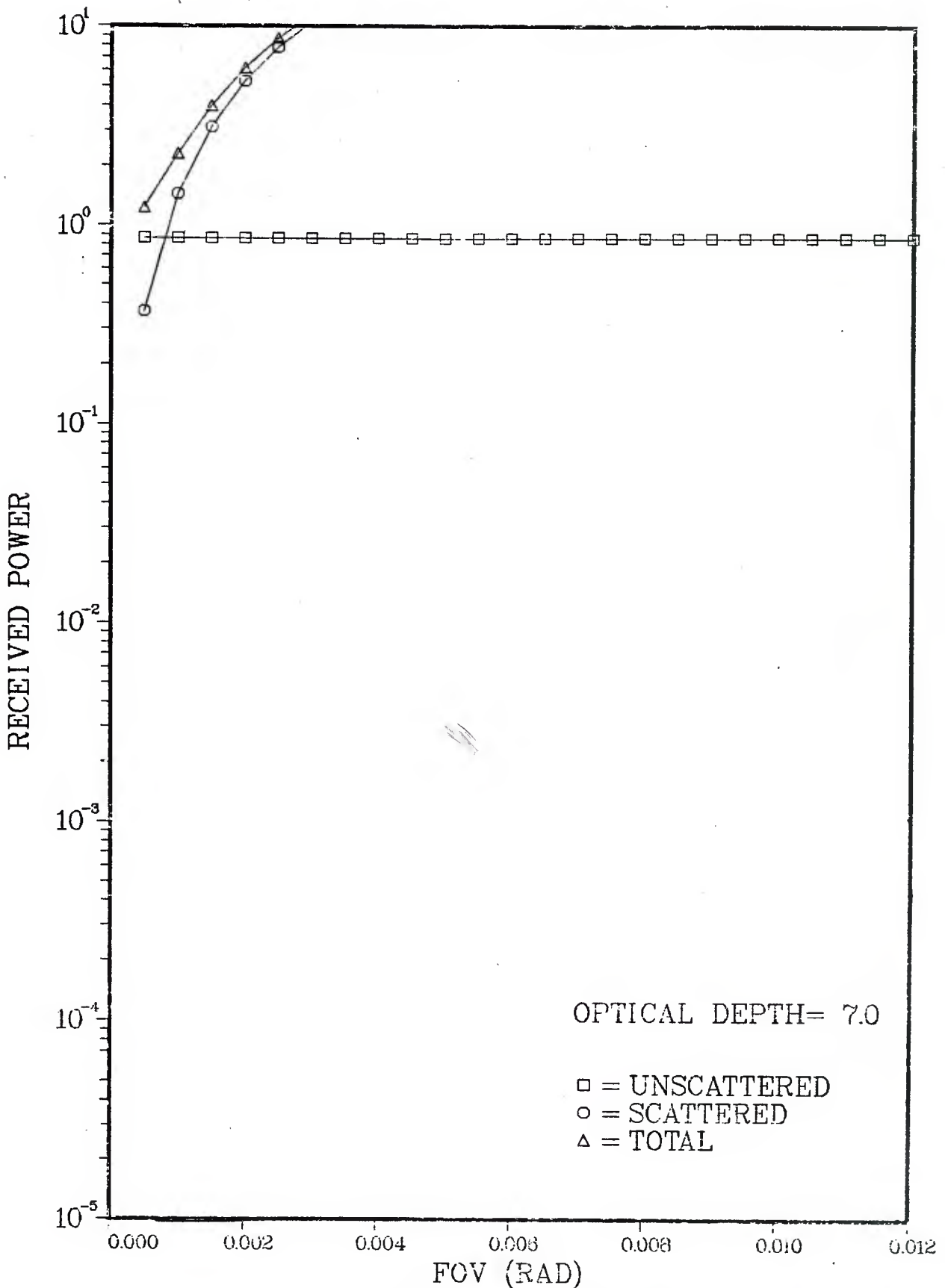


Fig. 25: Received power (arbitrary units) on the beam axis as function of detector FOV corresponding to Table 10 for  $\alpha = 289.33 \text{ rad}^{-1}$ ,  $R_D = 1.0 \text{ cm}$ , and  $\tau = 7.0$ . Received power is multiplied by  $\exp(\tau)$ .

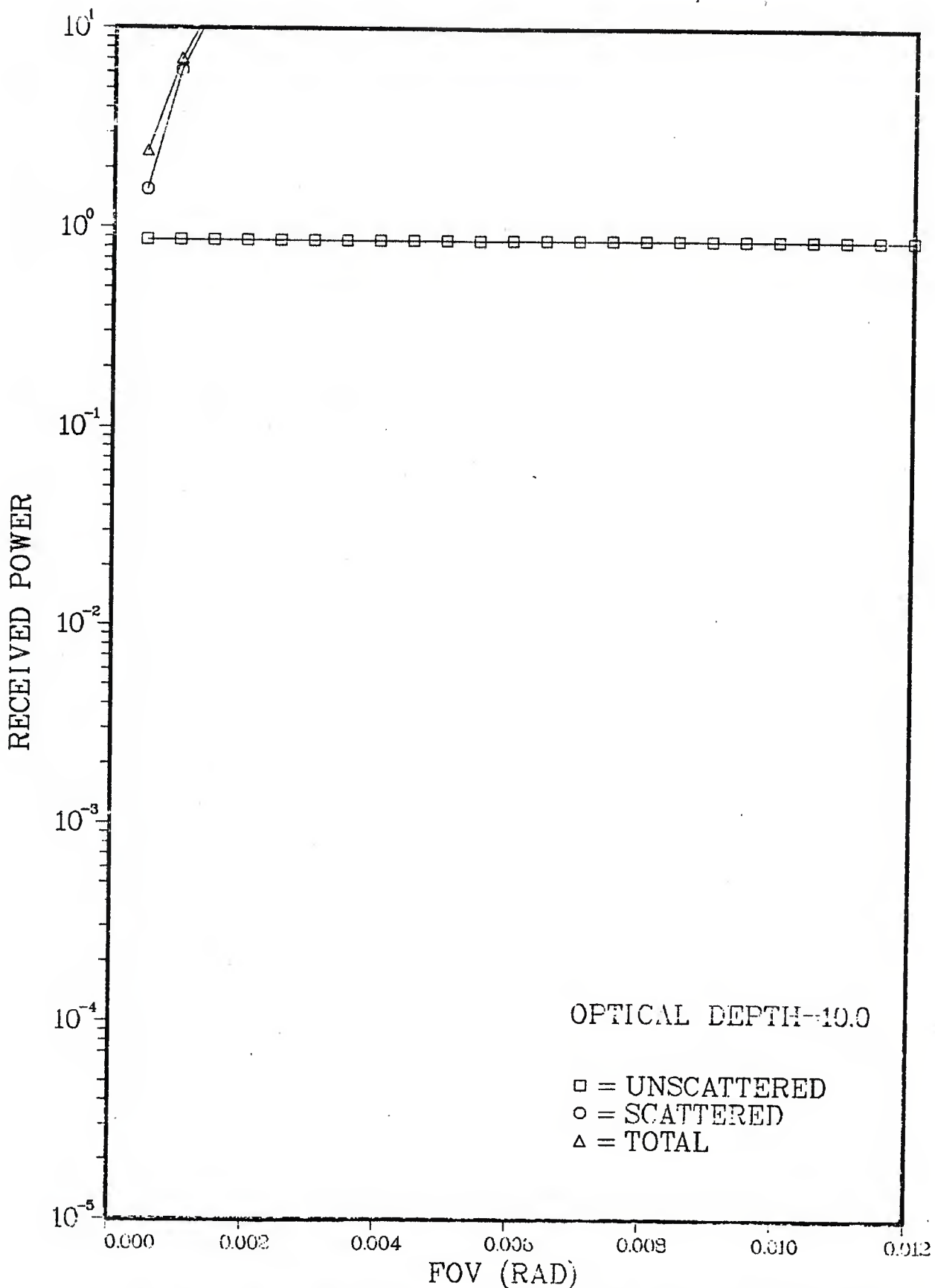


Fig. 26: Received power (arbitrary units) on the beam axis as function of detector FOV corresponding to Table 11 for  $\alpha = 289.33 \text{ rad}^{-1}$ ,  $R_D = 1.0 \text{ cm}$ , and  $\tau = 10.0$ . Received power is multiplied by  $\exp(\tau)$ .

at  $\lambda = 0.45 \mu\text{m}$ , for a coaxial detector of diameter  $R_D = 1 \text{ cm}$ . Note that the phase function and the Gaussian fit to the forward lobe of the Mie phase function are plotted in Fig. 3.

In order to study the effect of the detector's radius  $R_D$ , we let  $R_D$  assume values smaller and larger than the beam diameter of the  $1.0 \text{ cm}$ , viz.,  $R_D = 0.2 \text{ cm}$  and  $2.0 \text{ cm}$ . Results were obtained for same parameters as in Tables 8-11. However, for the sake of clarity we present only the results for  $\tau = 4.0$  for the two cases, viz.,  $R_D = 0.2 \text{ cm}$  (Table 12, Figs. 27-28) and  $R_D = 2.0 \text{ cm}$  (Table 13, Figs. 29-30). Table 12 and Figs. 27-28 depict the corresponding values of intensity and received power as functions of FOV for  $R_D = 0.2 \text{ cm}$ , whereas, Table 13 and Figs. 29-30 depict the corresponding values for  $R_D = 2.0 \text{ cm}$ . The three cases ( $R_D = 1.0, 0.2$  and  $2.0 \text{ cm}$ ;  $\tau = 4.0$ ) for large particles with phase function parameter  $\alpha = 289.33 \text{ cm}^{-1}$  show clearly the contrast in the behavior of the intensity and the received power.

The Fante-Dolin approximation employed in this paper enables one to estimate the corrections to the Bouguer-Beer law for a receiver having a finite field of view, as for example in Ref. 45.

TABLE 12. Received Power and On-Axis Intensity as Functions of the Detector FOV for the

Same Parameters as in Table 8, Except for  $R_D = 0.2$  cm and  $\tau = 4.0$ .

optical depth= 4.00

fov (rad)	pr-unscat.	pr-scatt.	pr-total	i-un	i-sc	i-tot
.00050	7.68740e-02	7.15489e-03	8.40238e-02	9.99869e-01	9.07773e-02	1.09065e+00
.00100	7.68740e-02	2.77738e-02	1.04648e-01	9.99869e-01	3.52279e-01	1.35215e+00
.00150	7.68740e-02	5.94859e-02	1.36360e-01	9.99869e-01	7.54168e-01	1.75404e+00
.00200	7.68740e-02	9.88488e-02	1.75723e-01	9.99869e-01	1.25246e+00	2.25232e+00
.00250	7.68740e-02	1.41969e-01	2.18843e-01	9.99869e-01	1.79750e+00	2.79737e+00
.00300	7.68740e-02	1.85133e-01	2.62007e-01	9.99869e-01	2.34212e+00	3.34199e+00
.00350	7.68740e-02	2.25314e-01	3.02188e-01	9.99869e-01	2.84801e+00	3.84788e+00
.00400	7.68740e-02	2.60454e-01	3.37328e-01	9.99869e-01	3.28938e+00	4.28925e+00
.00450	7.68740e-02	2.89527e-01	3.66401e-01	9.99869e-01	3.65359e+00	4.65346e+00
.00500	7.68740e-02	3.12400e-01	3.89274e-01	9.99869e-01	3.93932e+00	4.93919e+00
.00550	7.68740e-02	3.29589e-01	4.06463e-01	9.99869e-01	4.15341e+00	5.15328e+00
.00600	7.68740e-02	3.41980e-01	4.18854e-01	9.99869e-01	4.30728e+00	5.30715e+00
.00650	7.68740e-02	3.50587e-01	4.27461e-01	9.99869e-01	4.41385e+00	5.41372e+00
.00700	7.68740e-02	3.56378e-01	4.33252e-01	9.99869e-01	4.48535e+00	5.48522e+00
.00750	7.68740e-02	3.60174e-01	4.37048e-01	9.99869e-01	4.53210e+00	5.53197e+00
.00800	7.68740e-02	3.62614e-01	4.39488e-01	9.99869e-01	4.56208e+00	5.56194e+00
.00850	7.68740e-02	3.64162e-01	4.41036e-01	9.99869e-01	4.58106e+00	5.58093e+00
.00900	7.68740e-02	3.65137e-01	4.42011e-01	9.99869e-01	4.59300e+00	5.59287e+00
.00950	7.68740e-02	3.65751e-01	4.42625e-01	9.99869e-01	4.60050e+00	5.60037e+00
.01000	7.68740e-02	3.66137e-01	4.43011e-01	9.99869e-01	4.60522e+00	5.60509e+00
.01050	7.68740e-02	3.66381e-01	4.43255e-01	9.99869e-01	4.60819e+00	5.60806e+00
.01100	7.68740e-02	3.66534e-01	4.43408e-01	9.99869e-01	4.61006e+00	5.60993e+00
.01150	7.68740e-02	3.66631e-01	4.43505e-01	9.99869e-01	4.61123e+00	5.61110e+00
.01200	7.68740e-02	3.66691e-01	4.43565e-01	9.99869e-01	4.61195e+00	5.61182e+00
.01250	7.68740e-02	3.66726e-01	4.43600e-01	9.99869e-01	4.61237e+00	5.61224e+00

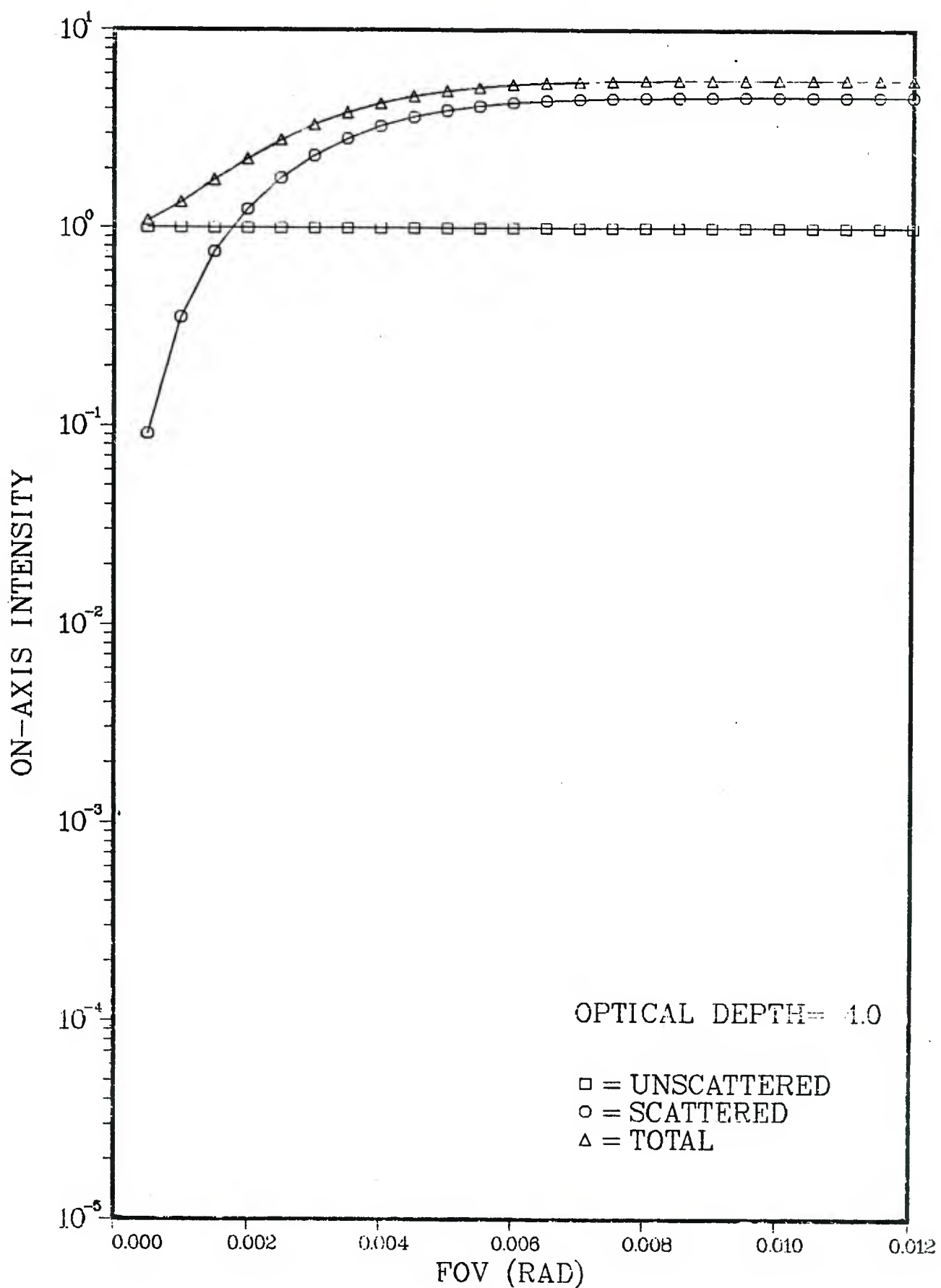


Fig. 27: Normalized intensity on the beam axis as function of detector FOV for the same parameters as in Fig. 20 except  $R_D = 0.2$  cm.

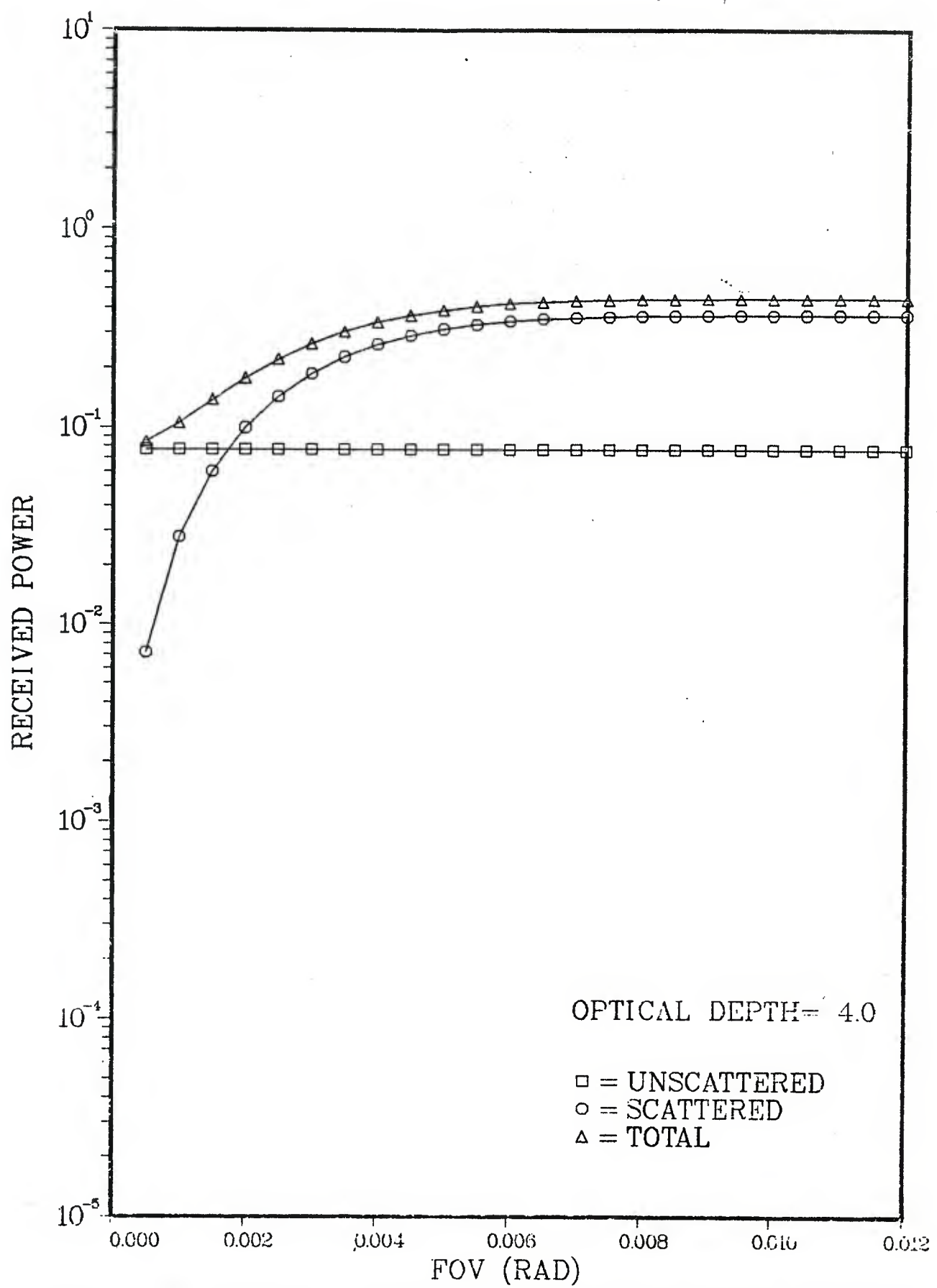


Fig. 28: Received power (arbitrary units) on the beam axis as a function of detector FOV, for the same parameters as in Fig. 27. The received power is multiplied by  $\exp(\tau)$ .

TABLE 13. Received Power and On-Axis Intensity as Functions of the Detector FOV for the Same Parameters as in Table 8, Except for  $R_D = 2.0$  cm and  $\tau = 4.0$ .

optical depth= 4.00		fov (rad)	pr-unscat.	pr-scatt.	pr-total	i-un	i-sc	i-tot
.00050	9.99664e-01	2.37529e+00	1.23719e+00	9.99869e-01	9.07773e-02	1.09065e+00	3.52279e-01	1.35215e+00
.00100	9.99664e-01	9.34312e-01	1.93398e+00	9.99869e-01	3.04422e+00	9.99869e-01	7.54168e-01	1.75404e+00
.00150	9.99664e-01	2.04455e+00	3.04422e+00	9.99869e-01	4.49677e+00	9.99869e-01	1.25246e+00	2.25232e+00
.00200	9.99664e-01	3.49711e+00	6.20220e+00	9.99869e-01	6.49711e+00	9.99869e-01	1.79750e+00	2.79737e+00
.00250	9.99664e-01	5.20254e+00	8.06144e+00	9.99869e-01	8.06144e+00	9.99869e-01	2.34212e+00	3.34199e+00
.00300	9.99664e-01	7.06178e+00	9.97490e+00	9.99869e-01	9.97490e+00	9.99869e-01	2.84801e+00	3.84788e+00
.00350	9.99664e-01	8.97523e+00	1.18510e+01	9.99869e-01	1.18510e+01	9.99869e-01	3.28938e+00	4.28925e+00
.00400	9.99664e-01	1.08613e+01	1.36129e+01	9.99869e-01	1.36129e+01	9.99869e-01	3.65359e+00	4.65346e+00
.00450	9.99664e-01	1.26133e+01	1.42039e+01	9.99869e-01	1.42039e+01	9.99869e-01	3.93932e+00	4.93919e+00
.00500	9.99664e-01	1.44047e+01	1.58711e+01	9.99869e-01	1.58711e+01	9.99869e-01	4.15341e+00	5.15328e+00
.00550	9.99664e-01	1.55875e+01	1.65871e+01	9.99869e-01	1.65871e+01	9.99869e-01	4.30728e+00	5.30715e+00
.00600	9.99664e-01	1.67489e+01	1.774485e+01	9.99869e-01	1.774485e+01	9.99869e-01	4.41385e+00	5.41372e+00
.00650	9.99664e-01	1.76911e+01	1.86908e+01	9.99869e-01	1.86908e+01	9.99869e-01	4.51350e+00	5.51346e+00
.00700	9.99664e-01	1.84310e+01	1.94307e+01	9.99869e-01	1.94307e+01	9.99869e-01	4.61328e+00	5.61324e+00
.00750	9.99664e-01	1.89942e+01	1.99938e+01	9.99869e-01	1.99938e+01	9.99869e-01	4.71325e+00	5.71322e+00
.00800	9.99664e-01	1.94106e+01	2.04102e+01	9.99869e-01	2.04102e+01	9.99869e-01	4.81322e+00	5.81319e+00
.00850	9.99664e-01	1.97105e+01	2.07101e+01	9.99869e-01	2.07101e+01	9.99869e-01	4.91320e+00	5.91317e+00
.00900	9.99664e-01	1.99216e+01	2.09213e+01	9.99869e-01	2.09213e+01	9.99869e-01	5.01318e+00	6.01316e+00
.00950	9.99664e-01	2.00676e+01	2.10672e+01	9.99869e-01	2.10672e+01	9.99869e-01	5.11316e+00	6.11314e+00
.01000	9.99664e-01	2.01672e+01	2.11669e+01	9.99869e-01	2.11669e+01	9.99869e-01	5.21315e+00	6.21313e+00
.01050	9.99664e-01	2.02348e+01	2.12345e+01	9.99869e-01	2.12345e+01	9.99869e-01	5.31313e+00	6.31311e+00
.01100	9.99664e-01	2.02805e+01	2.12802e+01	9.99869e-01	2.12802e+01	9.99869e-01	5.41311e+00	6.41309e+00
.01150	9.99664e-01	2.03115e+01	2.13111e+01	9.99869e-01	2.13111e+01	9.99869e-01	5.51123e+00	6.51121e+00
.01200	9.99664e-01	2.03325e+01	2.13322e+01	9.99869e-01	2.13322e+01	9.99869e-01	5.61195e+00	6.61193e+00
.01250	9.99664e-01	2.03468e+01	2.13465e+01	9.99869e-01	2.13465e+01	9.99869e-01	5.61224e+00	6.61223e+00

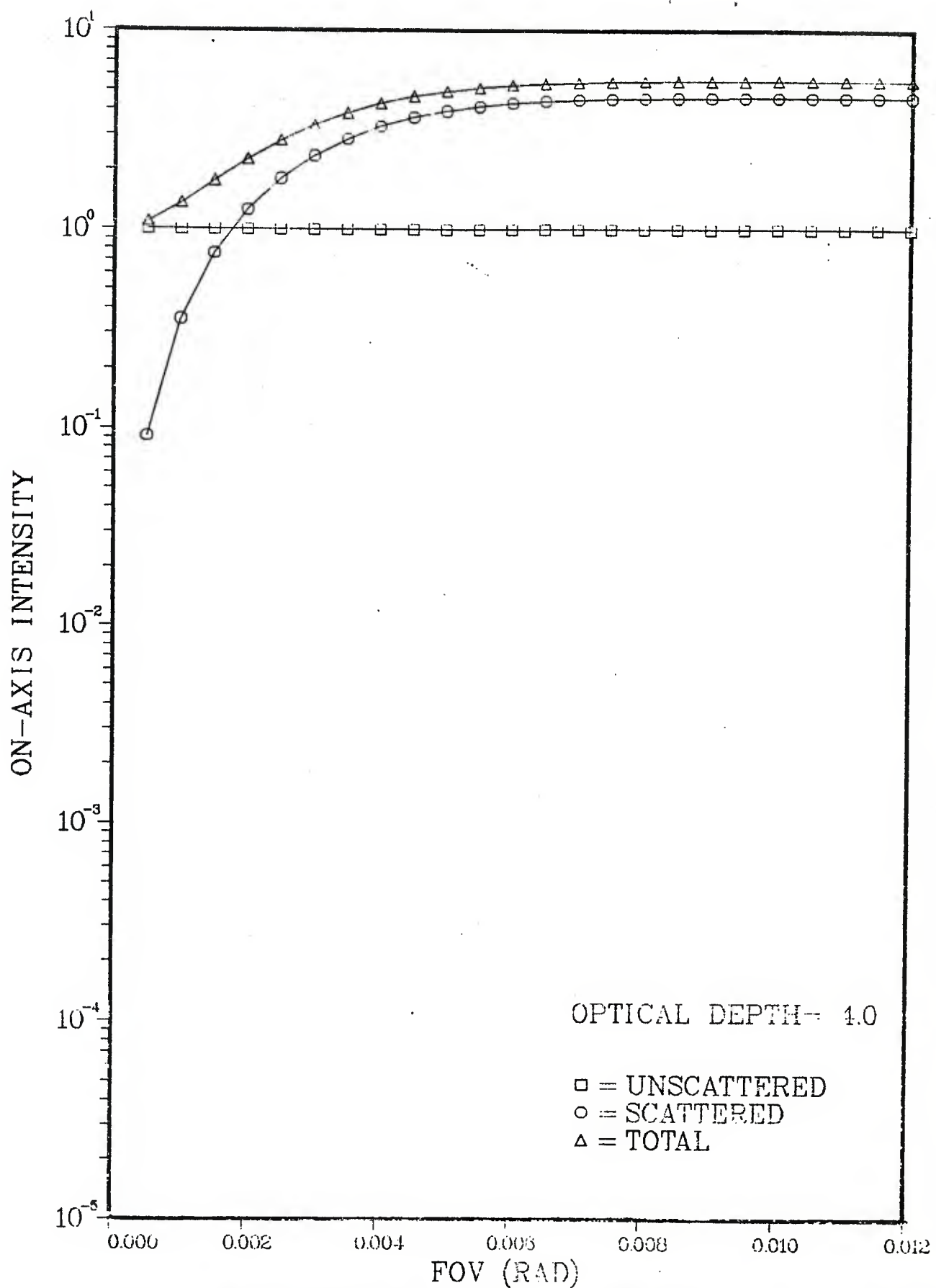


Fig. 29: Normalized intensity on the beam axis as a function of detector FOV for the same parameters as in Fig. 20, except  $R_D = 2.0$  cm.

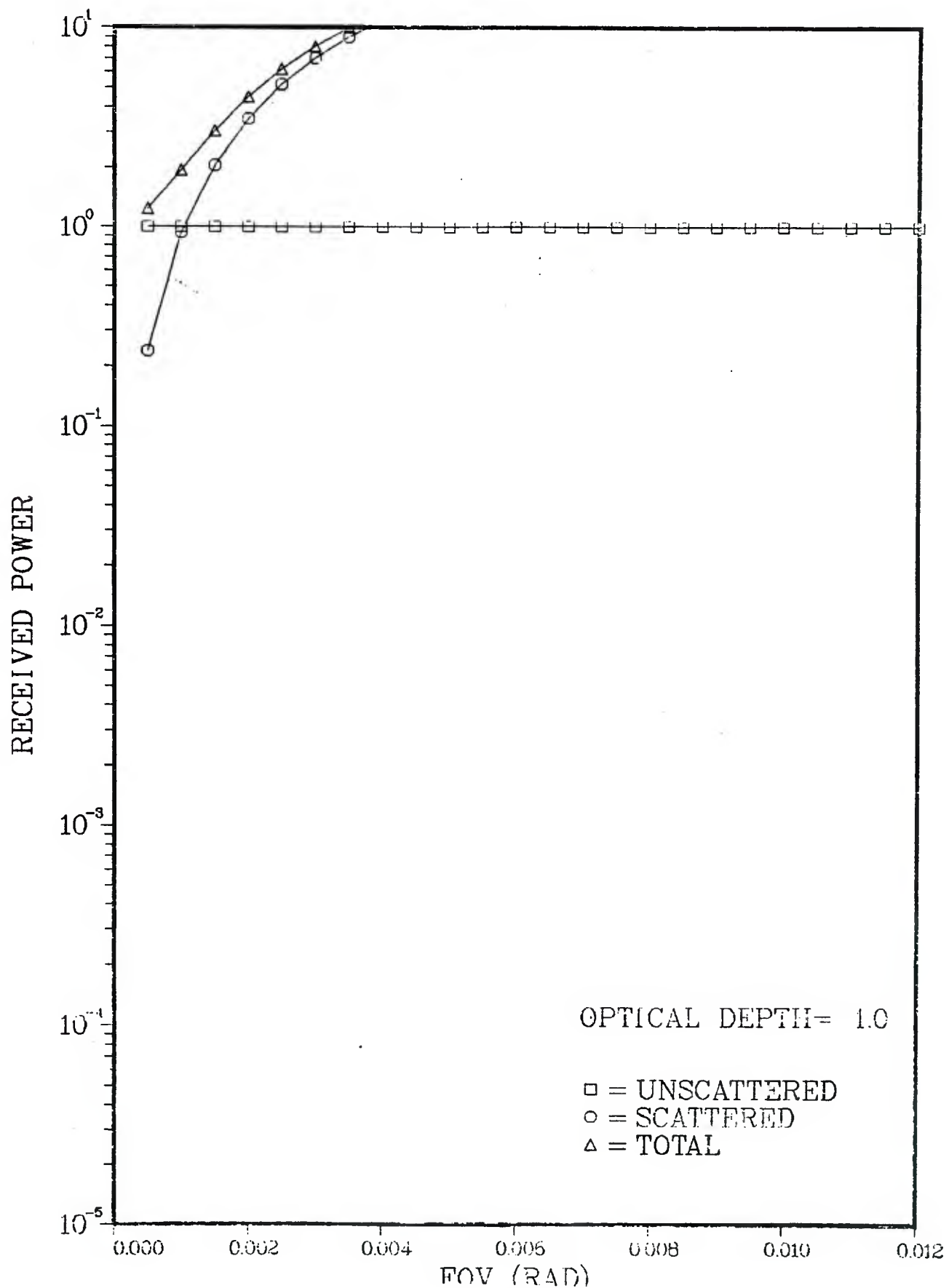


Fig. 30: Received power (arbitrary units) on the beam axis as a function of detector FOV, for the same parameters as in Fig. 29. The received power is multiplied by  $\exp(\tau)$ .

#### 4. CONCLUDING REMARKS

In this report, we have discussed some new formulations, computational methods, and results for the complex subject of multiple scattering effects on laser beams traversing dense aerosols, particularly in connection with topics such as higher order scattering contributions, exact solutions of the radiative transfer equation in the small angle approximation, and scattered radiance as a function of detector field-of-view. Conclusions based on work done thus far and recommendations for future research are given as follows.

1. In this paper, we developed the formulations for solving the radiative transfer equation (RTE) for laser beams traversing scattering media in the small-angle approximation and for making the results tractable to numerical computations by three different approaches:
  - a. Tam and Zardecki exact approach
  - b. Box and Deepak exact approach
  - c. Fante-Dolin approximation approach

The formulations for the quantities of interest, namely, the beam intensity, irradiance and the detected power are given. Numerical computations for the scattered irradiance and detected power were performed using the first two approaches. Tam and Zandecki approach, though computationally more time consuming than the Box and Deepak approach, gives additional insight into the contributions made by higher orders of scattering to the total multiple scattering; the latter just gives the total MS value. To date, the Tam and Zardecki approach has not been used to solve the case of non-Gaussian

phase functions; whereas the Box and Deepak approach can handle non-Gaussian phase functions. It is recommended that further work be performed to solve for the radiance and irradiance of laser beams for non-Gaussian phase functions by these two approaches.

2. It should be noted that the small-angle approximation is valid for highly forward-peaked phase functions. It is, therefore, recommended that approaches be developed to deal with the case of MS in laser beams traversing small size aerosol particles, with broadly-peaked phase functions.

3. It is recommended that experiments and numerical computations be performed to determine the effects of the detector field of view on the extinction and backscattering function measurements.

4. It is recommended that measurements and theoretical computations be performed to investigate the effects of beam diameter on optical extinction measurements.

5. It is recommended that the above investigation be repeated for the case of backscattering, which is of great importance for single-ended electro-optical systems such as Lidar, DIAL and Laser Doppler Velocimeter (LDV).

## 5. REFERENCES

1. H. C. van de Hulst, *Light Scattering by Small Particles*, John Wiley and Sons, Inc., New York (1957).
2. D. H. Woodward, J. O. S. A. 54, 1325 (1964).
3. C. Smart, et al. J. O. S. A. 55, 947 (1965).
4. R. Walsh, Appl. Opt. 7, 1213 (1968).
5. A. Deepak and A. E. S. Green, Appl. Opt. 9, 2362 (1970).
6. A. Deepak, *Second and Higher Order Scattering of Light in a Settling Polydisperse Aerosol*, Ph.D. Dissertation, University of Florida, 1969, Univeristy Microfilms, Ann Arbor, Michigan.
7. M. Kerker, *The Scattering of Light and other Electromagnetic Radiation*, Academic Press, Inc., New York (1969).
8. V. E. Zuev, M. V. Kabanov and B. A. Savelev, Izv. Atm. and Oceanic Phys. 13, 724-732 (1967).
9. E. A. Bucher and R. M. Lerner, Appl. Opt. 12, 2401 (1973).
10. W. H. Paik, M. Tebyani, D. J. Epstein, R. S. Kennedy, and J. H. Shapiro, Appl. Opt. 17, 899 (1978).
11. J. S. Ryan and A. I. Carswell, J. Opt. Soc. Am. 68, 900 (1978).
12. J. S. Ryan, S. R. Pal, and A. I. Carswell, J. Opt. Soc. Am. 69, 60 (1979).
13. G. C. Mooradian, M. Geller, L. B. Stotts, D. H. Stephens, and R. A. Krautwald, Appl. Opt. 18, 429 (1979).
14. G. C. Mooradian, M. Geller, P. H. Levine, L. B. Stotts, and D. H. Stephens, Appl. Opt. 19, 11 (1980).
15. V. A. Donchenko, I. V. Samokhvalov and G. G. Matviyenko, Atmos. and Oceanic Phys. 7, 776-779 (1971).
16. E. A. Bucher, Appl. Opt. 12, 2391 (1973).

17. C. Beck, Opt. Laser Technol. 9, 81 (1977).
18. D. Arnush, J. Opt. Soc. Am. 62, 1109 (1972).
19. S. T. Hong and A. Ishimaru, Radio Sci. 11, 551 (1976).
20. R. L. Fante, IEEE Antennas Propag. AP-21 (5), 750 (1973).
21. H. C. van de Hulst, A New Look at Multiple Scattering, NASA/Goddard Inst. for Space Studies Report, 1963.
22. W. G. Tam and A. Zardecki, J. Opt. Soc. Am. 69, 68-70 (1979).
23. W. G. Tam and A. Zardecki, Optica Acta 26, 659-670 (1979).
24. A. Zardecki and W. G. Tam, Can. J. Phys. 57, 1301 (1979).
25. G. N. Plass and G. W. Kattawar, Appl. Opt. 7, 415 (1969).
26. A. N. Witt, Astrophys J. Suppl. Ser. 35, 1 (1977).
27. A. Ishimaru, Proc. IEEE 65, 1030 (1977).
28. L. B. Stotts, J. Opt. Soc. Am. 69, 1719 (1979).
29. H. S. Snyder and W. T. Scott, Phys. Rev. 76, 220 (1949).
30. W. S. Scott, Rev. Mod. Phys. 35, 321 (1963).
31. H. M. Heggestad, Optical Communication Through Multiple Scattering Media, M.I.T. Technical Report No. 472, 22 November (1968).
32. S. R. Pal and A. I. Carswell, Appl. Opt. 15, 415-419 (1976).
33. J. L. Soret, Annls. Chim. et Phys. 14, 503 (1888).
34. S. Chandrashekhar, Radiative Transfer, Dover, New York (1960).
35. Z. Sekera, Handbuch der Physik, Ed. S. Flugge, Springer Verlag, Berlin, 48, 288 (1957).
36. G. N. Plass and G. W. Kattawar, Appl. Opt. 7, 361 (1968).
37. K. Cunningham, M. B. Wells, and D. G. Collins, Light Transport in the Atmosphere, Vol. II: Machine Codes for Calculation of Aerosol Scattering and Absorption Coefficients, Radiation Research Associates, Inc., Fort Worth, Texas (1966).

38. W. Hartel, *Das Licht*, 10, 141 (1941).
39. J. Dell Imagine, *A Study of MS of Optical Radiation with Applications to Laser Communication*, Ph.D. Dissertation, U.C.L.A., Los Angeles (1964).
40. C. Whitney, *J. Quant. Spectrosc. Radiat. Transfer*, 14, 591-611 (1974).
41. J. Lenoble (Ed.), *Standard Procedures to Compute Atmospheric Radiative Transfer in a Scattering Atmosphere*, Vol. I, IAMAP Radiation Commission, (1975).
42. A. Ishimaru and S. T. Hong, *Radio Science* 10, No. 6, 637 (1975).
43. J. A. Weinman, *J. Atmos. Sci.* 33, 1763 (1976).
44. L. B. Stotts, *J. Opt. Soc. Am.* 67, 815-819 (1977).
45. C. K. Whitney, *J. Opt. Soc. Am.* 69, 1554 (1979).
46. M. A. Box and A. Deepak, *Small-Angle Approximation to the Transfer of Narrow Laser Beams in Anisotropic Scattering Media*, NASA-CR, 1980.
47. M. A. Box and A. Deepak, *J. Opt. Soc. Am.*, 71, 1534 (1981).
48. A. Deepak, A. Zardecki, U. O. Farrukh and M. A. Box, *Multiple Scattering Effects of Laser Beams Traversing Dense Aerosol Media*, A. Deepak (ed.) *Atmospheric Aerosols: Their Formation, Properties and Effects*, Spectrum Press, Hampton, Virginia, 1982.
49. R. E. Danielson, D. R. Moore and H. C. van de Hulst, *J. Atmos. Sci.*, 26, 1078-1087 (1968).
50. K. E. Kunkel and J. A. Weinman, *J. Atmos. Sci.* 33, 1772-1781 (1976).
51. G. N. Plass and G. W. Kattawar, *Appl. Opt.* 7, 415-419 (1968); *Ibid*, 699-704; *Ibid*, 1519-1527.
52. G. W. Kattawar and G. N. Plass, *Appl. Opt.* 7, 869-878 (1968); *Appl. Opt.* 10, 738-748 (1971).
53. K. Liou and R. M. Schotland, *J. Atmos. Sci.* 28, 772 (1971).
54. R. C. Anderson and E. V. Browell, *Appl. Opt.* 11, 1345 (1972).
55. E. W. Eloranta, *Calculation of Doubly Scattered Lidar Returns*, Ph.D. Thesis, U. Wisconsin, Madison, 115 pp. (available from University Microfilms International, 300 North Zeeb Road, Ann Arbor, MI 48106).

56. E. W. Eloranta and S. T. Shipley, A Solution for Multiple Scattering, A. Deepak (ed.) *Atmospheric Aerosols: Their Formation, Properties and Effects*, Spectrum Press, Hampton, Virginia, 1982.
57. R. P. Hemenger, J. Opt. Soc. Am. 64, 503 (1974).
58. A. Deepak and A. H. Fluellen, A Comparative Study of Conroy and Monte Carlo Methods Applied to Multiple Quadratures and Multiple Scattering, NASA Contractor Report 3059 (NTIS, Springfield, VA, 1978).
59. G. K. Goedecke, in EOSAEL 80, Vol. I, Technical Documentation, (L. D. Duncan, ed.), Atmospheric Sciences Laboratory Report ASL-TR-0072, January 1981.
60. R. E. Jensen, J. Opt. Soc. Am. 70, 1557 (1980).
61. A. Deepak, U. O. Farrukh, and A. Zardecki, Appl. Opt. 21, 431 (1982).
62. A. Ishimaru, *Wave Propagation and Scattering in Random Media*, Academic Press, New York (1978).
63. L. S. Dolin, Izv. VUZ. Radiofizika 7, 380-382 (1964).
64. L. S. Dolin, Izv. VUZ Radiofizika 9, 61-71 (1966).
65. R. L. Fante, J. Opt. Soc. Am. 64, 592 (1974).
66. R. L. Fante, Proc. IEEE 62, 1400 (1974).
67. R. L. Fante, Proc. IEEE A & P 21, 750-755 (1973).
68. R. L. Fante, J. Opt. Soc. Am. 64, 592 (1974).
69. R. L. Fante, Proc. IEEE 68, 1424 (1980).
70. L. B. Stotts, J. Opt. Soc. Am. 69, 1719-1722 (1979).
71. G. Wentzel, Ann. Phys. 69, 335-345 (1922).
72. H. S. Snyder and W. T. Scott, Phys. Rev. 76, 220-225 (1949).
73. W. T. Scott, Rev. Mod. Phys. 35, 231-313 (1963).
74. D. M. Bravo-Zhivotovskiy, L. S. Dolin, A. G. Luchinin and V. A. Savel'yev, Izv. Atmos. Oceanic Phys. 5, 160-167 (1969).
75. W. G. Tam and A. Zardecki, Appl. Opt. 21, 2405 (1982).

76. D. Deirmendjian, Electromagnetic Scattering on Spherical Polydispersins (NY, 1969).
77. A. Deepak and G. P. Box, Analytic Modeling of Aerosol Size Distributions, NASA Contractor Report 159170 (NTIS, Springfield, VA, 1979).
78. M. Abramowitz and I. A. Stegun, Handbook of Mathematical Functions (Dover, New York, 1965).
79. H. Conroy, J. Chem. Phys. 47, 5307 (1967).
80. R. O. Gumprecht and C. M. Sliepcevich, J. Phys. Chem. 57, 90 (1953).
81. R. O. Gumprecht and C. M. Sliepcevich, J. Phys. Chem. 57, 95 (1953).
82. A. Deepak and O. H. Vaughan, Appl. Opt. 17, 347 (1978).
83. A. Deepak and M. A. Box, Appl. Opt. 17, 2900 (1978).
84. A. Deepak and M. A. Box, Appl. Opt. 17, 3168 (1978).

DISTRIBUTION LIST FOR ARCSL-CR-82060

Names	Copies	Names	Copies
CHEMICAL SYSTEMS LABORATORY			
ATTN: DRDAR-CLB	1	Advanced Research Projects Agency	1
ATTN: DRDAR-CLB-C	1	1400 Wilson Boulevard	
ATTN: DRDAR-CLB-P	1	Arlington, VA 22209	
ATTN: DRDAR-CLB-PS	4	DEPARTMENT OF THE ARMY	
ATTN: DRDAR-CLB-R	1		
ATTN: DRDAR-CLB-T	1	HQDA	
ATTN: DRDAR-CLB-TE	1	ATTN: DAMO-NCC	1
ATTN: DRDAR-CLC-B	1	ATTN: DAMO-NC/COL Robinson (P)	1
ATTN: DRDAR-CLC-C	1	WASH DC 20310	
ATTN: DRDAR-CLF	1		
ATTN: DRDAR-CLJ-R	2	HQDA	
ATTN: DRDAR-CLJ-L	2	Office of the Deputy Chief of Staff for	
ATTN: DRDAR-CLJ-M	1	Research, Development & Acquisition	
ATTN: DRDAR-CLN	1	ATTN: DAMA-CSS-C	1
ATTN: DRDAR-CLN-S	1	Washington, DC 20310	
ATTN: DRDAR-CLN-ST	1		
ATTN: DRDAR-CLT	1	HQ Sixth US Army	
ATTN: DRDAR-CLY-A (Pennsyle, Hundley)	2	ATTN: AFKC-OP-NBC	1
ATTN: DRDAR-CLY-R	1	Presidio of San Francisco, CA 94129	
COPIES FOR AUTHOR(S)			
Research Division	25	Commander	
RECORD COPY: DRDAR-CLB-A	1	DARCOM, STITEUR	
DEPARTMENT OF DEFENSE			
Defense Technical Information Center		ATTN: DRXST-STI	
ATTN: DTIC-DDA-2	2	Box 48, APO New York 09710	1
Cameron Station, Building 5			
Alexandria, VA 22314			
Director		Commander	
Defense Intelligence Agency		USASTCFEO	
ATTN: DB-4G1	1	ATTN: MAJ Mikeworth	1
Washington, DC 20301		APO San Francisco 96328	
Deputy Under Secretary of Defense for		Army Research Office	
Research and Engineering (R&AT)		ATTN: DRXRO-CB (Dr. R. Ghirardelli)	1
ATTN: Dr. Musa	1	ATTN: DRXRO-GS	1
ATTN: COL Friday	1	ATTN: Dr. W. A. Flood	1
ATTN: COL Winter	1	P.O. Box 12211	
Washington, DC 20301		Research Triangle Park, NC 27709	
Defense Advanced Research Projects Agency		HQDA ODUSA (OR)	
ATTN: Dr. Tegnella	1	ATTN: Dr. H. Fallin	1
Washington, DC 20301		Washington, DC 20310	
		HQDA (DAMO-RQD)	
		ATTN: MAJ C. Collat	1
		Washington, DC 20310	

HQDA, OCE ATTN: DAEN-RDM (Dr. Gomez) Massachusetts Ave, NW Washington, DC 20314	1	Director DARCOM Field Safety Activity ATTN: DRXOS-SE (Mr. Yutmeyer) Charlestown, IN 47111	1
OFFICE OF THE SURGEON GENERAL			
Commander US Army Medical Research and Development Command ATTN: SGRD-UBG (Mr. Eaton) ATTN: SGRD-UBG-OT (CPT Johnson) ATTN: LTC Don Gensler Fort Detrick, MD 21701	1	PM Smoke/Obscurants ATTN: DRCPM-SMK-E (A. Van de Wal) ATTN: DRCPM-SMK-M ATTN: DRCPM-SMK-T Aberdeen Proving Ground, MD 21005	1
Commander US Army Medical Bioengineering Research and Development Laboratory ATTN: SGRD-UBD-AL, Bldg 568 Fort Detrick, Frederick, MD 21701	1	Director US Army Materiel Systems Analysis Activity ATTN: DRXSY-MP ATTN: DRXSY-CA (Mr. Metz) ATTN: DRXSY-FJ (J. O'Bryon) ATTN: DRXSY-GP (Mr. Fred Campbell) Aberdeen Proving Ground, MD 21005	1
Commander USA Medical Research Institute of Chemical Defense ATTN: SGRD-UV-L Aberdeen Proving Ground, MD 21010	1	USA AVIATION RESEARCH AND DEVELOPMENT COMMAND	
US ARMY MATERIEL DEVELOPMENT AND READINESS COMMAND		Director Applied Technology Lab USARTL (AVRADCOM) ATTN: DAVDL-ATL-ASV ATTN: DAVDL-ATL-ASW ATTN: DAVDL-EV-MOS (Mr. Gilbert) Ft. Eustis, VA 23604	1
Commander US Army Materiel Development and Readiness Command ATTN: DRCDE-DM ATTN: DRCLDC ATTN: DRCMT ATTN: DRCSF-P ATTN: DRCSF-S ATTN: DRCDL (Mr. N. Klein) ATTN: DRCBI (COL Gearin) ATTN: DRCBSI-EE (Mr. Giambalvo) ATTN: DRCDMD-ST (Mr. T. Shirata) 5001 Eisenhower Ave Alexandria, VA 22333	1	Commander USA Avionics R&D Activity ATTN: DAVAA-E (M. E. Sonntag) Ft. Monmouth, NJ 07703	1
Commander US Army Foreign Science & Technology Center ATTN: DRXST-MT3 ATTN: DRXST-M73 (Poleski) 220 Seventh St., NE Charlottesville, VA 22901	1	USA MISSILE COMMAND	
	1	Commander US Army Missile Command Director, Energy Directorate ATTN: DRSMI-RHFT ATTN: DRSMI-RMST ATTN: DRSMI-YLA (N. C. Katos) Redstone Arsenal, AL 35809	1
	1	Commander US Army Missile Command Redstone Scientific Information Center ATTN: DRSHI-REO (Mr. Widenhofer) ATTN: DRSMI-RGT (Mr. Matt Maddix) ATTN: DRDMI-CGA (Dr. B. Fowler) ATTN: DRDMI-KL (Dr. W. Wharton) ATTN: DRDMI-TE (Mr. H. Anderson) Redstone Arsenal, AL 35809	1

<b>Commander</b>	<b>Director</b>
US Army Missile Command	US Army Atmospheric Sciences Laboratory
Redstone Scientific Information Center	ATTN: DELAS-AS (Dr. Charles Bruce) 1
ATTN: DRSMI-RPR (Documents)	ATTN: DELAS-AS-P (Mr. Tom Pries) 1
Redstone Arsenal, AL 35809	ATTN: DELAS-EO-EN (Dr. Donald Snider) 1
USA COMMUNICATIONS-ELECTRONICS COMMAND	ATTN: DELAS-EO-EN (Mr. James Gillespie) 1
<b>Commander</b>	ATTN: DELAS-EO-ME (Dr. Frank Niles) 1
USA Communications-Electronics Command	ATTN: DELAS-EO-ME (Dr. Ronald Pinnick) 1
ATTN: DRSEL-WL-S (Mr. J. Charlton)	ATTN: DELAS-EO-MO (Dr. Melvin Heaps) 1
Ft. Monmouth, NJ 07703	ATTN: DELAS-EO-MO (Dr. R. Sutherland) 1
USA ELECTRONICS RESEARCH AND	ATTN: DELAS-EO-S (Dr. Louis Duncan) 1
DEVELOPMENT COMMAND	White Sands Missile Range, NM 88002
<b>Commander</b>	US ARMY ARMAMENT RESEARCH AND
USA Electronics Research and	DEVELOPMENT COMMAND
Development Command	<b>Commander</b>
ATTN: DRDEL-CCM (Dr. J. Scales)	US Army Armament Research and
ATTN: DELHD-RT-CB (Dr. Sztankay)	Development Command
2800 Powder Mill Road	ATTN: DRDAR-LCA-L 1
Adelphi, MD 20783	ATTN: DRDAR-LCE-C 1
<b>Commander</b>	ATTN: DRDAR-LCU-CE 1
Harry Diamond Laboratories	ATTN: DRDAR-NC (COL Fields) 3
ATTN: DRXDO-RCB (Dr. Donald Wortman)	ATTN: DRDAR-SCA-T 1
ATTN: DRXDO-RCB (Dr. Clyde Morrison)	ATTN: DRDAR-SCF 1
ATTN: DRXDO-RDC (Mr. D. Giglio)	ATTN: DRDAR-SCP 1
2800 Powder Mill Road	ATTN: DRDAR-SCS 1
Adelphi, MD 20783	ATTN: DRDAR-TDC (Dr. D. Gyorog) 1
<b>Commander</b>	ATTN: DRDAR-TSS 2
USA Materials & Mechanics Research Center	ATTN: DRCPM-CAWS-AM 1
ATTN: DRXMR-MDE (Dr. Saul Isserow)	Dover, NJ 07801
Watertown, MA 02172	US Army Armament Research and
<b>Commander</b>	Development Command
USA Cold Region Research Engineering Laboratory	ATTN: DRDAR-TSE-OA (Robert Thresher) 1
ATTN: George Aitken	National Space Technology Laboratories
Hanover, NH 03755	NSTL Station, MS 39529
<b>Commander/Director</b>	Requirements and Analysis Office
Combat Surveillance and	Foreign Intelligence and Threat
Target Acquisition Laboratory	Projection Division
ERADCOM	ATTN: DRDAR-RAI-C 1
ATTN: DELCS-R (E. Frost)	Aberdeen Proving Ground, MD 21010
Ft. Monmouth, NJ 07703	<b>Commander</b>
	ARRADCOM
	ATTN: DRDAR-QAC-E 1
	Aberdeen Proving Ground, MD 21010
<b>Director</b>	<b>Director</b>
USA Ballistic Research Laboratory	ARRADCOM
	ATTN: DRDAR-BLB 1
	ATTN: DRDAR-TSB-S 1
	Aberdeen Proving Ground, MD 21005

US ARMY ARMAMENT MATERIEL READINESS COMMAND	Commander	
US Army Armament Materiel Readiness Command	US Army Infantry Center	1
ATTN: DRSAR-ASN	ATTN: ATSH-CD-MS-C	1
ATTN: DRSAR-IRI-A	ATTN: ATSH-CD-MS-F	1
ATTN: DRSAR-LEP-L	ATTN: ATZB-DPT-PO-NBC	1
ATTN: DRSAR-SF	Fort Benning, GA 31905	
Rock Island, IL 61299		
Commander	Commander	
US Army Dugway Proving Ground	USA Training and Doctrine Command	1
ATTN: Technical Library (Docu Sect)	ATTN: ATCD-N	1
Dugway, UT 84022	ATTN: ATCD-TEC (Dr. M. Pastel)	1
ATTN: ATCD-Z	ATTN: ATCD-Z	1
US ARMY TRAINING & DOCTRINE COMMAND	Fort Monroe, VA 23651	
Commandant	Commander	
US Army Infantry School	US Army Armor Center	1
ATTN: CTDD, CSD, NBC Branch	ATTN: ATZK-CD-MS	1
Fort Benning, GA 31905	ATTN: ATZK-PPT-PO-C	1
Commandant	Fort Knox, KY 40121	
US Army Missile & Munitions Center and School		
ATTN: ATSK-CM	Commander	1
Redstone Arsenal, AL 35809	USA TRADOC Systems Analysis Activity	1
ATTN: ATAA-SL	ATTN: ATAA-TDB (L. Dominguez)	1
White Sands Missile Range, NM 88002		
Commander	Commander	
US Army Logistics Center	USA Field Artillery School	1
ATTN: ATCL-MG	ATTN: ATSF-GD-RA	1
Fort Lee, VA 23801	Ft. Sill, OK 73503	
Commandant	Director	
US Army Chemical School	USA Concepts Analysis Agency	1
ATTN: ATZN-CM-C	ATTN: MOCA-SMC (Hal Hock)	1
ATTN: ATZN-CM-AD	8120 Woodmont Avenue	
ATTN: ATZN-CN-CDM (Dr. J. Scully)	Bethesda, MD 20014	
Fort McClellan, AL 36205	Los Alamos National Laboratory	1
ATTN: T-DOT, MS B279 (S. Gerstl)	ATTN: DRSTE-AD-M (Warren Baily)	1
Los Alamos, NM 87545	Aberdeen Proving Ground, MD 21005	
Commander	US ARMY TEST & EVALUATION COMMAND	
USAAVNC	Commander	
ATTN: ATZQ-D-MS	US Army Test & Evaluation Command	1
Fort Rucker, AL 36362	ATTN: DRSTE-CM-F	1
Commander	ATTN: DRSTE-CT-T	1
USA Combined Arms Center and Fort Leavenworth	ATTN: DRSTE-AD-M (Warren Baily)	1
ATTN: ATZL-CAM-IM	Aberdeen Proving Ground, MD 21005	
ATTN: ATZL-CA-SAN		
ATTN: ATZL-CA-TM-K		
Fort Leavenworth, KS 66027		

Commander USA EPG ATTN: STEEP-MM-IS ATTN: STEEP-MT-DS (CPT Decker) Ft. Huachuca, AZ 85613	1	Commander Naval Surface Weapons Center Dahlgren Laboratory ATTN: DX-21 ATTN: Mr. R. L. Hudson ATTN: F-56 (Mr. Douglas Marker) Dahlgren, VA 22448	1
Commander Dugway Proving Ground ATTN: STEDP-MT (Dr. L. Solomon) Dugway, UT 84022	1	Commander Naval Intelligence Support Center ATTN: Code 434 (H. P. St. Aubin) 4301 Suitland Road Suitland, MD 20390	1
<b>DEPARTMENT OF THE NAVY</b>			
Commander Naval Research Laboratory ATTN: Code 5709 (Mr. W. E. Howell) ATTN: Code 6532 (Mr. Curcio) ATTN: Code 6532 (Dr. Trusty) ATTN: Code 6530-2 (Mr. Gordon Stamm) ATTN: Code 8320 (Dr. Lothar Ruhnke) ATTN: Code 8326 (Dr. James Fitzgerald) ATTN: Code 43202 (Dr. Hermann Gerber) 4555 Overlook Avenue, SW Washington, DC 20375	1	Commander Naval Explosive Ordnance Disposal Technology Center ATTN: AC-3 Indian Head, MD 20640	1
Chief, Bureau of Medicine & Surgery Department of the Navy ATTN: MED 3033 Washington, DC 20372	1	Officer-in-Charge Marine Corps Detachment Naval Explosive Ordnance Disposal Technology Center Indian Head, MD 20640	1
Commander Naval Air Systems Command ATTN: Code AIR-301C (Dr. H. Rosenwasser) Washington, DC 20361	1	Commander Naval Air Development Center ATTN: Code 2012 (Dr. Robert Heimbold) Warminster, PA 18974	1
Commander Naval Sea Systems Command ATTN: SEA-62Y13 (LCDR Richard Gilbert) ATTN: SEA-62Y21 (A. Kanterman) ATTN: SEA-62Y21 (LCDR W. Major) Washington, DC 20362	1	Commander Naval Weapons Center ATTN: Code 382 (L. A. Mathews) ATTN: Code 3882 (Dr. C. E. Dinerman) ATTN: Code 3918 (Dr. Alex Shlanta) China Lake, CA 93555	1
Project Manager Theatre Nuclear Warfare Project Office ATTN: TN-09C Navy Department Washington, DC 20360	1	Commanding Officer Naval Weapons Support Center Applied Sciences Department ATTN: Code 50C, Bldg 190 ATTN: Code 502 (Carl Lohkamp) Crane, IN 47522	1
Institute for Defense Analysis 400 Army-Navy Drive ATTN: L. Biberman ATTN: R. E. Roberts Arlington, VA 22202	1	<b>US MARINE CORPS</b> Commanding General Marine Corps Development and Education Command ATTN: Fire Power Division, D091 Quantico, VA 22134	1

DEPARTMENT OF THE AIR FORCE

HQ AFLC/LOWMM  
Wright-Patterson AFB, OH 45433

HQ AFSC/SDZ  
ATTN: CPT D. Riediger  
Andrews AFB, MD 20334

USAF TAWC/THL  
Eglin AFB, FL 32542

USAF SC  
ATTN: AD/YQ (Dr. A. Vasiloff)  
ATTN: AD/YQO (MAJ Owens)  
Eglin AFB, FL 32542

AFAMRL/TS  
ATTN: COL Johnson  
Wright-Patterson AFB, OH 45433

Commander  
Hanscom Air Force Base  
ATTN: AFGL-POA (Dr. Frederick Volz)  
Bedford, MA 01731

Headquarters  
Tactical Air Command  
ATTN: DRP  
Langley AFB, VA 23665

AFOSR/NE  
ATTN: MAJ H. Winsor  
Bolling AFB, DC 20332

Dr. Charles Arpke  
OSV Field Office  
P.O. Box 1925  
Eglin AFB, FL 32542

OUTSIDE AGENCIES

Battelle, Columbus Laboratories  
ATTN: TACTEC  
505 King Avenue  
Columbus, OH 43201

Toxicology Information Center, JH 652  
National Research Council  
2101 Constitution Ave., NW  
Washington, DC 20418

Dr. W. Michael Farmer, Assoc. Prof., Physics  
University of Tennessee Space Institute 1  
Tullahoma, TN 37388

ADDITIONAL ADDRESSEES

Office of Missile Electronic Warfare  
ATTN: DELEW-M-T-AC (Ms Arthur) 1  
White Sands Missile Range, NM 88002

US Army Mobility Equipment Research and  
Development Center  
ATTN: DROME-RT (Mr. O. F. Kezer) 1  
Fort Belvoir, VA 22060

Director  
US Night Vision and EO Laboratories  
ATTN: DRSEL-NV-VI (Dr. R. G. Buser) 1  
ATTN: DRSEL-NV-VI (Mr. R. Bergemann) 1  
ATTN: DELNV-VI (Luanne Obert) 1  
ATTN: DELNV-L (D. N. Spector) 1  
Fort Belvoir, VA 22060

Commander  
217th Chemical Detachment  
ATTN: AFVL-CD 1  
Fort Knox, KY 40121

Headquarters  
US Army Medical Research and  
Development Command  
ATTN: SG RD-RMS 1  
Fort Detrick, MD 21701

Commander  
US Army Environmental Hygiene Agency  
ATTN: Librarian, Bldg 2100 1  
Aberdeen Proving Ground, MD 21010

Commandant  
Academy of Health Sciences, US Army  
ATTN: HSHA-CDH 1  
ATTN: HSHA-IPM 2  
Fort Sam Houston, TX 78234